

UC San Diego

UC San Diego Electronic Theses and Dissertations

Title

Advanced Phased-Arrays and Techniques for 5G Multi-Standard Applications and Carrier Aggregation at 24-29 GHz and 37-40 GHz

Permalink

<https://escholarship.org/uc/item/7f12g9n2>

Author

Yin, Yusheng

Publication Date

2020

Peer reviewed|Thesis/dissertation

UNIVERSITY OF CALIFORNIA SAN DIEGO

**Advanced Phased-Arrays and Techniques for 5G Multi-Standard Applications and
Carrier Aggregation at 24-29 GHz and 37-40 GHz**

A dissertation submitted in partial satisfaction of the
requirements for the degree
Doctor of Philosophy

in

Electrical Engineering (Electronic Circuits and Systems)

by

Yusheng Yin

Committee in charge:

Professor Gabriel M. Rebeiz, Chair
Professor Gert Cauwenberghs
Professor William Hodgkiss
Professor Vitaliy Lomakin
Professor Daniel F. Sievenpiper

2020

Copyright
Yusheng Yin, 2020
All rights reserved.

The dissertation of Yusheng Yin is approved, and it is acceptable in quality and form for publication on microfilm and electronically:

Chair

University of California San Diego

2020

DEDICATION

To my family

EPIGRAPH

The wealth of the mind is the only wealth.

TABLE OF CONTENTS

	Signature Page	iii
	Dedication	iv
	Epigraph	v
	Table of Contents	vi
	List of Figures	ix
	List of Tables	xiv
	Acknowledgements	xv
	Vita	xviii
	Abstract of the Dissertation	xix
Chapter 1	Introduction	1
	1.1 Background	1
	1.2 Motivation	3
	1.3 Thesis Overview	3
Chapter 2	Wideband 23.5-29.5 GHz Phased-Arrays for Multi-Standard 5G Applications and Carrier Aggregation	7
	2.1 Introduction	7
	2.2 Phased Array Architecture and Beamformer Chip	9
	2.3 Wideband Antenna Design	11
	2.4 Wideband Array Pattern and EIRP Measurements	13
	2.4.1 Channel Variation and Patterns	14
	2.4.2 Wideband Frequency Response and EIRP	17
	2.5 Multi-Standard and Wideband EVM Measurements	19
	2.6 Carrier Aggregation Analysis and Simulation	25
	2.6.1 Beam Squint and IM3 Patterns	25
	2.6.2 System level Carrier Aggregation Simulations	28
	2.7 5G Carrier Aggregation Measurements	30
	2.8 Conclusion	35
	2.9 Acknowledgment	36

Chapter 3	A 24-29.5 GHz 256-Element 5G Phased-Array with 65.5 dBm Peak EIRP and 256-QAM Modulation	37
	3.1 Introduction	37
	3.2 2x2 TRX Quad Beamformer Chip	38
	3.3 28 GHz 16x16 Phased-Array Design	39
	3.4 Pattern and EIRP Measurements	41
	3.5 EVM Measurements	44
	3.6 Conclusion	45
	3.7 Acknowledgment	46
Chapter 4	A 1 Gbps 3.5-4.75 km Communication Link Based on a 5G 28 GHz 8×8 Phased-Array	47
	4.1 Introduction	47
	4.2 Wideband 8x8 Phased-Array	48
	4.3 3.5-4.75 Km Communication Link Measurements	51
Chapter 5	A Bidirectional 36 Gbps Connectorless Connector at 2-4 cm Using a 28 GHz 2×2 Phased-Array with Position-Offset Compensation	56
	5.1 Introduction	56
	5.2 Connectorless Connector Based on a 2x2 Phased-Array	57
	5.3 Link Measurements with Connectorless Connector	58
	5.3.1 No Misalignment Case	59
	5.3.2 Misalignment of up to 63°	61
	5.4 Conclusion	64
Chapter 6	Determining the OIP3 and Bias-Network Resonances of Phased-Array Amplifiers Using Far-Field Measurement Techniques	65
	6.1 Introduction	65
	6.2 2x2 TRX Quad Beamformer Chip OIP3 Measurement	66
	6.3 28 GHz 4x8 Phased Array RF Performance Measurements	67
	6.4 Far-Field OIP3 Measurements Using the 4×8 Phased Array	70
	6.5 Conclusion	75
	6.6 Acknowledgment	75
Chapter 7	A 37-42-GHz 8×8 Phased-Array With 48-51-dBm EIRP, 64-QAM 30-Gb/s Data Rates and EVM Analysis Versus Channel RMS Errors	76
	7.1 Introduction	76
	7.2 Phased-Array Architecture and Beamformer	78
	7.3 Antenna Design	80
	7.4 EVM Analysis versus Gain and Phase Error	83
	7.5 Transceiver and High-Pass Filter	87
	7.6 39 GHz Phased-Array RF Performance Measurements	89
	7.6.1 Construction, Array Electronic Gain and Calibration	89

	7.6.2	Patterns, EIRP and Frequency Response Measurements . . .	93
	7.7	System Level Measurements	98
	7.7.1	Radiated LO and Image Power	98
	7.7.2	EVM	100
	7.7.3	Wideband Performance	102
	7.8	Conclusion	103
	7.9	Acknowledgment	104
Chapter 8		Conclusion and Future Work	106
	8.1	Conclusion	106
	8.2	Future Work	108
Bibliography		109

LIST OF FIGURES

Figure 2.1:	(a) Block diagram of the wideband 5G 8x8 phased-array and (b) spectrum for carrier aggregation.	8
Figure 2.2:	Block diagram of the wideband 23.5-29.5 GHz 2x2 beamformer chip. . .	10
Figure 2.3:	Stackup of low-cost 12-layer PCB.	11
Figure 2.4:	(a) 28 GHz wideband antenna model and coaxial feed. (b) Simulated S_{11} and S_{21} versus scan angle in E- and H-plane at the reference port. S_{21} is plotted at 0° and 30° (elevation) and 45° (azimuth) scan angles.	12
Figure 2.5:	Front and back view of the 28 GHz wideband 8x8 phased-array board. . .	13
Figure 2.6:	Measured normalized channel gain and phase variation at 27 GHz with calibration in the Tx mode.	14
Figure 2.7:	Measured H-plane (azimuth) patterns with 10-dB raised-cosine taper at (a) 25 GHz, (b) 27 GHz, and (c) 29 GHz, in the Rx mode.	15
Figure 2.8:	Measured E-plane (elevation) patterns with uniform illumination at (a) 25 GHz, (b) 27 GHz, and (c) 29 GHz in the Tx mode.	16
Figure 2.9:	Measured co-pol. versus cross-pol. patterns at (a) broadside, (b) 30° scan and (c) 50° scan in the H-plane at 27 GHz in the Rx mode.	17
Figure 2.10:	Measured (a) flat-top pattern and monopulse pattern at (a) broadside and (c) 50° scan at 27 GHz. Normalized to patterns with uniform illumination. . .	18
Figure 2.11:	Measured wideband frequency response of the 8x8 phased-array in the Tx and Rx modes.	19
Figure 2.12:	Measured: (a) $EIRP_{1dB}$ versus frequency, (b) EIRP versus number of element, and (c) $EIRP_{1dB}$ versus scan angle in the azimuth plane (H-plane) at different frequencies.	20
Figure 2.13:	Setup for EVM measurement at 1.3 m.	21
Figure 2.14:	(a) Measured EVM versus EIRP and spectrum at different power levels with (b) 200 Mbaud and (c) 800 Mbaud 64-QAM waveform at 27 GHz.	22
Figure 2.15:	Measured EVM versus EIRP with (a) 200 Mbaud 64-QAM waveform at 25 and 29 GHz and (b) with 800-Mbaud 64-QAM waveform at 24.5 and 29.5 GHz in single carrier mode.	23
Figure 2.16:	Measured EVM versus scan angle in the H-plane with 800 Mbaud 64-QAM at 6 dB and 10 dB backoff at 27 GHz.	24
Figure 2.17:	Measured EVM and constellations for 64-QAM and 256-QAM waveforms at a center frequency of 27 GHz.	24
Figure 2.18:	(a) Measured EVM versus data rate at 27 GHz with a 16-QAM waveform at different scan angles and (b) constellations at different data rates at normal incident (no scan).	25
Figure 2.19:	(a) Simulated beam squint patterns at 0° , 15° , 35° and 55° scan angles with phase setting at 27 GHz. Patterns are normalized to the broadside pattern. (b) Simulated antenna gain drop at the cross-over point at 25, 27 and 29 GHz. The element pattern follows $\cos(\theta)$ in the simulation.	26

Figure 2.20:	Measured H-plane at 25 and 29 GHz when scanning to 50° with phase setting at 27 GHz. Normalized to the peak of pattern at 27 GHz.	27
Figure 2.21:	(a) Simulated IM3 patterns at 15°, 35° and 55° scan angles. (b) Simulated detailed IM3 patterns at 21 and 33 GHz when scanning to 50° with phase setting at 27 GHz in the CA mode. Normalized to the peak of each pattern.	28
Figure 2.22:	(a) Setup for carrier aggregation simulation, and (b) simulated CCDF curve for 64-QAM modulated signal with one to four aggregated carriers.	29
Figure 2.23:	(a) Simulated broadband spectrum for output signal from beamformer with aggregated carriers at 25 and 29 GHz, (b) simulated spectrum for each modulated signal at complex baseband, and (c) corresponding constellation.	30
Figure 2.24:	(a) Architecture for phased-array transmitter in CA mode, and (b) setup for 5G carrier aggregation measurement.	31
Figure 2.25:	(a) Measured gain of Ka band horn antenna, (b) space loss factor at a distance of 1.38 m, (c) measured cable loss and (d) calculated correction factor ($-10*\log(SLF*G_r*Cable_Loss)$)	32
Figure 2.26:	Measured spectrum for 5G carrier aggregation at (a) broadside, (b) 30° and 50° scan with 200 Mbaud 64-QAM.	33
Figure 2.27:	Measured constellations and EVM for 5G CA using 200 Mbaud 64-QAM waveforms with 25- and 29-GHz carriers at different scan angles.	34
Figure 3.1:	Block diagram of the 256-element phased-array transceiver based on 2x2 transmit/receive beamformer chips.	38
Figure 3.2:	(a) Top and bottom views of the 12-layer 256-element phased-array PCB using 64 2x2 beamformer chips and stacked-patch antennas. (b) 12-layer PCB stack up.	39
Figure 3.3:	Measured channel gain and phase variation after calibration at 27 GHz.	40
Figure 3.4:	Measured H-plane (azimuth) patterns at (a) broadside and (b) 45° scan with uniform illumination at 27 GHz.	41
Figure 3.5:	Measured H-plane (azimuth) scanned patterns to ±60° at 27 GHz with 10-dB raised-cosine taper. (b) Measured versus simulated H-plane pattern at 27 GHz.	42
Figure 3.6:	Measured EIRP of the 16x16 phased-array at P1dB and Psat.	43
Figure 3.7:	EVM measurement setup for the 28 GHz 16x16 array.	44
Figure 3.8:	EVM versus EIRP with (a) 64-QAM and (b) 256-QAM 100 Mbaud modulation. (b) Constellations of 256-QAM modulation at different EIRP levels.	45
Figure 4.1:	Block diagram of 28 GHz 8x8 phased-array.	48
Figure 4.2:	Block diagram of the 28 GHz 2x2 quad TRX beamformer.	49
Figure 4.3:	(a) Measured H-Plane patterns in the TX mode at 29 GHz and (b) measured EIRP vs frequency at P1dB.	50
Figure 4.4:	Block diagram of the 3.5-4.75 km link measurement setup.	51
Figure 4.5:	Setup photos of the 3.5 km communication link measurement: (a) views of transmit and receive setup, (b) distance on Google map.	51

Figure 4.6:	Measured: (a) EVM at different data rates with QPSK modulation and (b) EVM at different scan angles in the azimuth plane with 200 Mbaud QPSK modulation.	53
Figure 4.7:	Measured constellations for the 3.5 km communication link.	54
Figure 5.1:	Front and back view of the 2x2 phased-array.	58
Figure 5.2:	Measurement setup for 2-4 cm link: (a) block-diagram, (b) photograph. . .	59
Figure 5.3:	Measured normalized EIRP of the 2x2 antenna array. Inset shows 2x2 pattern at broadside.	60
Figure 5.4:	(a) Misalignment view of the two connectorless connectors, (b) two beams in alignment.	61
Figure 5.5:	Measured: (a) EVM at different data rates, (b) constellations at different data rates with 16-QAM, 32-QAM, and 64-QAM modulation.	62
Figure 5.6:	Simulated patterns of the 2x2 array at broadside and for a scan angle of 50°.	63
Figure 5.7:	Measured 16-QAM EVM with different misalignment distance for 5 Gbaud symbol rate at R=4 cm.	63
Figure 6.1:	Architecture of a millimeter-wave phased array and its far-field radiated spectrum.	67
Figure 6.2:	(a) Block diagram of the 2x2 TRX beamformer chip and (b) picture of the test PCB board for single-channel OIP3 measurements.	68
Figure 6.3:	Measured (a) AM-AM and (b) AM-PM distortion for a single TX channel of the 2x2 TRX beamformer chip at 28 GHz.	68
Figure 6.4:	Measured (a) output power versus input power for the 2x2 beamformer chip at 28 GHz, and (b) output IM3 spectrum for a single channel with -36.7 and -33.7 dBm input power to the beamformer chip.	69
Figure 6.5:	(a) Block diagram of the 28 GHz 4x8 phased-array, (b) front and back view of the phased-array board.	70
Figure 6.6:	(a) Measured H-plane (azimuth) patterns at 27 GHz in the Tx mode. (b) Measured EIRP versus frequency.	71
Figure 6.7:	(a) Setup for far-field OIP3 measurement using a 4x8 phased array, (b) Friis block diagram for OIP3 in the far-field.	72
Figure 6.8:	Measured (a) received power at the horn versus input power to the array ($\Delta f=10$ MHz), and (b) IM3 spectrum at the horn with -22.4 and -19.4 dBm input power to the 32-element phased-array.	73
Figure 6.9:	Measured output power versus frequency spacing for (a) 1 kHz to 10 MHz with $P_{in}=-22.4$ dBm (array input power) and (b) 1 kHz to 800 MHz with $P_{in}=-19.4$ dBm (array input power). All output powers are referenced to the PA output of a single channel using Equation (5.2), (5.3).	74
Figure 7.1:	(a) Block diagram of the 39 GHz 8x8 phased-array, and (b) 2x2 39 GHz 5G TRX beamformer chip, and (c) dimensions of antennas and feed lines for the 2x2 cell at 30 GHz and 42 GHz. The 2x2 chip fits well within the 37-42 GHz antenna period.	77

Figure 7.2:	Stackup of the low-cost 12-layer PCB board.	79
Figure 7.3:	Single polarized 2x2 subarray with (a) standard feeds and (b) rotated feeds. (c) Simulated electric field distribution along the non-radiation edge of a single antenna. (d) Simulated 2x2 antenna array pattern with feed rotation. M1, M3 and M2, M4 are 180° out of phase.	81
Figure 7.4:	(a) 39 GHz antenna model and coaxial feed. Simulated S_{11} and S_{21} versus scan angle for (b) E-plane and (c) H-plane.	82
Figure 7.5:	(a) Setup for EVM analysis in Matlab and (b) transmit RF channel model with 11 dBm OP1dB and its AM-AM and AM-PM response.	83
Figure 7.6:	Simulated EVM versus rms gain and phase error across the array for a 64-QAM signal with $\alpha=0.35$ and a PAPR=7.7 dB, and at (a) 14 dB backoff, (b) 8 dB backoff and (c) 5 dB backoff. Constellations are plotted for 2 dB rms gain error and 20° rms phase error.	85
Figure 7.7:	Simulated EVM versus number of element with 1 dB rms gain error and 10° rms phase error at (a) 8 dB and (b) 5 dB backoff for 60 iterations.	86
Figure 7.8:	(a) Block diagram of UCSD wideband transceiver and (b) measured broadband spectrum at 10 dB backoff from P1dB in the TX mode.	88
Figure 7.9:	(a) Simulation model for the 39 GHz high-pass filter, (b) measured and simulated filter S-parameters.	89
Figure 7.10:	Front and back view of the 39 GHz 8x8 phased-array.	90
Figure 7.11:	Block diagram for system analysis in (a) TX mode, and (b) RX mode.	90
Figure 7.12:	Measurement setup for pattern and calibration.	92
Figure 7.13:	Measured normalized gain and phase variation (a) without calibration and (b) with calibration at 39 GHz in the TX mode for 64 channels.	92
Figure 7.14:	Measured broadside co-pol and cross-polarization components at (a) broadside, (b) 30° scan angle in the H-plane and (c) 60° scan angle in the H-plane. All patterns are measured at 39 GHz without calibration.	94
Figure 7.15:	Measured H-plane patterns in the TX mode with and without calibration for (a) uniform illumination, and (b) 6-dB raised cosine taper.	95
Figure 7.16:	Measured E-plane patterns without calibration at 39 GHz.	96
Figure 7.17:	Measured beam-squint from 38 to 40 GHz at 50° scan angle in the H-plane and normalized to the broadside pattern at 39 GHz. Patterns are measured without calibration.	96
Figure 7.18:	(a) Measured EIRP at P1dB and P_{sat} versus frequency with and without calibration and (b) wideband frequency response in TX and RX modes of the 39 GHz 8x8 array.	97
Figure 7.19:	(a) Setup for 39 GHz 8x8 array 1 m link and EVM measurements. (b) Measured spectrum for the 39 GHz array system at P1dB.	99
Figure 7.20:	Measured (a) EVM versus EIRP at 39 GHz with a 200 MBaud 64-QAM waveform with and without calibration, and (b) constellations at different EIRP levels.	101
Figure 7.21:	Measured EVM versus scan angles in the H-plane for a 64-QAM waveform. Measurements done without calibration.	102

Figure 7.22: Measured (a) EVM versus data rate with 16 and 64-QAM waveforms, (b) constellations at different data rates. Measurements done without calibration. 103

LIST OF TABLES

Table 2.1:	Summary of the 2x2 SiGe TRX beamformer chip	10
Table 2.2:	Comparison with State of the Art 28 GHz Phased-Arrays	35
Table 4.1:	Summary of the 2x2 TRX beamformer chip	49
Table 4.2:	Link budget for 3.5-4.75 km communication	52
Table 5.1:	Summary of the 2x2 TRX array.	57
Table 5.2:	Link budget for R=4 cm	60
Table 7.1:	Summary of the 2x2 SiGe TRX beamformer chip	79
Table 7.2:	Comparisons with State-of-the-Art 39-GHz Phased-Arrays	104

ACKNOWLEDGEMENTS

First and foremost, I would like to express my sincerest gratitude to my advisor Professor Gabriel M. Rebeiz for his continuous guidance, support and encouragement during my entire doctoral studies. As a fresh student with little research experience, I really appreciated his guidance and training which led me to the right path of research. One important lesson I learned from him is that one has to pay extreme attention to all the details to make things work. And his insightful comments and advice will become the most valuable treasure in my life. Again, I feel really luck to have the opportunity to work in his group.

I also would like to thank my dissertation committee members, Prof. Gert Cauwenberghs, Prof. William Hodgkiss, Prof. Vitaliy Lomakin and Prof. Daniel F. Sievenpiper for their time, interest, and valuable comments.

I would like to thank my TICS group members over four years. First, I must thank current TICS group members Qian Ma, Hyunchul Chung, Yaochen Wang, Abdurrahman Alijuhani, Ahmed Nafe, Tom Phelps, Changtian Wang, Kevin Low, Siwei Li, Zhe Zhang, Sultan Alqarni, Gokhan Gultepe, Abdurrahman Alhamed, Oguz Kazan and Dimitrios Baltimas for their technical discussions and friendship. I would also like to thank the previous TICS group members, Samet Zehir, Tumay Kanar, Mustafa Sayginer, Hasan Al-Rubaye, Kerim Kibaroglu, Eric Wagner, Umut Kodak, Bhaskar Rupakula, Li Gao and Omar Elaasar for their help and support.

The dissertation would not have been completed without the support of my colleagues Qian Ma and Hyunchul Chung. We were partners on many projects and they were always happy to offer me help and share with their experience. I really enjoy working with them.

This thesis was completed with the generous support of Intel, the UCSD Center for Wireless Communications, Renesas Electronics, and the Laboratory for Telecommunication Sciences.

Last but not least, I must express my gratitude to my parents, Ming Yin and Guirong Zheng for their unconditional love and encouragement and family has always been the source of

energy and courage for me.

The material in this dissertation is based on the following papers which are either published, has been submitted for publication, or contains material that is currently being prepared for submission for publication.

Chapter 2, in full, has been submitted for publication of the material as it may appear in: Y. Yin, B. Ustundag, K. Kibaroglu, M. Sayginer and G. M. Rebeiz, "Wideband 23.5-29.5 GHz phased-arrays for multi-standard 5G applications and carrier aggregation", *IEEE Trans. Microw. Techn.*, accepted. The dissertation author was the primary investigator and author of this paper.

Chapter 3, in part, is a reprint of the material as it may appear in: Y. Yin, Z. Zhang, T. Kanar, S. Zehir and G. M. Rebeiz, "A 24-29.5 GHz 256-element 5G phased-array with 65.5 dBm peak EIRP and 256-QAM modulation", in *IEEE International Microwave Symposium (IMS)*, June, 2020. The dissertation author was the primary investigator and author of this paper.

Chapter 4, in full, is a reprint of the material as it appears in: Y. Yin, T. Phelps, B. Ustundag, K. Kibaroglu, M. Sayginer and G. M. Rebeiz, "A 1 Gbps 3.5-4.75 km communication link based on a 5G 28 GHz 8×8 phased-array", in *IEEE International Symposium on Phased Array System & Technology (PAST)*, Oct, 2019, pp.1-4. The dissertation author was the primary investigator and author of this paper.

Chapter 5, in full, is a reprint of the material as it appears in: Y. Yin, B. Ustundag, K. Kibaroglu, M. Sayginer and G. M. Rebeiz, "A bidirectional 36 Gbps connectorless connector at 2-4 cm using 28 GHz 2×2 phased-array with position-offset compensation", in *IEEE International Microwave Symposium (IMS)*, June, 2019, pp.1084-1087. The dissertation author was the primary investigator and author of this paper.

Chapter 6, in full, is a reprint of the material as it may appear in: Y. Yin and G. M. Rebeiz, "Determining the OIP3 and bias-network resonances of phased-array amplifiers using far-field measurement techniques", *IEEE Antennas and Wireless Propagation Letter.*, submitted. The dissertation author was the primary investigator and author of this paper.

Chapter 7, in full, is a reprint of the material as it appears in: Y. Yin, S. Zehir, T. Kanar, Q. Ma, H. Chung, L. Gao and G. M. Rebeiz, "A 37-42-GHz 8×8 phased-array with 48-51-dBm EIRP, 64-QAM 30-Gb/s data rates, and EVM analysis versus channel RMS errors", *IEEE Trans. Microw. Techn.*, accepted. The dissertation author was the primary investigator and author of this paper.

VITA

- 2016 B. S. in Electrical and Electronics Engineering, University of Electronic Science and Technology of China, China
- 2018 M. S. in Electrical Engineering (Electronic Circuits and Systems)
- 2020 Ph. D. in Electrical Engineering (Electronic Circuits and Systems)

PUBLICATIONS

- Y. Yin et al., "A 37-42-GHz 8×8 phased-array with 48-51-dBm EIRP, 64-QAM 30-Gb/s data rates, and EVM analysis versus channel RMS errors", *IEEE Trans. Microw. Techn.*, accepted.
- Y. Yin, B. Ustundag, K. Kibaroglu, M. Sayginer and G. M. Rebeiz, "Wideband 23.5-29.5 GHz phased-arrays for multi-standard 5G applications and carrier aggregation", *IEEE Trans. Microw. Techn.*, accepted.
- Z. Zhang, Y. Yin and G. M. Rebeiz, "Intersymbol interference and equalization for large 5G phased-arrays with wide scan angles", *IEEE Trans. Microw. Techn.*, submitted.
- Y. Yin and G. M. Rebeiz, "Determining the OIP3 and bias-network resonances of phased-array amplifiers using far-field measurement techniques", *IEEE Antennas and Wireless Propagation Letter.*, submitted.
- Y. Yin, Z. Zhang, T. Kanar, S. Zehir and G. M. Rebeiz, "A 24-29.5 GHz 256-element 5G phased-array with 65.5 dBm peak EIRP and 256-QAM modulation", in *IEEE International Microwave Symposium (IMS)*, June, 2020.
- Y. Yin, T. Phelps, B. Ustundag, K. Kibaroglu, M. Sayginer and G. M. Rebeiz, "A 1 Gbps 3.5-4.75 km communication link based on a 5G 28 GHz 8×8 phased-array", in *IEEE International Symposium on Phased Array System & Technology (PAST)*, Oct, 2019, pp.1-4.
- Y. Yin, S. Zehir, T. Kanar and G. M. Rebeiz, "A 37-42 GHz 8×8 phased-array for 5G communication systems with 48-50 dBm EIRP", in *IEEE International Microwave Symposium (IMS)*, June, 2019, pp.480-483.
- Y. Yin, B. Ustundag, K. Kibaroglu, M. Sayginer and G. M. Rebeiz, "A bidirectional 36 Gbps connectorless connector at 2-4 cm using 28 GHz 2×2 phased-array with position-offset compensation", in *IEEE International Microwave Symposium (IMS)*, June, 2019, pp.1084-1087.

ABSTRACT OF THE DISSERTATION

Advanced Phased-Arrays and Techniques for 5G Multi-Standard Applications and Carrier Aggregation at 24-29 GHz and 37-40 GHz

by

Yusheng Yin

Doctor of Philosophy in Electrical Engineering (Electronic Circuits and Systems)

University of California San Diego, 2020

Professor Gabriel M. Rebeiz, Chair

The millimeter-wave (mm-wave) spectrum is currently used for the fifth-generation (5G) standard for high data-rate and low-latency links for both mobile users and fixed wireless access. The 5G standard supports licensed bands at 23.5-30.5 GHz and 37-43 GHz and unlicensed band at 57-71 GHz. Compared with 4G bands, the mm-wave bands support $10\times$ larger bandwidth and thus can greatly improve the data-rate and maximize the throughput. At millimeter-wave frequencies, phased-array antennas with 32 to 512 elements are used to increase the antenna directivity so as to overcome the severe path loss. Such arrays can improve the link margin and allow for Gbps communications at 50-1000 meters. The research projects in this dissertation, in

consequence, focus on the design and implementation of wideband 5G phased-arrays at 28 GHz and 39 GHz with 64 to 256 elements and with state-of-the-art performance. Also, the phased array system analysis for EVM degradation versus RMS error, and advanced applications such as carrier aggregation at mm-waves are investigated.

Chapter 1

Introduction

1.1 Background

The ever increasing mobile data traffic has caused stress on the current 4G cellular network. In consequence, the millimeter-wave spectrum has drawn a lot of attention over the past few years and is now approved to be used for the fifth-generation (5G) communication systems to provide mobile users with Gbps and low-latency data links. Compared with 4G communication systems which deliver a maximum data rate of a few hundred of Mbps, the 5G mm-wave network employs carrier frequencies at 28 GHz, 39 GHz or even up to 60 GHz which has more than $10\times$ larger available bandwidth and thus can achieve tens of Gbps communication links. Therefore, 5G communication systems are capable of supporting the emerging techniques and applications, such as the internet of vehicles, smart city and virtual reality which all require high data-rate transfer with low latency.

Although 5G communications have many advantages, some drawbacks exist and many challenges need to be solved. The first obstacle is the increased free space loss ($SLF=(\lambda/4\pi R)^2$) for electromagnetic signals at mm-wave frequency bands. If the signal wavelength decreases by a factor of 10, the free space loss will increase by a factor of 100 and this results in a $10\times$

shorter communication distance given the same effective isotropic radiated power (EIRP) and transmit/receive (TRX) antenna gain. Also, the mm-wave signal suffers more propagation loss from the atmospheric absorption compared with its sub-6 GHz counterpart and its line of sight (LOS) property degenerates the ability of diffraction when the signal encounters obstacles in the transmission.

The challenge also arises from the design and implementation of mm-wave systems. Phased arrays, with high antenna gain and beam steering capabilities, emerge as an effective solution to overcome the high path loss and allow for long-distance communication links. However, unlike the sub-6 GHz antenna arrays where the passive antenna elements and active TRX modules are designed and optimized separately and then connected together through connectors and cables, mm-wave phased arrays follow different design strategies. For example, the transmission-line effect and its loss become significant at mm-wave frequencies so that the design of interconnection between antennas and TRX channels has the same importance as the antenna design itself so as to achieve the best system performance. Some other factors like the coupling between antenna elements should also be considered in the design procedure.

Another issue which exists in 5G mm-wave phased-arrays is the channel-to-channel variation and calibration. The performance variation for each antenna element usually comes from the fabrication mismatch of different beamformer chips, printed-circuit-board (PCB) fabrication errors and non-ideal behavior of surface mounted devices (SMD). This variation can be compensated using calibration techniques and a good system performance can be maintained. Since the deployment quantity of 5G mm-wave base stations is much larger than the 4G network, the cost of calibration overhead should be reduced to a minimum. Therefore, efficient calibration methods should be investigated and it is important to know what calibration is enough to achieve excellent performance.

Despite of the challenges that need to be addressed for 5G mm-wave technology, it is still very promising and worth investigating. The effort of both industry and academia will speed up

the deployment of the 5G mm-wave network and the next generation wireless technology will become part of people's daily life in the near future.

1.2 Motivation

The 5G era is approaching and wireless communications evolved from traditional broadcast systems to directive communications with the use of phased arrays. Also, low-cost commercial silicon beamformer chips with excellent performance (OP1dB, NF, etc.) have become available which makes it possible to construct affordable 5G phased arrays. Therefore, mm-wave phased arrays with 64 to 256 elements can be implemented with high EIRP, low system noise figure and high electronic gain, and these arrays are capable of achieving up to 10 Gbps data links within 300 m to 1000 m range.

There are various interesting topics worth investigating. One is the design of phased arrays with wideband performance, for example, a wideband 23.5-29.5 GHz phased array is demonstrated in this dissertation which can be used for multi-standard and 5G inter-band carrier aggregation. Another topic is the analysis of the array performance versus systematic errors such as the channel-to-channel variation. It is essential to understand the phased array tolerance to these non-ideal factors so as to reduce the cost in practical deployment. In addition to the regular communication scenarios, phased arrays can also be used for other applications such as the short-distance Gbps data transfer between smart devices and point-to-point communication links at few kilometers.

1.3 Thesis Overview

This thesis presents demonstrations of high performance mm-wave phased-array systems at 28 GHz and 39 GHz along with their advanced applications and system analysis.

Chapter 2 presents a 23.5-29.5 GHz 8x8 phased-array for wideband multi-standard applications. The array is based on wideband high-performance 2x2 transmit/receive (TRX) quad-beamformer chips with 6-bit of phase control and 8-bit of gain control. The antenna is designed using a stacked-patch structure combined with a two-stage impedance matching network to enhance its bandwidth. The 8x8 phased-array achieves an effective isotropic radiated power (EIRP) of 54.8 dBm at P1dB with a 3-dB bandwidth of 23.5-30.5 GHz, and can scan to $\pm 60^\circ$ in the azimuth plane and $\pm 40^\circ$ in the elevation plane with excellent patterns with a single-point calibration at 27 GHz. Measured error vector magnitude (EVM) for a 64-QAM 200 and 800 Mbaud waveforms result in a system EVM of 5% (-26 dB) at an average EIRP of 46-47 dBm at 24.5-29.5 GHz. Also, the wideband array is capable of 16-QAM 24 Gbps links with an EVM $< 16\%$ over all scan angles. An inter-band carrier aggregation system is also demonstrated with the wideband array using 200 Mbaud 64-QAM waveforms with 25- and 29-GHz carriers. The phased-array phase and amplitude settings are chosen such that the 25 GHz and 29 GHz waveforms are radiating simultaneously at the same angle with low scan loss, resulting in an efficient system. Also, the out-of-band 3rd-order intermodulation products generated by the power amplifier on each element are filtered out by the antenna. Carrier aggregation measurements with up to 50° scan angles are demonstrated with low EVM. To the author's knowledge, this is the first demonstration of carrier aggregation in mm-wave 5G systems.

Chapter 3 presents a 24-29.5 GHz 256-element phased-array for 5G applications. The array is based on commercial 2x2 TRX beamformer chips, designed with SiGe BiCMOS technology, which employ 6 bits of phase control and 8 bits of gain control. A symmetrical 1:64 Wilkinson network is used to distributed the power to all elements. The phased-array can achieve -20 dB sidelobe levels after calibration, and can scan up to $\pm 60^\circ$ in the azimuth-plane and $\pm 50^\circ$ in the elevation-plane. The measured EIRP is 63.5 dBm and 65.5 dBm at P1dB and Psat respectively, with a 3-dB bandwidth of 5.5 GHz (24-29.5 GHz). Complex modulation measurements on the 16x16 array with 64-QAM and 256-QAM 100 Mbaud waveforms ($\alpha=0.35$, PAPR=7.7 to 8.2

dB) show low EVM values (2-3%) up to an EIRP of 58 dBm. This is the first 256-element array for 5G applications with very high EIRP, and which can support 64 and 256-QAM modulation formats.

Chapter 4 presents a 200 Mbps to 1 Gbps communication link at a distance of 3.5-4.75 km using two high-performance 28 GHz 8x8 phased-arrays. The 8x8 transmit array achieves an EIRP of 53-54 dBm to overcome the 132.5-135.2 dB path loss at these large distances. The error vector magnitude (EVM) was measured with different data rates and at different scan angles in the azimuth plane. An EVM of <36% was achieved for a maximum data rate of 1 Gbps, which is enough for QPSK with FEC (forward error correction). At 200 Mbps with QPSK modulation, an EVM of 17% was achieved. To our knowledge, this work is the first demonstration of communication links at few kilometers using 5G phased-arrays.

Chapter 5 presents a high-data rate wireless link over a short distance using a 2x2 phased-array. The array can be used as a connectorless connector that enables ultra-fast data transfer without the need for a physical cable connecting the transmitter and receiver. It is seen that the use of phased-array scanning, even in a small array, greatly increases the link robustness versus misalignment and maintains a low EVM over large misalignment distances.

Chapter 6 presents a method to determine the OIP3 of phased-array amplifiers using a far-field measurement, the equation is derived and verified by experiment. The far-field OIP3 is then measured using a 5G 28 GHz 32-element phased array employing 2x2 beamformer chips, and the far-field derived OIP3 agrees well with measurements done on a single amplifier. This technique therefore allows the user to determine the (average) OIP3 of the power amplifiers used in an array even if they do not have access to the individual beamformer chip. An additional benefit is the ability of characterizing the PCB bias network resonances in a phased-array environment.

Chapter 7 presents a 5G 37-42 GHz 8x8 phased-array. The array is based on 2x2 SiGe transmit/receive (TRX) beamformer chips in SiGe technology with 6 bits of phase control and 8 bits of gain control. A detailed study is presented showing the effects of array-level amplitude

and phase errors on the radiated EVM of 64-element arrays. The array scans to $\pm 60^\circ$ in the azimuth plane and $\pm 50^\circ$ in the elevation plane with low sidelobes. The measured peak effective isotropic radiated power (EIRP) is 51 dBm at P_{sat} with a 3-dB bandwidth of 36-41.5 GHz. A 39 GHz communication system is also demonstrated along with a high-pass filter and an integrated up/down-converter, and achieves an LO and image rejection level of 50 dBc, meeting FCC requirements of < -13 dBm/MHz of total leakage power. The array achieves $< 5\%$ error vector magnitude (EVM) (-26 dB) using a 64-QAM 200 MHz waveform at an average EIRP of 44 dBm over all scan angles, including the LO and up/down-converter contributions. A 30 Gbps communication link with 64-QAM modulation is also shown. To our knowledge, this is first demonstration of a 39-GHz phased-array communication system for 5G applications.

Chapter 8 concludes the dissertation and discusses future work.

Chapter 2

Wideband 23.5-29.5 GHz Phased-Arrays for Multi-Standard 5G Applications and Carrier Aggregation

2.1 Introduction

The demand for high data-rate communications for mobile users has promoted the investigation of multi-gigabit-per-second phased-array systems for the fifth-generation (5G) communication standard [1–16]. At millimeter-wave frequencies, phased-array antennas with 32-512 elements are used to increase the antenna directivity so as to overcome the severe path loss (SLF = space loss factor = $(\lambda/4\pi R)^2 = -62$ dB for $R = 1$ m at 30 GHz). Such arrays improve the link margin and allow for Gbps communications at 50-300 meters.

There are different frequency bands allocated worldwide to 5G mm-wave systems including the 24.25-27.5 GHz, 27.5-29.5 GHz, 37-40 GHz and 40-43 GHz bands. Previously, phased-arrays and their related chips were designed to operate in one band which limited their use as the number of bands increased. It is therefore advantageous to design phased-array beamformer

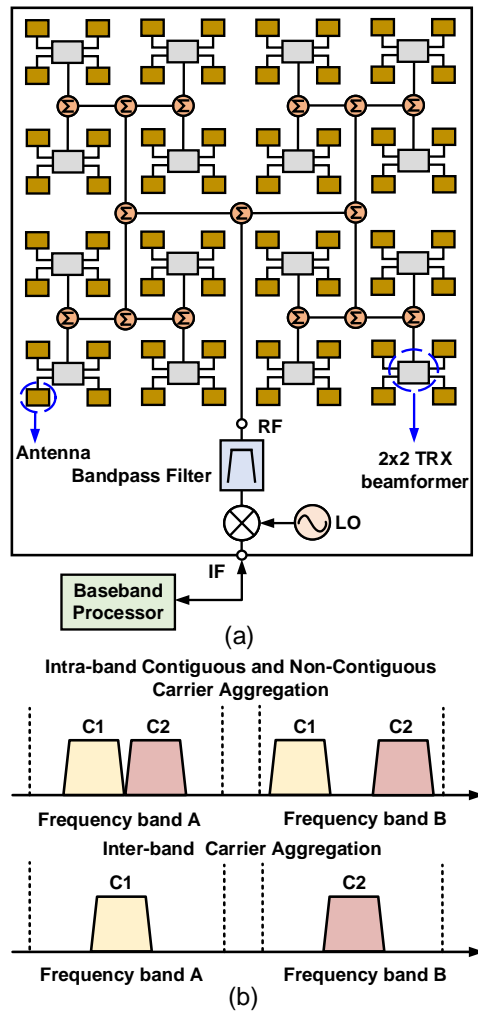


Figure 2.1: (a) Block diagram of the wideband 5G 8x8 phased-array and (b) spectrum for carrier aggregation.

chips and antenna arrays which can operate over a wider band, such as 23.5-29.5 GHz and 37-43 GHz so as to allow multi-standard operation and reduce the cost of deployment.

Carrier aggregation (CA), which combines multiple component carriers (CCs) across the available spectrum, is a potential technique which can be used to increase the spectral efficiency and maximize the throughput. An example of sub-6 GHz CA is LTE Advanced (Release 10) which supports up to five 20 MHz carriers which can be allocated to an individual user. There are different types of CA scenarios: a) intra-band contiguous CA, b) intra-band

non-contiguous CA and c) inter-band CA (Fig. 2.1b). The intra-band contiguous CA mode is effectively indistinguishable from advanced 5G standards employing OFDM waveforms with 4x or 8x 100 MHz component carriers, and presented in a number of mm-wave phased-array system demonstrations [17–22]. This paper focuses on the inter-band CA which aggregates multiple CCs in different frequency bands as it can enhance the efficient use of spectrum, especially if the operator has purchased two distinct frequency bands (such as AT&T with 24-25 GHz and 28-29 GHz). For such an application, a wideband phased-array is required and its operation in CA mode should be investigated.

In this work, a 64-element wideband 23.5-29.5 GHz phased-array for multi-standard and carrier aggregation is presented. Operation at different frequencies from 25 to 29 GHz is first demonstrated, and then, over-the-air (OTA) 5G carrier aggregation with two CCs at 25 GHz and 29 GHz is presented. Challenges in 5G CA such as the increase of peak-to-average-power-ratio (PAPR), beam-squint at different carriers, and the generation of 3rd-order intermodulation components and their filtering are studied in detail with experimental verification.

2.2 Phased Array Architecture and Beamformer Chip

The 64-element (8x8) phased-array employs the architecture shown in Fig. 2.1a. It is based on 2x2 (quad) transmit/receive (TRX) beamformer chips fabricated in SiGe technology, and flipped on a low-cost multiple-layer printed circuit board (PCB). The 64 antenna elements are placed on the other side of the PCB and are directly fed by beamformer chips using a probe feed. This ensures minimum transmission-line loss between the chip and the antenna and results in optimal performance both in the Tx and Rx modes. A wideband transceiver is used at the common point, and a filter is integrated on the PCB for added LO and image rejection. This topology has been presented before in numerous papers and will not be expanded here for brevity [6, 8, 10, 12, 16].

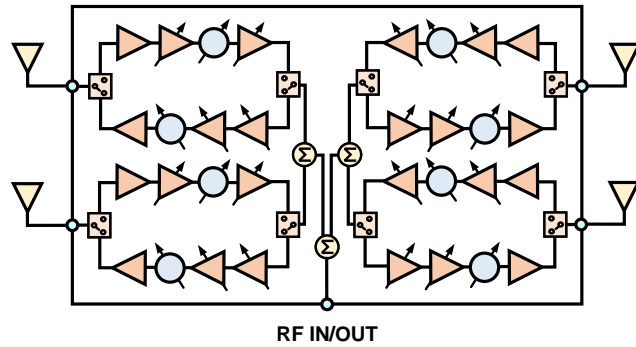


Figure 2.2: Block diagram of the wideband 23.5-29.5 GHz 2x2 beamformer chip.

Table 2.1: Summary of the 2x2 SiGe TRX beamformer chip

Receive mode		Transmit mode	
Gain (dB)	19	Gain (dB)	22
NF (dB)	5.5	OP1dB (dBm)	15-16
IP1dB (dBm)	-19	IP1dB (dBm)	-7
Gain Control	26	Gain Control (dB)	26
Phase shifter	6-bit	Phase shifter	6-bit
DC power / ch (W)	0.156	DC power / ch (W)	0.34
VDD (V)	2.3	VDD (V)	2.3

The wideband beamformer chip contains four RF TRX channels and a common RF port with a 1:4 on-chip Wilkinson network as shown in Fig. 2.2. Each channel of the beamformer chip contains a 6-bit phase shifter, 8-bit variable gain amplifier (VGA), a power amplifier (PA) and a low noise amplifier (LNA). The phase shifter has a phase step of 5.6° and the VGA provides a gain control of 26 dB. The PA results in an OP1dB of 15-16 dBm at 23-31 GHz. The beamformer chip also has a noise figure (NF) of 5.5 dB at 27 GHz with an IP1dB of -19 dBm. The power consumption is 156 mW/channel in the receive mode due to the high linearity of the chip, and 340 mW/channel in the transmit mode at P1dB (Table 2.1). The chip is controlled using a serial peripheral interface (SPI). Details of the chip design and measured performance are shown in [11].

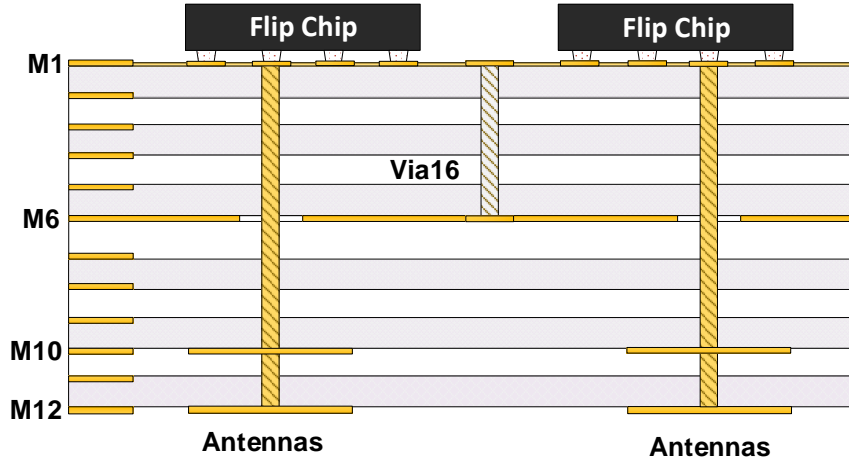


Figure 2.3: Stackup of low-cost 12-layer PCB.

2.3 Wideband Antenna Design

The 8x8 phased-array is built on a low-cost Megtron 6 PCB ($\epsilon_r = 3.4$, $\tan \delta = 0.005$ at 30 GHz). Sixteen quad beamformer chips are used on the M1 layer as shown in Fig. 2.3. Also, a 1:16 Wilkinson power combining network is designed on the M1 layer with a compact configuration. The antenna is a stacked-patch structure on M10 and M12 to enhance the antenna bandwidth, and with the M6 layer used as the antenna ground. Such an antenna can result in 15% bandwidth, but a two-stage matching network is used on M1 to further enhance the impedance matching between the antenna and the beamformer chip and results in a 25% fractional bandwidth. To our knowledge, this is nearly the limit of achievable bandwidth for a standard microstrip antenna [23, 24]. The SPI control lines and VDD are routed on M2-M5.

Fig. 2.4a presents the antenna model on M1 and M12 layers which includes the antenna, coaxial feed and the matching network. This is simulated using ANSYS HFSS with Master/Slave boundary conditions along with the Floquet port excitation. Fig. 2.4b presents the simulated antenna S_{11} and S_{21} when scanning in the E- and H-planes and a -10 dB bandwidth of 24-30.5 GHz is achieved. The S_{21} includes the antenna efficiency and the matching network ohmic loss on M1 layer up to the reference port (defined at the chip's RF port) as shown in Fig. 2.4a. The

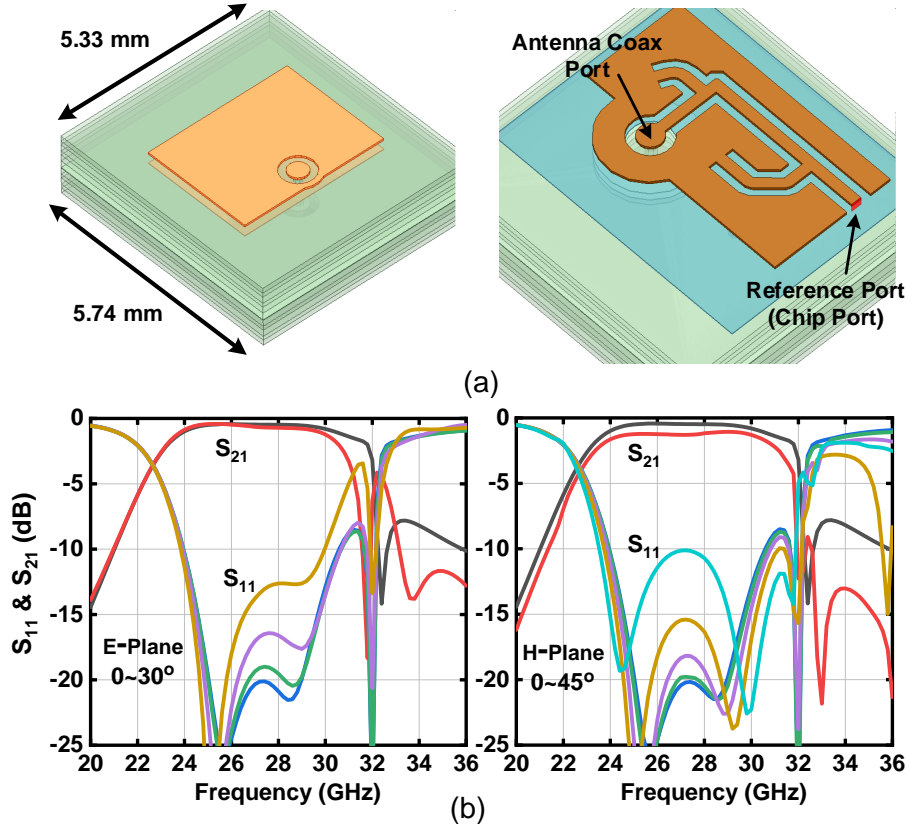


Figure 2.4: (a) 28 GHz wideband antenna model and coaxial feed. (b) Simulated S_{11} and S_{21} versus scan angle in E- and H-plane at the reference port. S_{21} is plotted at 0° and 30° (elevation) and 45° (azimuth) scan angles.

antenna has an average simulated loss of 0.5 dB at 0° and increases to 1.3 dB at 45° scan angle. Note that the antenna relative response is -8 to -10 dB at 21 GHz and 33 GHz, which is required for filtering the intermodulation products in the carrier-aggregation system.

The 8x8 phased-array employs an antenna grid size of 5.3 mm (0.53λ @ 30 GHz) on the horizontal (azimuth) axis and 5.74 mm (0.574λ @ 30 GHz) on the vertical (elevation) axis. With this spacing, a scanning capability of $\pm 60^\circ$ in azimuth and $\pm 40^\circ$ in elevation without grating lobes is achieved at the maximum frequency of 29.5 GHz. The board is designed with full symmetry and with equal feed-line lengths so that minor calibration is needed when measuring the patterns and EIRP. The antenna feeds between two neighboring rows are rotated for a low cross-polarization. This results in a cross-polarization level below -28 dB over all scan

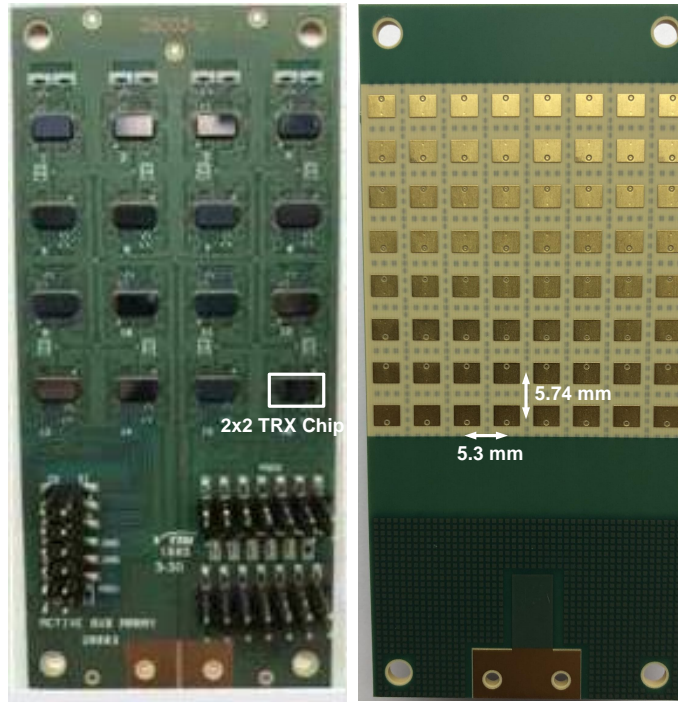


Figure 2.5: Front and back view of the 28 GHz wideband 8x8 phased-array board.

angles [8, 16].

For wideband designs, the antenna directivity changes versus frequency. For a uniform illumination, the 8x8 array has a gain of 21.7-23.7 dB at 23.5-29.5 GHz, respectively. Therefore, for the same radiated power per element versus frequency, the EIRP at 23.5 GHz is 2 dB lower than at 29.5 GHz.

2.4 Wideband Array Pattern and EIRP Measurements

The fabricated phased-array board is shown in Fig. 2.5 with an antenna aperture of $4.6 \times 4.3 \text{ cm}^2$. The array consumes 10 W in the Rx mode and 21.8 W in the Tx mode at P1dB. Also, the 8x8 array is designed to be scalable on the azimuth plane so that one can place multiple arrays side by side without generating grating lobes.

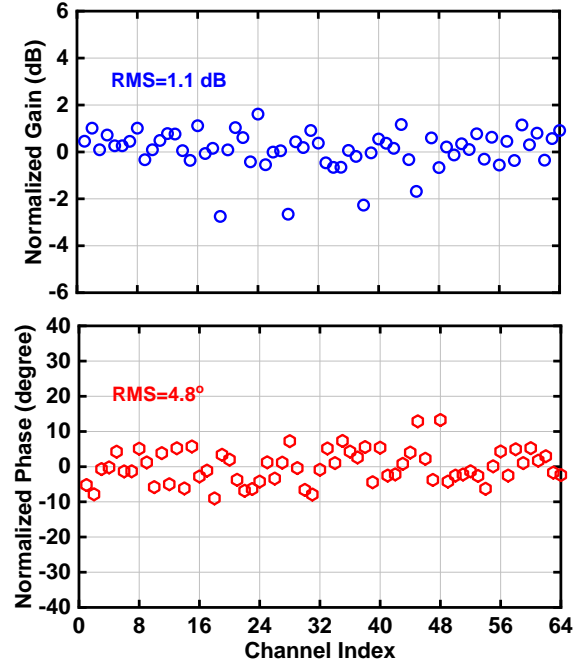


Figure 2.6: Measured normalized channel gain and phase variation at 27 GHz with calibration in the Tx mode.

2.4.1 Channel Variation and Patterns

The 64-element array is first calibrated in the far-field by turning on one element at a time. The VGA and phase shifter are then used to compensate the offset between the reference channel and all other channels. Fig. 2.6 presents the measured gain and phase variation after calibration at 27 GHz in the Tx mode. An rms gain and phase error of 1.1 dB and 4.8°, respectively, is achieved. Note that the calibration is only done at 27 GHz and is enough to achieve high-quality patterns and EVM measurements at 24.5-29.5 GHz due to the symmetry of the design.

Fig. 2.7 presents the measured Rx H-plane patterns with 10-dB raised-cosine taper at 25, 27 and 29 GHz. The array scans to $\pm 50^\circ$ with a sidelobe level < -20 dB at all frequencies and the gain only drops by 3-4 dB at the largest scan angle. A 10 dB raised-cosine is used to show the stringent -20 dB sidelobe levels and how a single-point calibration is adequate for this array. At 27 GHz, the 3-dB beamwidth is 15.6° - 20° at 0° - 50° scan angles. The Tx mode patterns are similar and not shown.

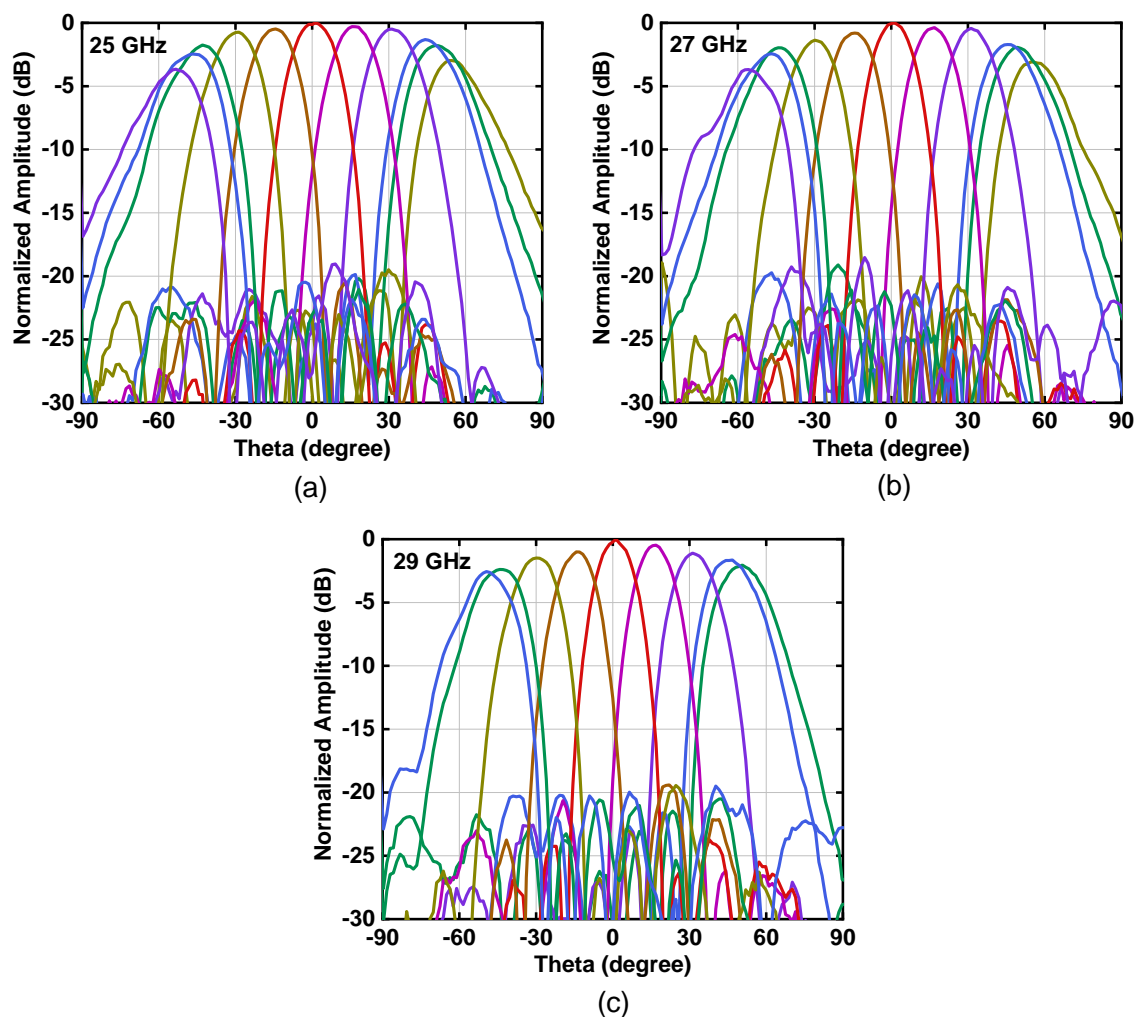


Figure 2.7: Measured H-plane (azimuth) patterns with 10-dB raised-cosine taper at (a) 25 GHz, (b) 27 GHz, and (c) 29 GHz, in the Rx mode.

Fig. 2.8 presents the measured E-plane patterns with uniform illumination at 25, 27 and 29 GHz in the Tx mode. The array can scan to $\pm 40^\circ$ at 25 and 29 GHz and scan to $\pm 30^\circ$ at 29 GHz with < -11 dB sidelobes. The pattern drops by more than 5 dB when scanning to 40° at 29 GHz, and this is due to the surface-wave mode arising from the 0.56λ antenna grid size in the elevation plane.

Fig. 2.9 presents the measured broadside pattern with uniform illumination at 27 GHz, and the cross-polarization level is < -32 dB at broadside. A cross-polarization level of < -28 dB is

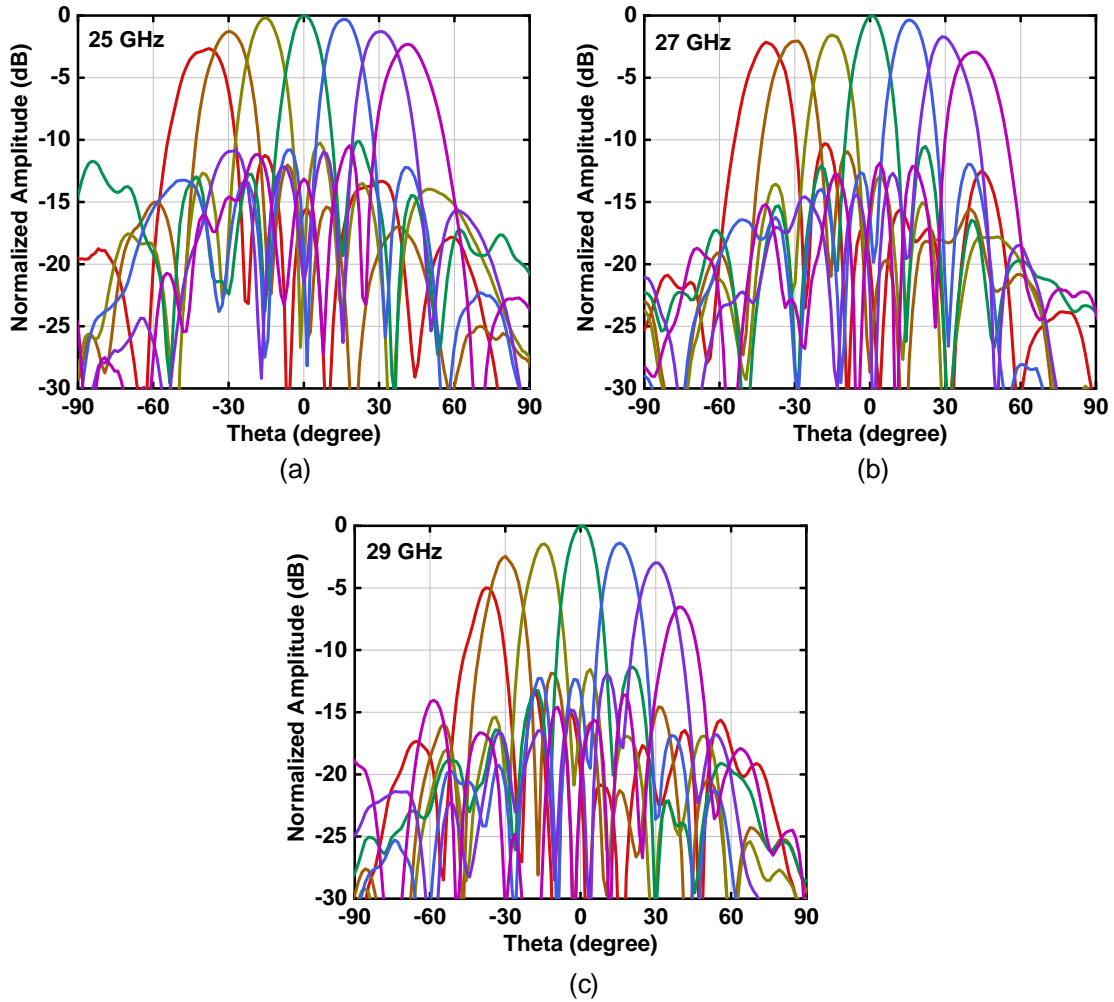


Figure 2.8: Measured E-plane (elevation) patterns with uniform illumination at (a) 25 GHz, (b) 27 GHz, and (c) 29 GHz in the Tx mode.

achieved over all scan angles in the H-plane due to the utilization of feed-rotation technique. The 3-dB beamwidth is 12.6° - 18° at 0° - 50° scan angles.

Fig. 2.10a presents measured patterns for wide coverage areas in the azimuth plane. The amplitude distribution across the array elements follows a *sinc* function [6]. Such a pattern spreads the energy equally over wide angles and improves the coverage for users for a short distance communications. Similar patterns are achieved at 25 GHz and 29 GHz and are not shown. Fig. 2.10b-c present the measured monopulse patterns which can be used for user tracking. A <-24

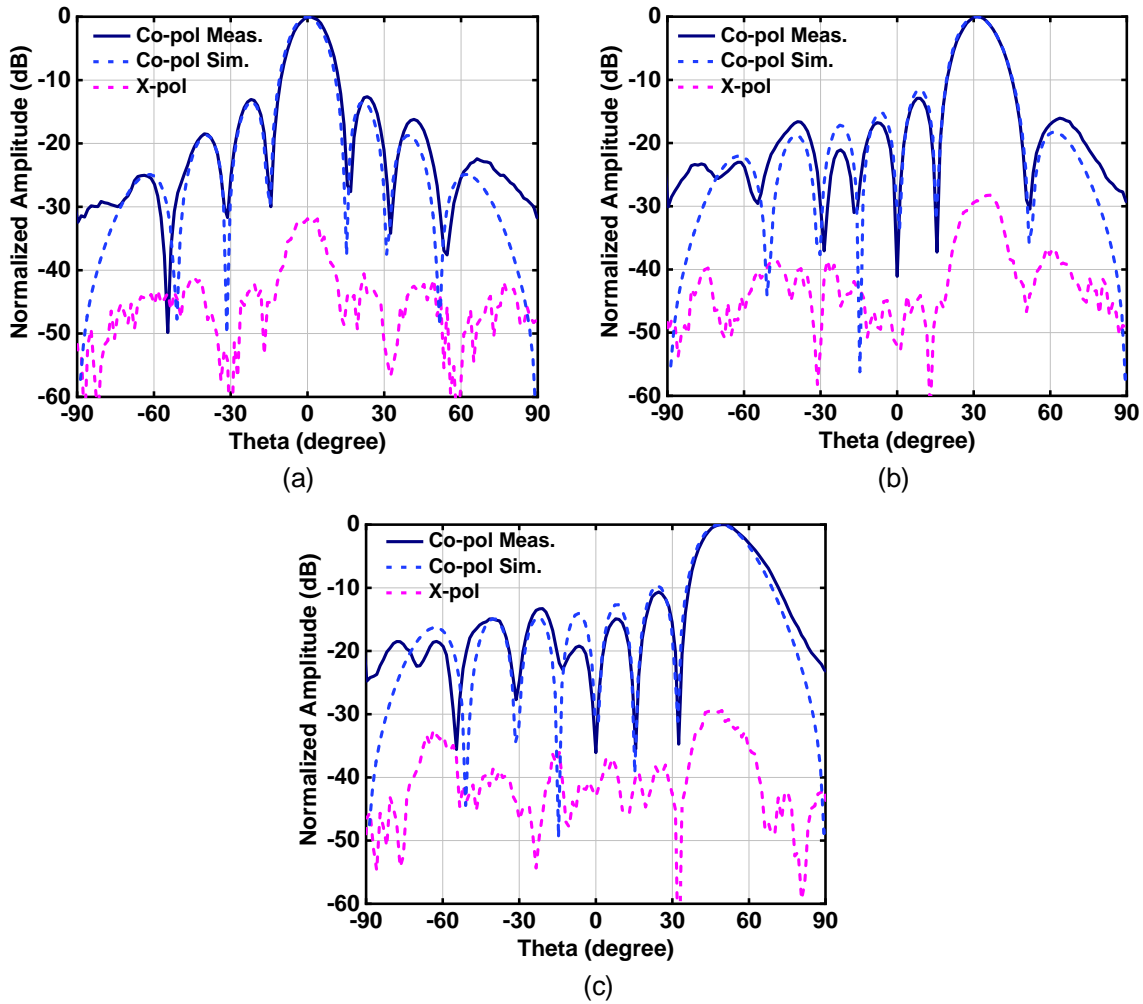


Figure 2.9: Measured co-pol. versus cross-pol. patterns at (a) broadside, (b) 30° scan and (c) 50° scan in the H-plane at 27 GHz in the Rx mode.

dB null level can be achieved at all scan angles for tracking purposes.

2.4.2 Wideband Frequency Response and EIRP

Fig. 2.11 presents the measured wideband frequency response of the 8x8 array. The measured 3-dB bandwidths in the Tx and Rx modes are 25.5-29.4 GHz and 24-29.6 GHz, respectively. This includes the Wilkinson network, the chip electronic gain and the antenna response. Note that in the Tx mode, a better figure of merit is the EIRP as more input power can

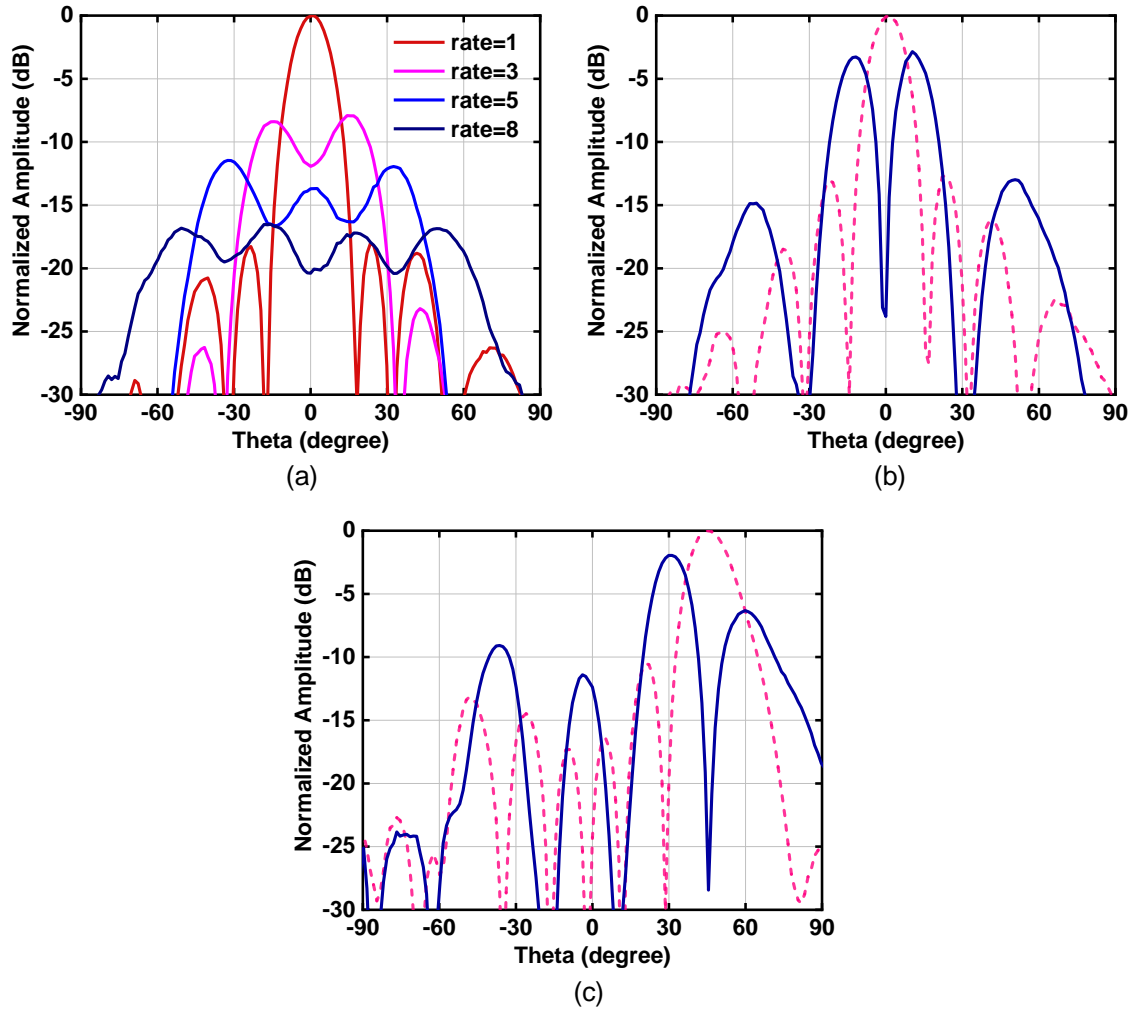


Figure 2.10: Measured (a) flat-top pattern and monopulse pattern at (a) broadside and (c) 50° scan at 27 GHz. Normalized to patterns with uniform illumination.

be used to overcome the chip electronic gain drop.

Fig. 2.12a presents the measured EIRP of the 8x8 phased-array at broadside and an EIRP of 54.8 dBm at P1dB is achieved. The EIRP has a 3-dB bandwidth of 23.5-30.5 GHz and agrees with simulations at 27-28 GHz ($EIRP = 20\log N + G_{ant} + P_{element} = 36 + 4 + 15 - 16 = 55 - 56$ dBm, where $G_{ant} = D_{ant} - Loss$. $D_{ant} = 5$ dB at 28 GHz and $Loss = 1$ dB is the antenna loss and matching network loss). Note that at 23.5 GHz, the phased-array directivity is 1.5 dB lower than at 28 GHz and also, the antenna reflection coefficient is -10 dB resulting in an additional 0.5 dB power loss.

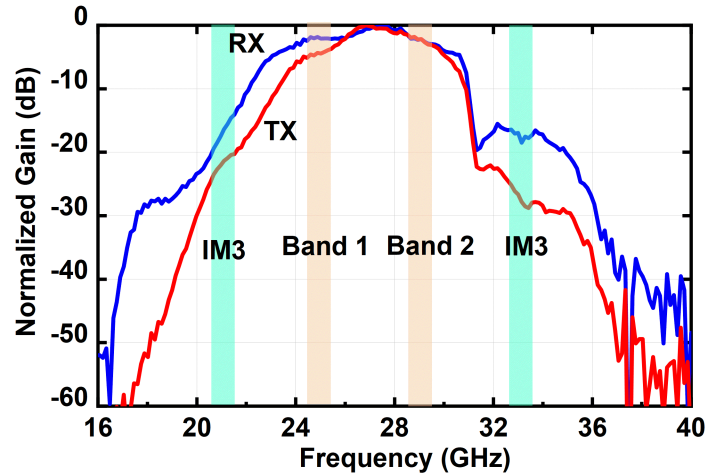


Figure 2.11: Measured wideband frequency response of the 8x8 phased-array in the Tx and Rx modes.

Therefore, the 2x2 SiGe beamformer chip has a wideband and well-matched PA and contributes only 1 dB of transmit-power degradation to the EIRP at 23.5 GHz.

Fig. 2.12b presents the measured EIRP versus different number of elements with the input power set at the IP1dB level for 27 GHz. The EIRP increases as $20\log N$ with the increase of element number, and the variation between different clusters also becomes less due to the averaging effect of phased-arrays. A wide EIRP bandwidth is achieved at all sub-array levels (several 32-element arrays, several 16-element arrays).

Fig. 2.12c presents the $EIRP_{1dB}$ at different scan angles in the H-plane (azimuth scan) at 25-29 GHz, and less than 3 dB EIRP drop is obtained within a $\pm 50^\circ$ scan range for all frequencies. As shown in Fig. 2.4b, the antenna is designed to be well matched even at large scan angles, and the beamformer PAs can still deliver almost the same amount of power at P1dB compared with broadside.

2.5 Multi-Standard and Wideband EVM Measurements

EVM measurements using a single-carrier (SC) are performed on the wideband 8x8 array with the setup shown in Fig. 2.13. A Keysight arbitrary waveform generator (M8195 AWG)

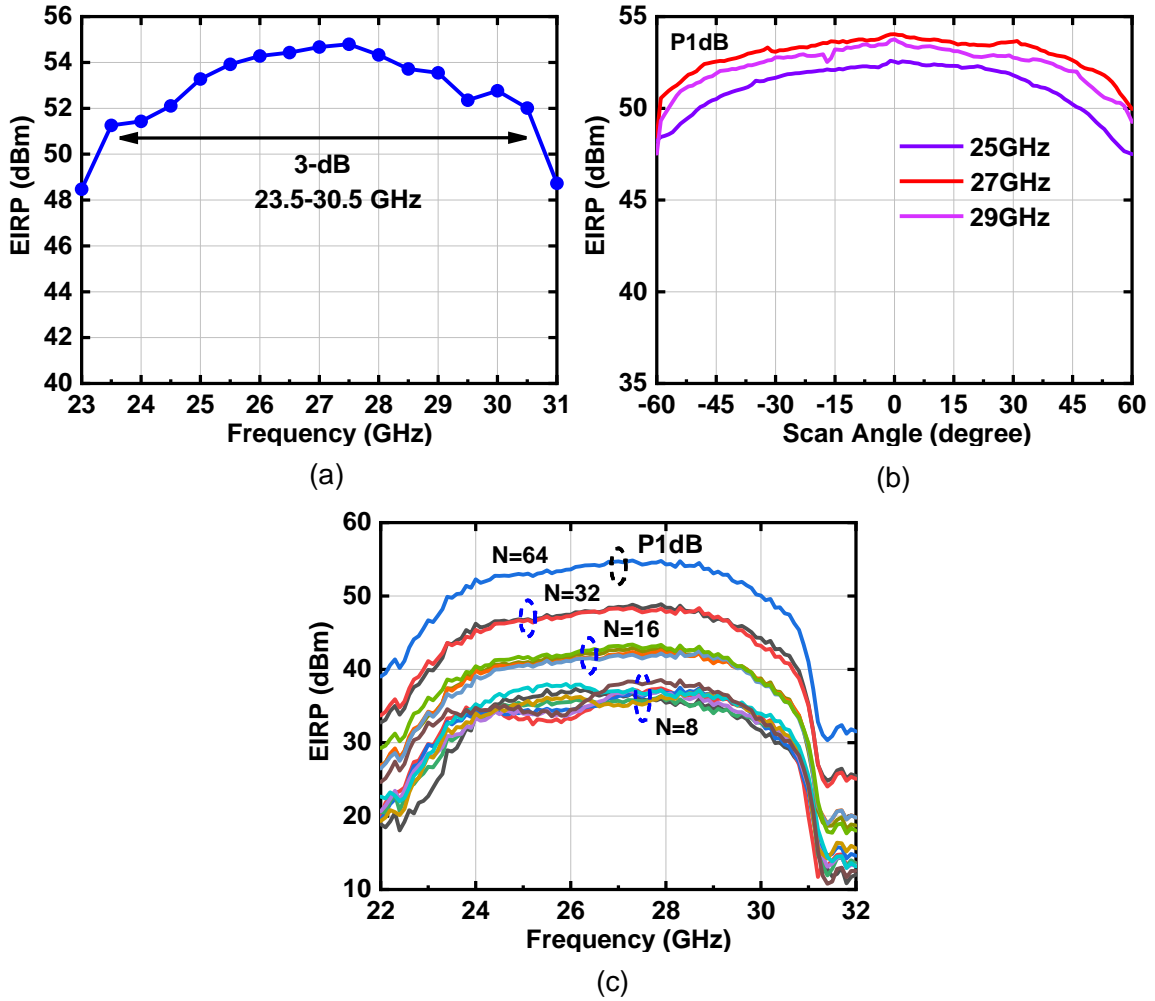


Figure 2.12: Measured: (a) $EIRP_{1dB}$ versus frequency, (b) EIRP versus number of element, and (c) $EIRP_{1dB}$ versus scan angle in the azimuth plane (H-plane) at different frequencies.

is used to generate the modulated signal with the center frequency at 27 GHz. The modulated signal is amplified by a PA and fed into the transmit array. A Ka-band horn antenna is placed at a distance of 1.3 m which results in a space-loss-factor (SLF) of 63.3 dB at 27 GHz. A Keysight 63 GHz real-time oscilloscope (DSOZ632A) is then used to demodulate the signal using the Keysight Vector Signal Analysis software (VSA-89600). An external LNA is placed after the horn antenna to maintain SNR of the link since the DSO has a NF of 20 dB.

Fig. 2.14a presents the measured EVM versus EIRP with a 200 Mbaud 64-QAM waveform

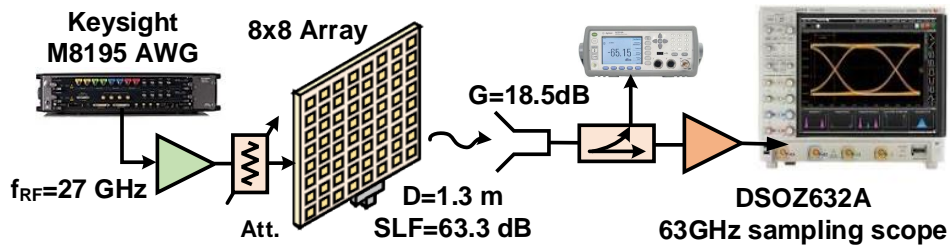


Figure 2.13: Setup for EVM measurement at 1.3 m.

at 27 GHz, and a PAPR of 7.7 dB with a pulse shaping factor $\alpha = 0.35$. The EVM is first limited at low EIRP with the SLF of 63.3 dB. In the mid-region, the EVM is constant at 2.6% (-31.7 dB) and is limited by the transmit chain SNR together with the DSO phase noise. At high EIRP, the EVM is limited by the PA non-linearity. At 5% system EVM_{rms} (-26 dB), the array achieves an average EIRP of 46.5 dBm which is 8 dB backoff from the array's P1dB. If the background 2.6% is taken out, the array delivers an EIRP of 47 dBm at an EVM of 5% (-26 dB). Fig. 2.14a also presents the EVM measurements done with 800 Mbaud bandwidth. It is interesting that the 800 Mbaud performance is ~ 1 dB better than the 200 Mbaud achieving a 5% EVM_{rms} (-26 dB) at an EIRP of 48 dBm, and this could be due to the power amplifier bias network. Fig. 2.14b, c present the measured spectrum at different backoff levels from P1dB using the 200 Mbaud and 800 Mbaud 64-QAM waveforms at 27 GHz. At 8 dB backoff (EIRP = 46.5 dBm), the measured adjacent channel power ratio (ACPR) is -32 to -33 dBc (mid-band point).

Fig. 2.15a presents the measured EVM versus EIRP using the 200 Mbaud 64-QAM waveform at 25 and 29 GHz in single-carrier mode. Note that in this measurement, the system is optimized further and the EVM floor is 2% (instead of 2.6 %). At 5% EVM_{rms} (-26 dB), the radiated EIRP is 45.5 dBm for both frequencies showing the wideband performance of the array. Similar measurements were done using the 800 Mbaud waveform and an EIRP of 46-46.5 dBm is obtained for an EVM of 5%. The EVM is also measured at 27 GHz for different scan angles with the 800 Mbaud 64-QAM waveform. A nearly constant EVM can be obtained over $\pm 50^\circ$ scan

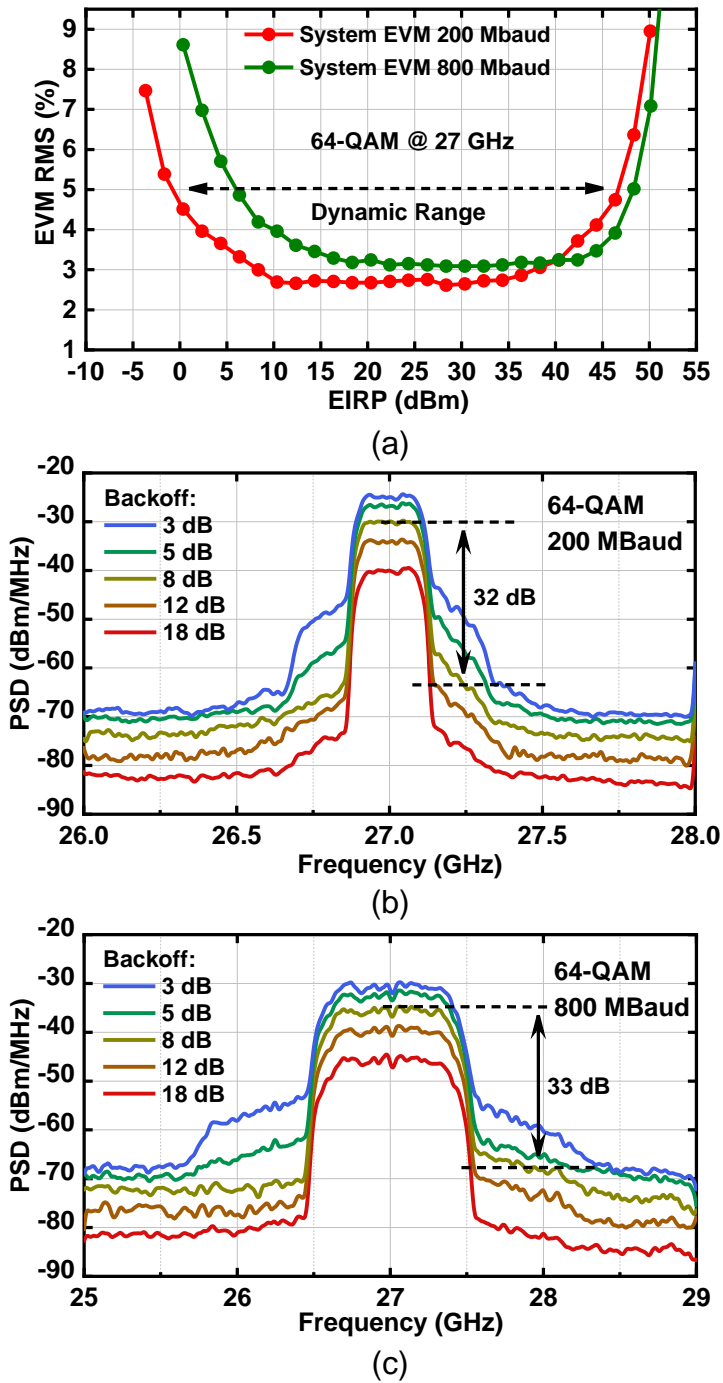


Figure 2.14: (a) Measured EVM versus EIRP and spectrum at different power levels with (b) 200 Mbaud and (c) 800 Mbaud 64-QAM waveform at 27 GHz.

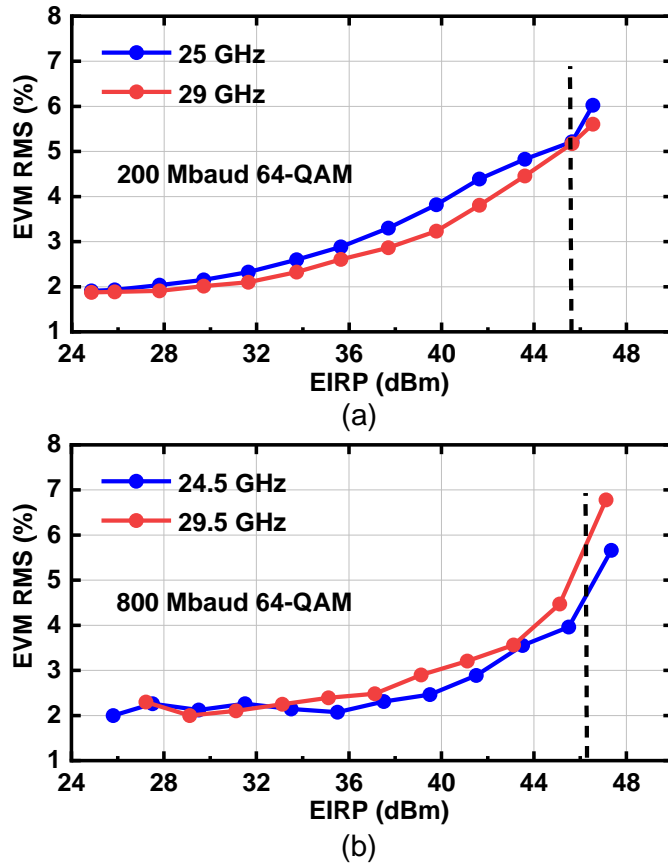


Figure 2.15: Measured EVM versus EIRP with (a) 200 Mbaud 64-QAM waveform at 25 and 29 GHz and (b) with 800-Mbaud 64-QAM waveform at 24.5 and 29.5 GHz in single carrier mode.

range at 6 dB and 10 dB backoff from P1dB (Fig. 2.16). Similar measurements were obtained at different frequencies.

Fig. 2.17 presents the measured constellations in the mid-EVM region (30 to 40 dBm) for different modulations. It is seen that near-ideal performance can be obtained from this phased-array even with 400 Mbaud 256-QAM waveforms having a PAPR of 8.2 dB.

The 8x8 array has a 6-7 GHz instantaneous bandwidth and therefore, can be used for wideband ultra-high-data transfer. Fig. 2.18a presents the measured EVM versus data rate using 16-QAM waveforms with $\alpha = 0.35$ (PAPR=6.6 dB) at 0° , 40° and 60° scan angles. A maximum data rate of 24 Gbps can be achieved with an $EVM_{rms}=14.4\%-16\%$ (-17 dB to -16 dB). The different time of arrival for elements across the phased-array causes inter-symbol interference

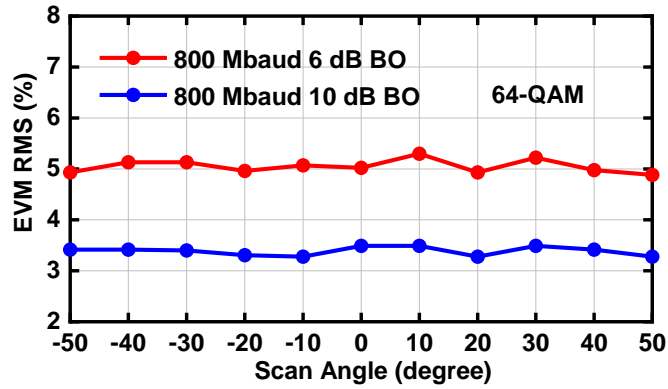
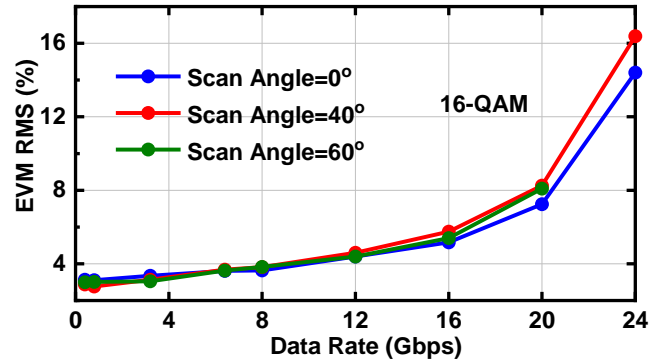


Figure 2.16: Measured EVM versus scan angle in the H-plane with 800 Mbaud 64-QAM at 6 dB and 10 dB backoff at 27 GHz.

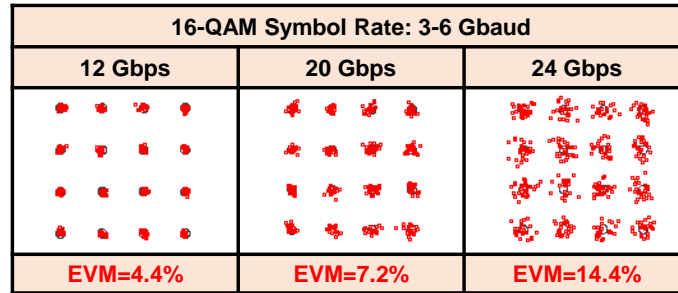
64-QAM Symbol Rate: 200-800 Mbaud		256-QAM Symbol Rate: 200-400 Mbaud	
1.2 Gbps	4.8 Gbps	1.6 Gbps	3.2 Gbps
EVM=2.6%	EVM=3.2%	EVM=2.5%	EVM=2.7%

Figure 2.17: Measured EVM and constellations for 64-QAM and 256-QAM waveforms at a center frequency of 27 GHz.

(ISI) which degenerates the EVM especially at large scan angles with high data rate. But the measured EVM does not degrade even at 40° to 60° scan angle due the use of an FIR equalizer in the DSO. The measured constellations for different data rates are shown in Fig. 2.18b.



(a)



(b)

Figure 2.18: (a) Measured EVM versus data rate at 27 GHz with a 16-QAM waveform at different scan angles and (b) constellations at different data rates at normal incident (no scan).

2.6 Carrier Aggregation Analysis and Simulation

2.6.1 Beam Squint and IM3 Patterns

CA operating at 25 and 29 GHz results in phased-array beam squint due to the use of constant phase shifters on the antenna elements. Beam squint causes loss in the antenna gain for the different CA frequencies at the observation angle especially when scanning to wide angles. The pointing angle can be calculated as:

$$\sin(\theta_f) = \frac{f_0}{f} \cdot \sin(\theta_0) \quad (2.1)$$

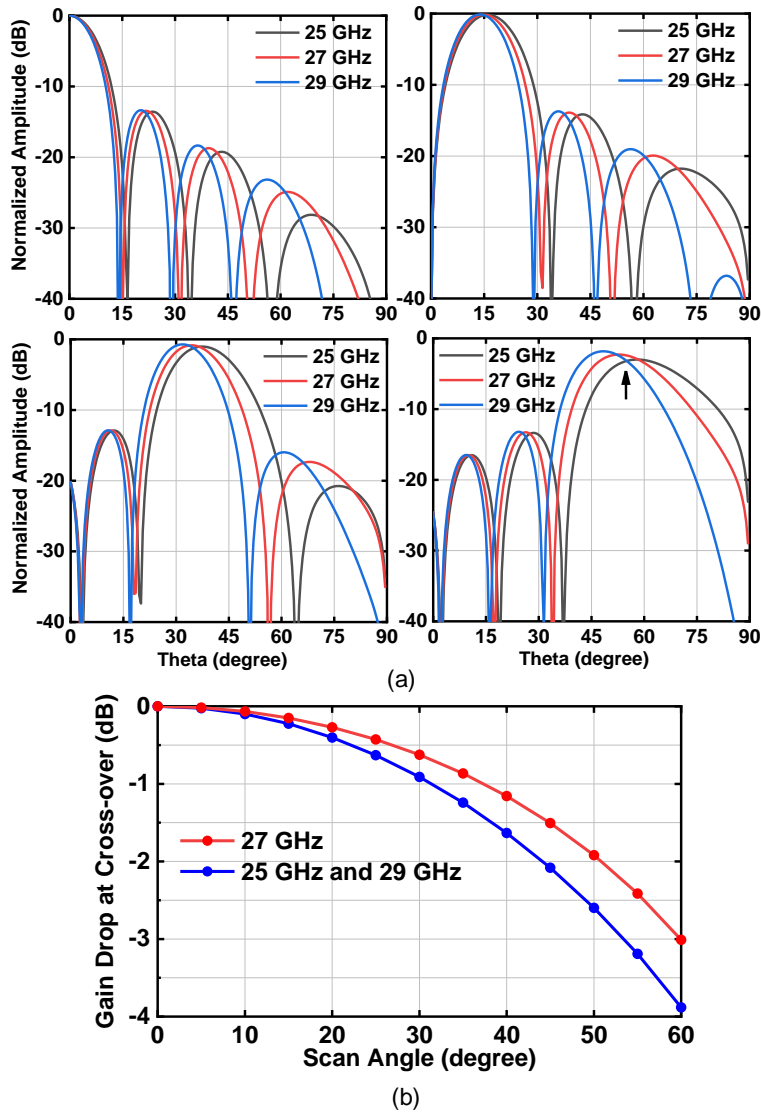


Figure 2.19: (a) Simulated beam squint patterns at 0° , 15° , 35° and 55° scan angles with phase setting at 27 GHz. Patterns are normalized to the broadside pattern. (b) Simulated antenna gain drop at the cross-over point at 25, 27 and 29 GHz. The element pattern follows $\cos(\theta)$ in the simulation.

where f_0 and θ_0 are the phase shifter setting frequency and scan angle, and f and θ_f are the operating frequency and pointing angle (in this case, 25 GHz and 29 GHz). Fig. 2.19a presents the simulated patterns at 25, 27 and 29 GHz for scan angles of 0° , 15° , 35° , 55° . The phase shifts on the array are set at 27 GHz and one can clearly see that the 25 and 29 GHz patterns are pointed at different angles. Note that the 25 GHz points higher than the scan angle, and the 29 GHz

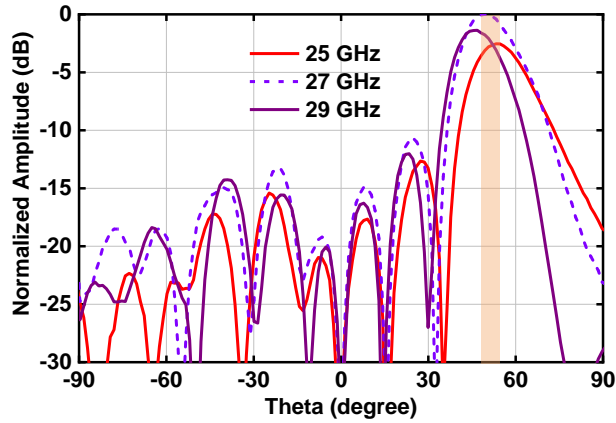


Figure 2.20: Measured H-plane at 25 and 29 GHz when scanning to 50° with phase setting at 27 GHz. Normalized to the peak of pattern at 27 GHz.

pattern points lower than the scan angle. Therefore, there is always an intersection angle which has minimal loss in antenna gain for both 25 and 29 GHz patterns. This property ensures that the inter-band CA can work for wide scan angles without excessive pattern gain loss, even if the two frequency bands are 4 GHz away from each other. The pattern gain loss (intersection point) is shown in Fig. 2.19b for the 8x8 array. It is seen that the maximum excess gain loss (due to the pattern crossover operation) is only 0.5 dB at 55° scan angle. Fig. 2.20 presents the measured H-plane patterns at 25 and 29 GHz with phase setting at 27 GHz for 50° scan, and an excess gain loss of <0.5 dB for each pattern can be achieved. The lower gain at 25 GHz and 29 GHz is due to the array frequency response (see Fig. 2.11).

The phased array also generates IM3 components ($2f_2-f_1$, $2f_1-f_2$) at 21 GHz and 33 GHz due to the PA non-linearities on each antenna element. These IM3 components radiate at different angles when the phase shifters are set for θ_0 at 27 GHz (Fig. 2.21a) [25]. Fig. 2.21b presents detailed patterns for a 50° scan angle, and it is seen that the IM3 components peak at 80° (21 GHz) and 39° (33 GHz). This results in 7-8 dB reduction in the far-field IM3 components if measured in a receive array at this angle. However, for out-of-band (OOB) radiation, one needs to also look at all angles, and this 7-8 dB reduction is not helpful for meeting the FCC OOB

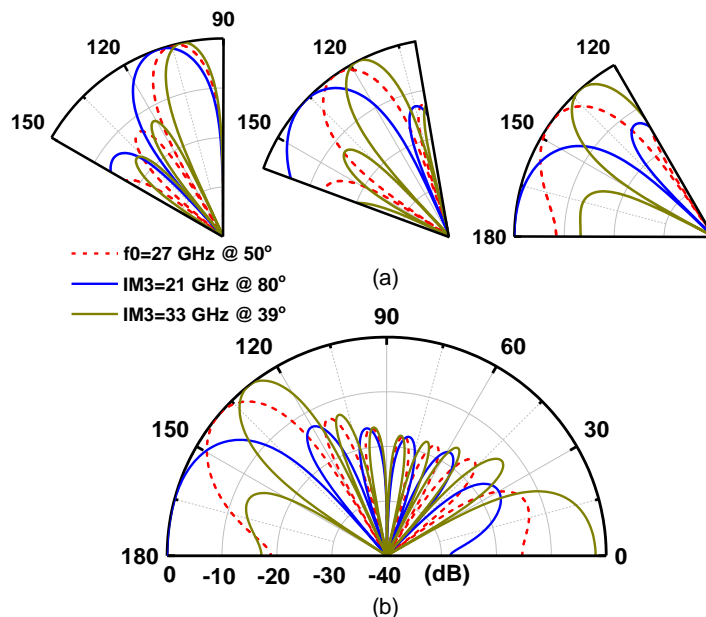


Figure 2.21: (a) Simulated IM3 patterns at 15°, 35° and 55° scan angles. (b) Simulated detailed IM3 patterns at 21 and 33 GHz when scanning to 50° with phase setting at 27 GHz in the CA mode. Normalized to the peak of each pattern.

(out-of-band) specifications.

2.6.2 System level Carrier Aggregation Simulations

Fig. 2.22a presents the simulation setup in *Matlab Simulink* to investigate the intermodulation effect of the RF channel in carrier aggregation mode. Two independently modulated 400 Mbaud 64-QAM baseband signals are generated by a random integer generator together with a rectangular QAM modulator. The signals are fed through the raised-cosine filter ($\alpha=0.35$) and are upconverted to the RF domain with carriers at 25 and 29 GHz. The two modulated signals are added using an ideal combiner before passing through the channel. The *Matlab* constellation diagram block and spectrum analyzer are then used to measure the output signal. The beamformer channel is modelled using a non-linear amplifier with 25 dB gain and 15 dBm OP1dB. Cadence simulations show an OIP3 of 20 dBm for the SiGe beamformer with 25 GHz and 29 GHz inputs, and only the odd order is considered in its input-to-output polynomial function since the 3rd-order

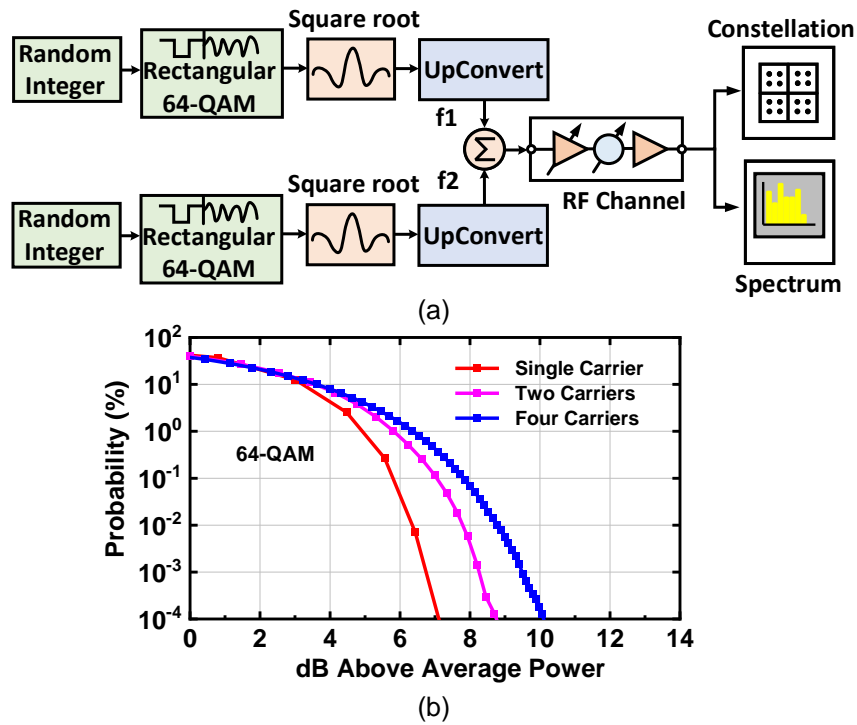


Figure 2.22: (a) Setup for carrier aggregation simulation, and (b) simulated CCDF curve for 64-QAM modulated signal with one to four aggregated carriers.

intermodulation is of interest.

The Complementary Cumulative Distribution Function (CCDF) is used to describe the probability of a signal’s instantaneous power at a specified level above the average power. The CCDF curve with one, two and four carriers with 64-QAM modulation ($\alpha=0.35$ for pulse-shaping filter) is shown in Fig. 2.22b. At 10⁻⁴% probability, the two-carrier 64-QAM signal has 1.8 dB higher peak-to-average-ratio (PAPR) than a single-carrier signal. Therefore, more backoff is needed for two-carrier aggregation in order to achieve the same EVM performance.

Fig. 2.23a presents the simulated spectrum of the output signal from the beamformer channel with two carrier components at 25 and 29 GHz. The total output power for the two carriers is 7 dBm which is 8 dB backoff, or 4 dBm and 11 dB backoff per carrier. Note that the radiated power will be 1 dB lower due to the antenna loss. The IM3 are observed at 21 GHz and 33 GHz with a -25 dBc power level. The spectrum for each modulated signal is presented in Fig.

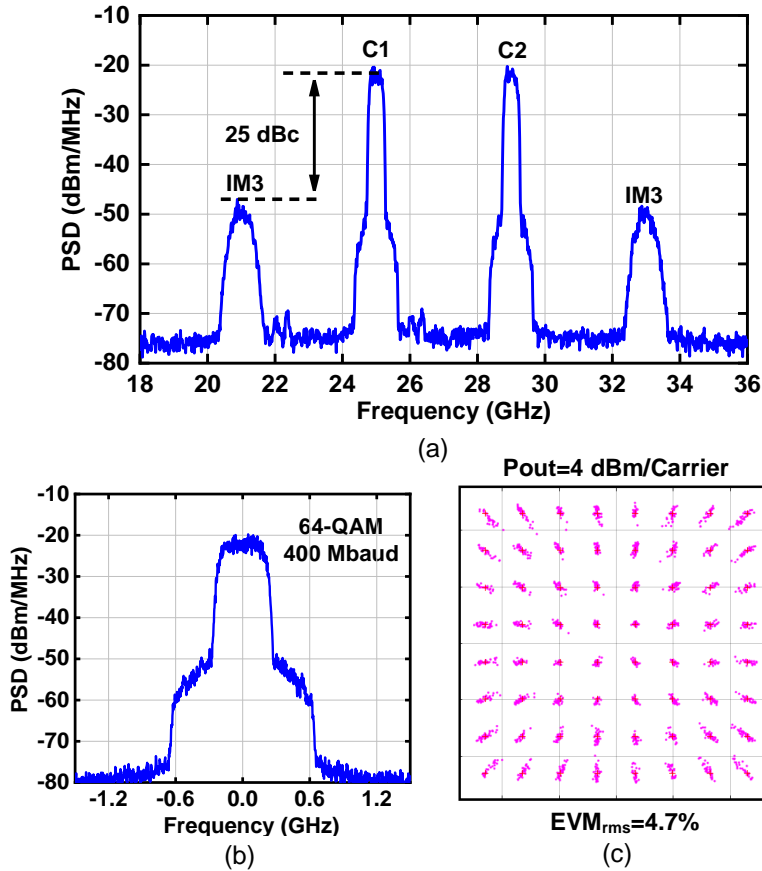


Figure 2.23: (a) Simulated broadband spectrum for output signal from beamformer with aggregated carriers at 25 and 29 GHz, (b) simulated spectrum for each modulated signal at complex baseband, and (c) corresponding constellation.

2.23b at baseband and the simulated EVM is 4.7% (Fig. 2.23c).

2.7 5G Carrier Aggregation Measurements

Fig. 2.24a presents possible architectures to implement 5G CA signals for a phased-array system. The baseband modulated signals are up-converted to RF using different mixers and LO's (carrier frequencies), and then aggregated in the RF domain using an isolated summer such as a Wilkinson network. The penalty is the use of several LO sources. However, this architecture avoids the generation of intermodulation products between the different CCs if they are first aggregated at IF and then up-converted using one mixer and one LO.

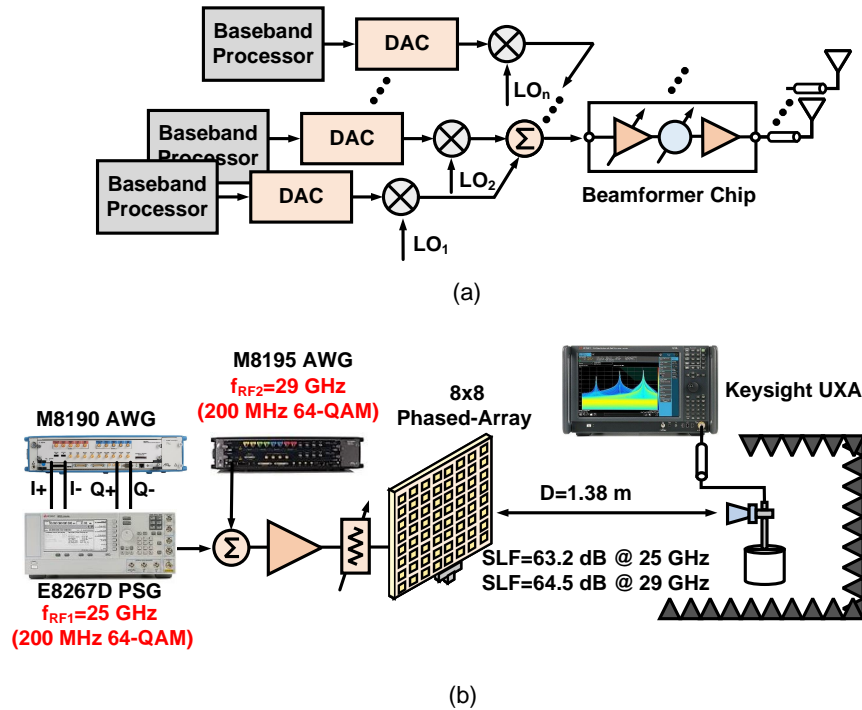


Figure 2.24: (a) Architecture for phased-array transmitter in CA mode, and (b) setup for 5G carrier aggregation measurement.

The 5G carrier aggregation measurement was performed on the wideband 8x8 phased-array with the setup shown in Fig. 2.24b, and is essentially similar to Fig. 2.24a. The first carrier is centered at 25 GHz with 200 Mbaud 64-QAM modulation and is generated by the M8190 AWG together with the E8267D vector signal generator (PSG). The other carrier with the same modulation format and centered at 29 GHz is generated directly by the M8195 AWG. The two modulated signals are aggregated using a Ka-band Wilkinson combiner and are then fed into the transmit chain. A Keysight UXA is placed on the receive side after the horn antenna, and the two CCs are demodulated separately using the Keysight 89600 VSA software.

Wideband measurements at 21 GHz to 33 GHz present calibration challenges which must be taken into account. The space loss factor, receive horn gain and cable loss all vary with frequency, and must be normalized out of the measurements (Fig. 2.25a, b, c). Since they are all part of the Friss equation ($P_r = EIRP * SLF * G_r * Cable_Loss$), it is easy to get the correction factor

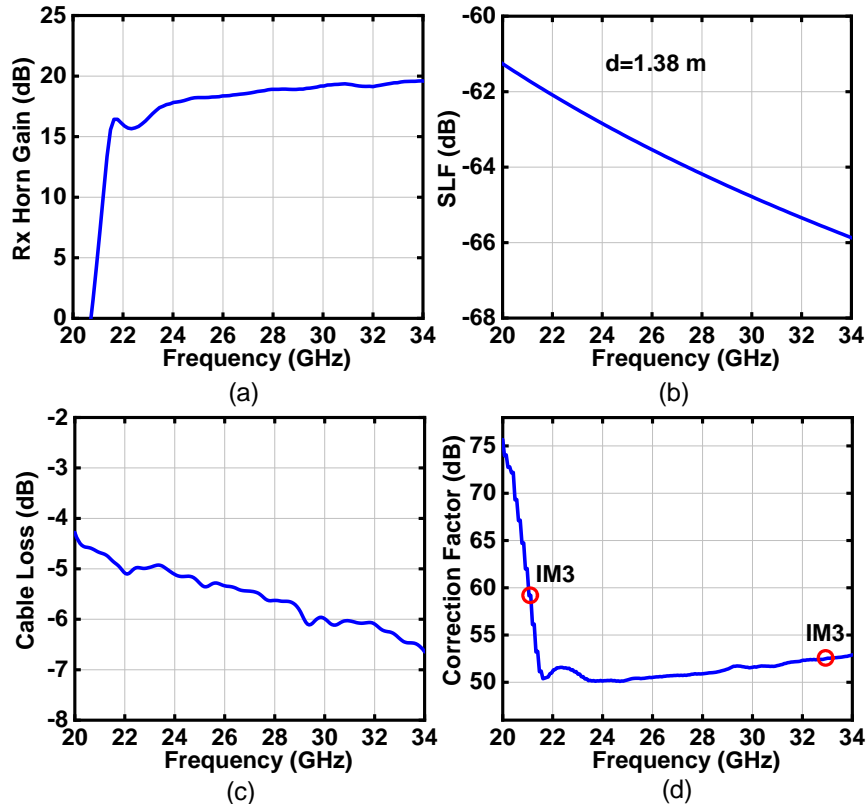


Figure 2.25: (a) Measured gain of Ka band horn antenna, (b) space loss factor at a distance of 1.38 m, (c) measured cable loss and (d) calculated correction factor ($-10 \cdot \log(SLF \cdot G_r \cdot Cable_Loss)$)

as shown in Fig. 2.25d. It is seen that the measured received power at 21 GHz should have a +6 dB correction factor for fair comparison to the measured power at 33 GHz.

Fig. 2.26a presents the measured spectrum for CA at broadside with a total radiated EIRP of 41 dBm for two CCs. Raw data is shown due to the UXA noise floor and no correction factor is included. This is a backoff of 12 dB from the $EIRP_{1dB}$ at 25 GHz and 29 GHz (~ 53 dBm), and corresponds to a radiated power of 3 dBm/antenna or 0 dBm/carrier/antenna. The IM3 components generated by the two carriers in the beamformer power amplifiers are observed at 21 and 33 GHz with a level < -34 dBc. The 21 GHz and 33 GHz IM3 levels are of equal amplitude as +6 dB should be added to the measured 21 GHz power levels. The spur at 27 GHz is generated by the driver amplifier before the array and can be improved by using a better amplifier. Note that the antenna response reduces the IM3 by 8 dB as presented in Section 2.3, and additional filtering

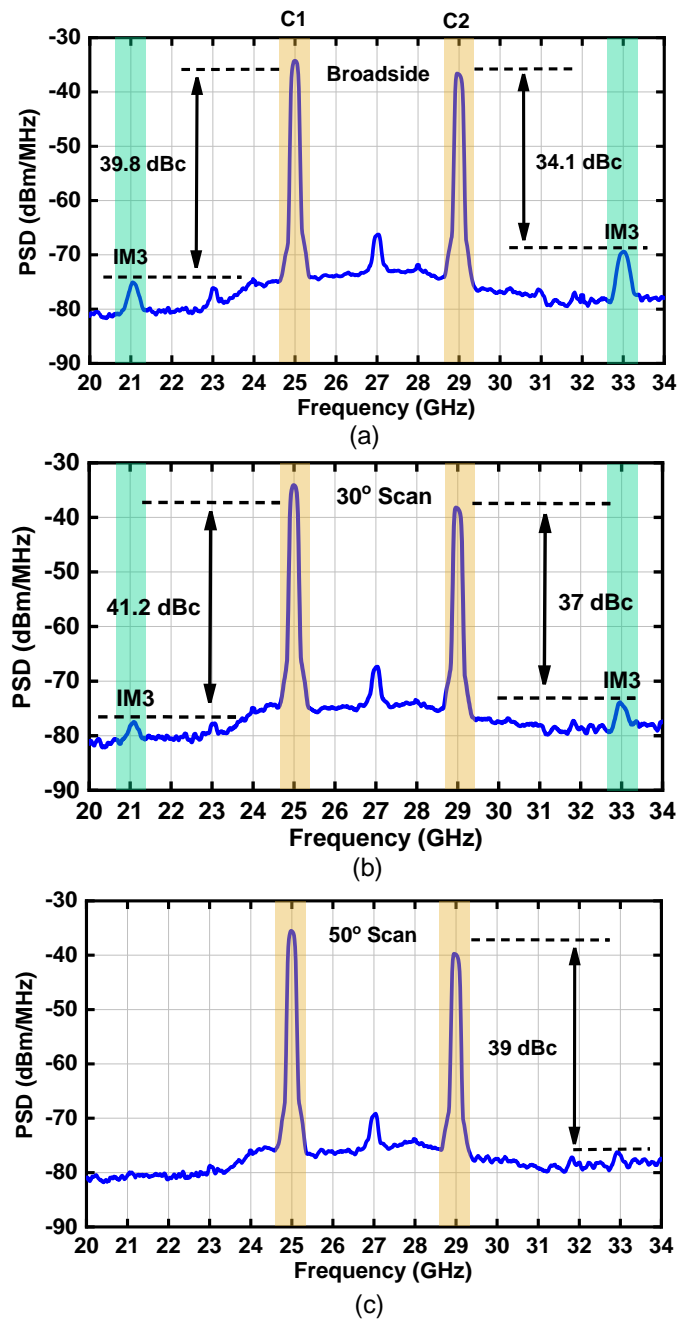


Figure 2.26: Measured spectrum for 5G carrier aggregation at (a) broadside, (b) 30° and 50° scan with 200 Mbaud 64-QAM.

can be also done in a well-designed radome. The measured spectrum at 30° and 50° scan angles are presented in Fig. 2.26b, c with a phase setting at 27 GHz. The measured IM3 components are

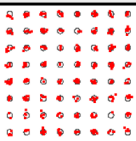
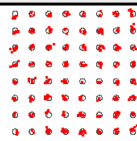
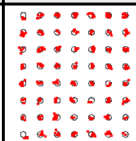
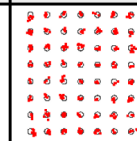
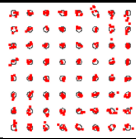
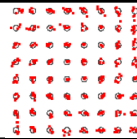
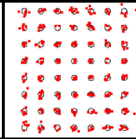
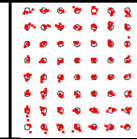
200 Mbaud 64-QAM Carrier Aggregation with EIRP=41 dBm (Two CCs)				
Scan Angle	0°	15°	30°	50°
Constellations for 25 GHz CC				
EVM	4.15%	4.25%	4.25%	4.49%
Constellations for 29 GHz CC				
EVM	4.93%	5.14%	5.06%	5.21%

Figure 2.27: Measured constellations and EVM for 5G CA using 200 Mbaud 64-QAM waveforms with 25- and 29-GHz carriers at different scan angles.

further reduced by 5-6 dB at 50° since they are not radiated at this scan angle. At 21 GHz, the measured IM3 is lower than the noise floor for the 50° case.

Fig. 2.27 presents the measured EVM and constellations at different scan angles with a total EIRP of 41 dBm. At broadside, the measured EVM_{rms} is 4.15% and 4.93% for 25- and 29-GHz CC, respectively. These values include a system-only EVM (no phased array) of 2.3% at 25 GHz and at 29 GHz. Therefore, the array contribution is 3.5% at 25 GHz and 4.4% at 29 GHz. The EVM does not degrade much even at wide scan angles. Note that in CA mode, the 5% total EVM_{rms} (worst case) occurs at an EIRP of 41 dBm which is 4 dB lower than the corresponding EIRP obtained from SC measurements (45 dBm). This is due to the increase in the PAPR when two 64-QAM signals are aggregated together and to the wideband operation of the SiGe power amplifier resulting in a lower OIP3. Table 2.2 compares this work with prior 28 GHz phased-arrays, and shows the highest peak EIRP, widest bandwidth, and with inter-band carrier aggregation operation.

Table 2.2: Comparison with State of the Art 28 GHz Phased-Arrays

Chip Parameter	This work	Tokyo ' 19 [7]	Qualcomm ' 18 [5]	IBM ' 17 [4]	UCSD ' 20 [8]	UCSD ' 18 [6]
Technology	0.18 um SiGe BiCMOS	65 nm CMOS	28 nm LP-RF CMOS 1P7M	0.13 um SiGe BiCMOS	0.18 um SiGe BiCMOS	0.18 um SiGe BiCMOS
Elements per chip	4	4	24	2x16	2x4	4
RX NF / Chip (dB)	5.5	4.1	4.4-4.7	6	4.8	4.8
RX IP _{1dB} (dBm)	-19	-26.5	N/A	-22.5	-21	-21
TX OP _{1dB} / ch. (dBm)	15-16	15.7	> 12	13.5	12	12
TX P _{DC} / ch. (mW)	340 @ P _{1dB}	299 @ 11 dBm	122 @ P _{1dB}	319 @ Psat	228 @ P _{1dB}	220 @ P _{1dB}
RX P _{DC} / ch. (mW)	156	148	42	206	163	150
Phased-Array Measurements						
Elements in array	64	8x1	2x4 + 4	2x64	2x64	64
Frequency (GHz) / Multi-Standard	23.5-29.5 / Yes	26.5-29.5 / No	26.5-29.5 / No	27.2-28.7 / No	28-32 / No	28-32 / No
EIRP (dBm)	54.8 @ P _{1dB}	39.8 @ Psat	34-35 / pol @ Psat	54 @ Psat	52 @ Psat	52 @ Psat
TX P _{DC} / array (W)	21.8 @ P _{1dB}	2.4 (EIRP=32.8 dBm)	0.98 / pol @ P _{1dB}	20.4 @ Psat	14.6 / pol @ P _{1dB}	14.1 @ P _{1dB}
Scan Range, Az (°)	+/- 60	+/- 50	+/- 45	+/- 50	+/- 50	+/- 50
EVM	-26 dB @ 200 MHz 8 dB BO from P1dB (EIRP=47 dBm) Carrier Aggregation: 25/29 GHz 200MHz -29.3 dB, -27 dB (EIRP=41 dBm)	N/A	N/A	N/A	EVM<-19.7 dB 16-QAM EIRP=44 dBm / pol EVM<-23 dB 64-QAM EIRP=41 dBm / pol	-26 dB @ 100 MHz (EIRP=46 dBm)
Maximum data rate	24 Gbps 16-QAM @ 1.3 m	1.5 Gbps 64-QAM 7.2 Gbps 512 QAM @ 5 m	N/A	N/A	2x2 MIMO: 2x20 Gbps 16-QAM 2x30 Gbps 64-QAM	18 Gbps 16-QAM @ 5 m 12 Gbps 16-QAM @ 300 m

2.8 Conclusion

This chapter presented a 23.5-29.5 GHz wideband 8x8 phased-array for multi-standard operation and 5G carrier aggregation. The array achieves a peak EIRP of 54.8 dBm. The array results in excellent performance in the E- and H-planes over the frequency range using a single-point calibration at 27 GHz. EVM measurements (-26 dB) at 24.5-29.5 GHz with 200-800 Mbaud 64-QAM waveforms resulted in 46-47 dBm EIRP which is 6-8 dB backoff from EIRP_{1dB}. Inter-band 5G carrier aggregation measurements were also demonstrated with 25- and 29-GHz carriers with 12 dB backoff and a total radiated EIRP of 41 dBm. The IM3 components are out of band and partly filtered out by the antenna response. The work shows that carrier aggregation is possible in 5G millimeter-wave system provided that the beamformer phase setting is done so as to minimize the beam squint and pattern gain loss for two carriers. Future work is still needed to optimize

carrier aggregation systems including the design of wideband power amplifiers with low IM3 products, the possible use of filters between the beamformer chip and antennas, and the design of radomes with bandpass properties.

2.9 Acknowledgment

The authors thank Kyocera International, San Diego, for assembling the arrays in their state of the art assembly line. The authors thank the Keysight team, Santa Rosa, for technical discussions and state-of-the-art equipment.

Chapter 2, in full, is a reprint of the material as it may appear in: Y. Yin, B. Ustundag, K. Kibaroglu, M. Sayginer and G. M. Rebeiz, "Wideband 23.5-29.5 GHz phased-arrays for multi-standard 5G applications and carrier aggregation", *IEEE Trans. Microw. Theory Techn.*, accepted. The dissertation author was the primary investigator and author of this paper.

Chapter 3

A 24-29.5 GHz 256-Element 5G

Phased-Array with 65.5 dBm Peak EIRP and 256-QAM Modulation

3.1 Introduction

A lot of research has been done on millimeter-wave phased-arrays for 5G applications, with 32- and 64-element arrays now demonstrated using silicon beamformer chips with excellent performance without calibration [6, 9, 10, 12]. Phased-array design is now based on the all-RF architecture at the antenna level, where gain and phase control on each channel is done in the RF domain (as opposed to the LO or IF phase shifters). In order to grow the array to a large number of element, RF beamformer chips may then employ a mixer on-chip for every 8-16 elements [4, 5, 26, 27] and then add the chips together using an IF beamformer on the printed-circuit-board (PCB). An LO splitter network is also used to distribute the LO to all chips in the array. In other implementations, the beamformer chips have an all-RF design (RF in/RF out, 2x2 quad-core or 8 or even 16-elements) and a millimeter-wave Wilkinson network is used on the

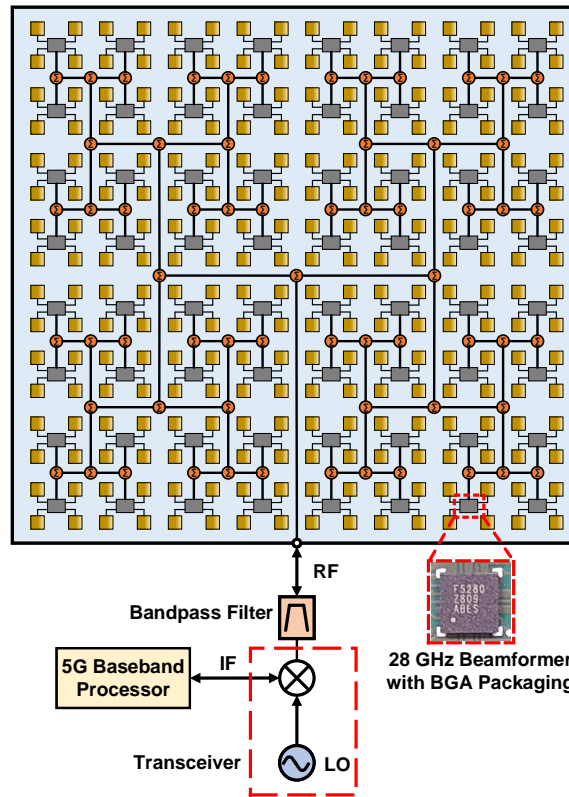
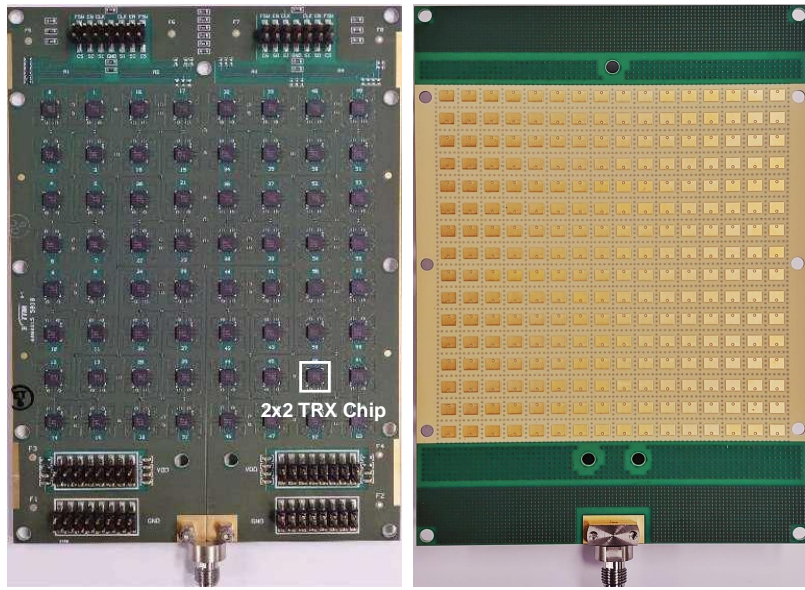


Figure 3.1: Block diagram of the 256-element phased-array transceiver based on 2x2 transmit/receive beamformer chips.

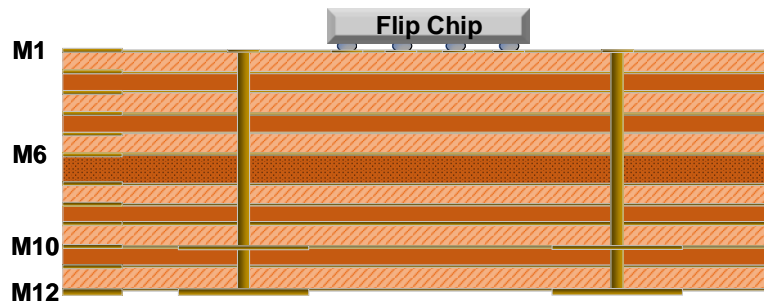
PCB to add the signals from a large number of antennas to build a large phased-array (Fig. 3.1). A single transceiver and a high-Q filter is then placed at the sum point for down-conversion and to filter out the mixer harmonics (TX mode) and interferers (RX mode). A total of 64 different 2x2 chips are used for a 256-element array.

3.2 2x2 TRX Quad Beamformer Chip

The beamformer chips are fabricated in SiGe BiCMOS technology designed for 28 GHz 5G phased-array applications (Fig. 3.1). Each chip consists of 4 RF TRX channels and one common RF port with operation range from 25 GHz to 31 GHz. Each channel has a 6-bit phase shifter, a 26-dB variable gain amplifier, a PA for TX, and an LNA for RX. The chip has a measured



(a)



(b)

Figure 3.2: (a) Top and bottom views of the 12-layer 256-element phased-array PCB using 64 2x2 beamformer chips and stacked-patch antennas. (b) 12-layer PCB stack up.

OP1dB of 11.5-12 dBm in the TX mode with a TX electronic gain of 27 dB, and NF of 5.5 dB in the RX mode, together with a RX electronic gain of 22 dB. A standard serial-peripheral interface (SPI) is implemented for fast beam switching.

3.3 28 GHz 16x16 Phased-Array Design

Fig. 3.2a presents the antenna and chip-side views of the 16x16 phased-array, which is fabricated on a low-cost 12-layer printed-circuit board (Megtron 6) with $\epsilon_r=3.62$ and $\tan\delta=0.005$

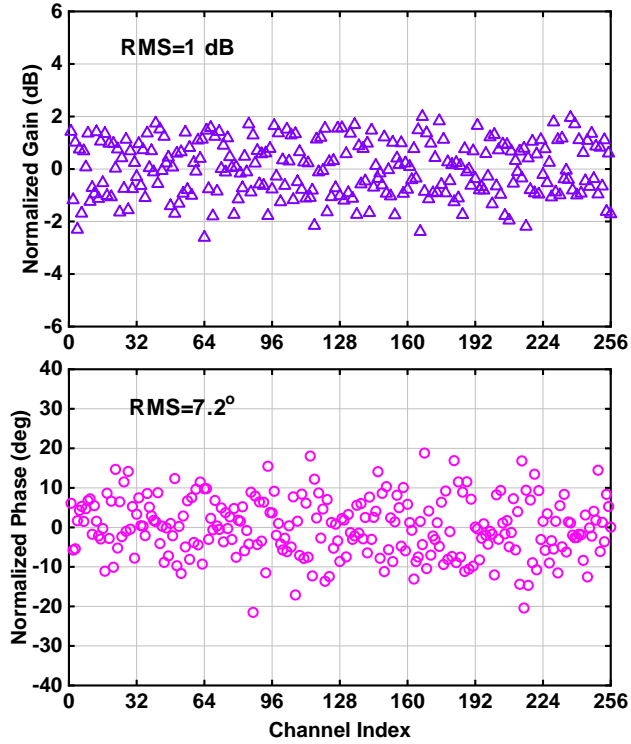


Figure 3.3: Measured channel gain and phase variation after calibration at 27 GHz.

at 30 GHz (Fig. 3.2b). The 1:64 Wilkinson network employs a co-planar waveguide (CPW) structure on M1, and commercially available 0201 resistors are used as isolation resistors for reduced cost. M2 is used as the ground of transmission lines and the Wilkinson network. M3-M5 are used for the VDD and digital SPI lines.

The antenna utilizes a stacked-patch structure on M10 and M12 for wideband operation, and M6 is used for the antenna ground. The simulated antenna S_{11} shows a -10 dB bandwidth at 24-30 GHz. The phased-array has an antenna grid of 5.3 mm (0.53λ @ 30 GHz) in the H-plane (azimuth) and 5.7 mm (0.57λ @ 30 GHz) in the E-plane (elevation), resulting in a total active area of $84.8 \times 91.2 \text{ mm}^2$. This design allows the array to scan up to $\pm 60^\circ$ in the azimuth and $\pm 50^\circ$ in the elevation planes.

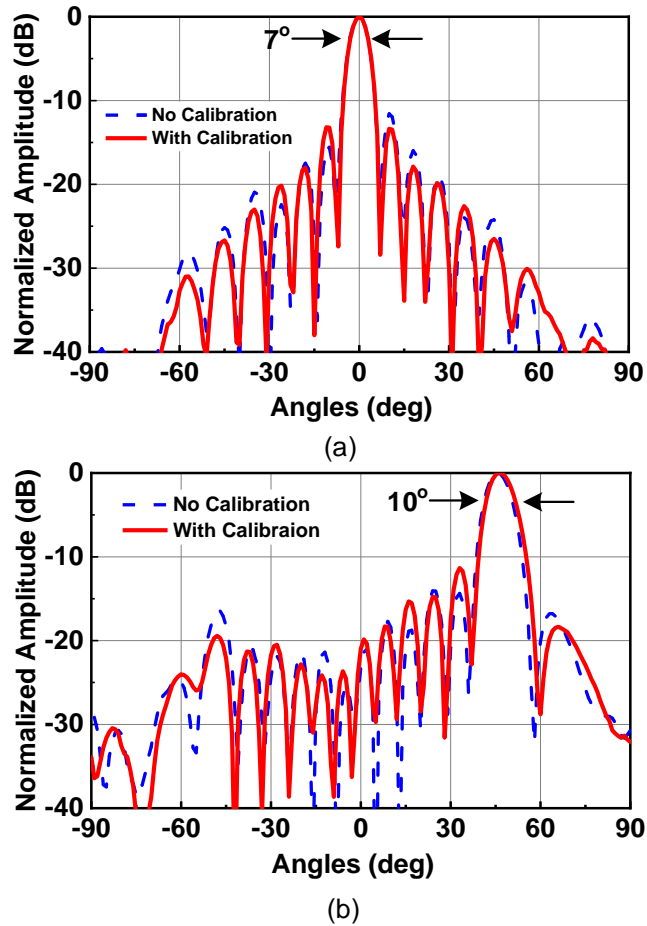


Figure 3.4: Measured H-plane (azimuth) patterns at (a) broadside and (b) 45° scan with uniform illumination at 27 GHz.

3.4 Pattern and EIRP Measurements

The phased-array is first measured and calibrated in the far field in the ETS-Lindgren 5700 chamber. The amplitude and phase responses of each channel is measured and the difference between each channel to a reference channel is compensated using VGA and phase shifter settings. Fig. 3.3 presents the measured channel gain and phase variation after calibration, the array achieves an RMS gain and phase error of 1 dB and 7.2°, respectively. The calibration is performed at 27 GHz and applied to all measurements from 24-29.5 GHz. We have found that a single-point calibration is enough to cover a 5 GHz bandwidth and results in excellent patterns at

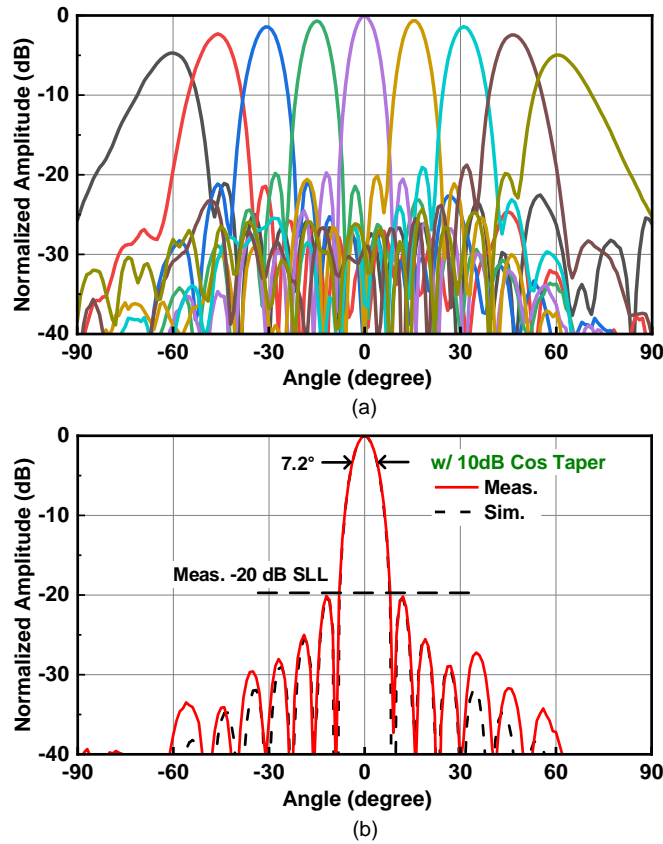


Figure 3.5: Measured H-plane (azimuth) scanned patterns to $\pm 60^\circ$ at 27 GHz with 10-dB raised-cosine taper. (b) Measured versus simulated H-plane pattern at 27 GHz.

24, 27 and 29 GHz.

Fig. 3.4 presents the measured calibrated and non-calibrated RX H-plane patterns with uniform illumination. The 3-dB beamwidth is 7° at broadside and increases to 10° when scanning to 45° which agrees well with simulation.

Fig. 3.5a presents the measured RX H-plane (azimuth) patterns with a 10-dB raised-cosine taper and scan angles up to $\pm 60^\circ$. The patterns have a -20 dB sidelobe level at all scan angles. A comparison with simulations is shown in Fig. 3.5b and excellent agreement is achieved. Similar patterns were obtained at 24 and 29 GHz (not shown for brevity).

The Wilkinson network has an ohmic loss of 7 dB. This has minimal effect in the RX mode as the system NF increases from 5.5 dB to 5.53 dB (due to the 22 dB gain in the beamformer

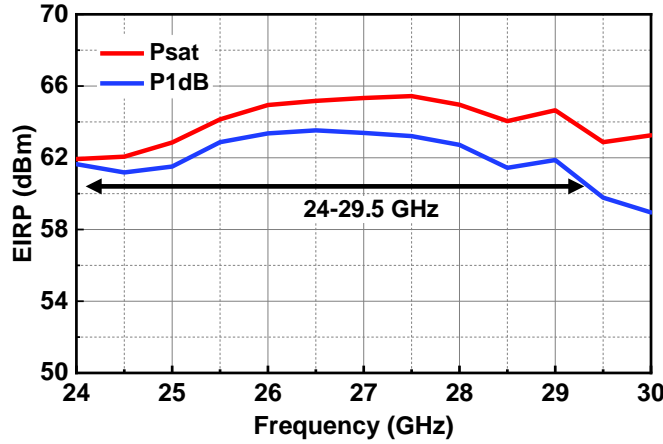


Figure 3.6: Measured EIRP of the 16x16 phased-array at P1dB and Psat.

chip). In the TX mode, the input power required at RF sum port for P1dB operation is $P_{in} = -15 \text{ dBm} + 7 \text{ dB} + 18 \text{ dB} = 10 \text{ dBm}$ (where 18 dB is the 1:64 division loss, and -15 dBm is the IP1dB of the beamformer chip). This power level can be easily attained from silicon transceivers with a typical OP1dB of 15-16 dBm.

Fig. 3.6 presents the measured effective isotropic radiated power (EIRP) of the 16x16 phased-array at broadside. A peak EIRP of 63.5 dBm and 65.5 dBm is achieved at P1dB and Psat, respectively, with a 3-dB bandwidth of 24-29.5 GHz. The EIRP can be calculated as:

$$EIRP_{1dB} = 20 \log N + 4 + 11.5 = 63.5 \text{ dBm} \quad (3.1)$$

where $N = 256$ is the number of elements, 11.5 dBm is the OP1dB of each beamformer channel, and 4 dB is the antenna element gain (Directivity - Loss, where $D = 5 \text{ dB}$ at 27 GHz, and $Loss = 1 \text{ dB}$, which is the antenna loss and the transmission-line loss between the antenna port and the beamformer port). The measurement results agree well with the expected values.

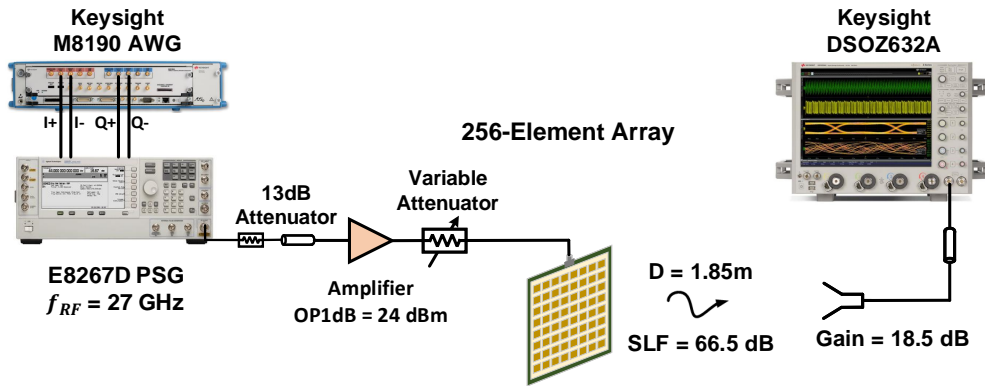
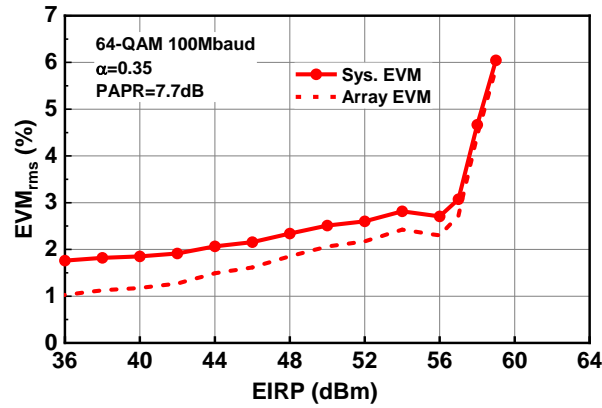


Figure 3.7: EVM measurement setup for the 28 GHz 16x16 array.

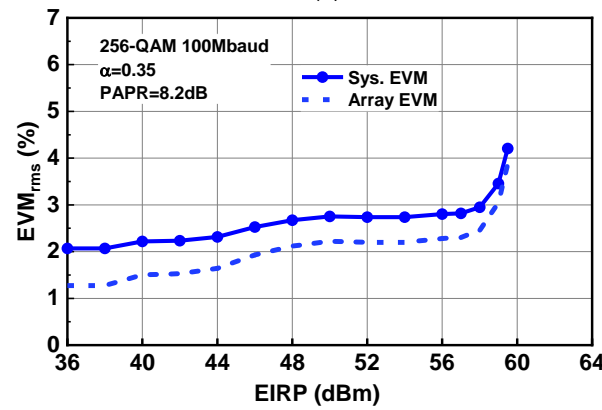
3.5 EVM Measurements

Complex modulation measurements were performed on the 256-element phased-array with the setup shown in Fig. 3.7. A Keysight M8190 arbitrary waveform generator (AWG) is used to generate 100 Mbaud 64- and 256-QAM modulated waveforms with a pulse shaping filter of $\alpha=0.35$, resulting in a peak-to-average power ratio (PAPR) of 7.7-8.2 dB. The signal is up-converted to 27 GHz and fed to the 16x16 phased-array through an amplifier. The instrumentation system (up to the phased-array input) has a measured EVM of 1.43% for 64-QAM and 1.63% for 256-QAM. A standard gain horn is used on the RX and the signal is demodulated using the Keysight DSOZ632A 63 GHz real-time scope running the VSA software.

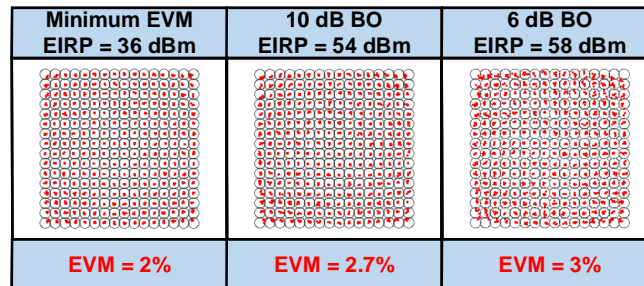
Fig. 3.8 presents the measured error vector magnitude (EVM) versus EIRP. The array adds virtually no distortion ($EVM_{array}=1\%$) at low EIRP, and results in system EVM of 3% (256-QAM) and 5% (64-QAM) at an EIRP of 58-58.5 dBm, all dominated by the PA distortion. The EVM was also measured versus scan angles and it was the same as broadside up to $\pm 60^\circ$.



(a)



(b)



(c)

Figure 3.8: EVM versus EIRP with (a) 64-QAM and (b) 256-QAM 100 Mbaud modulation. (b) Constellations of 256-QAM modulation at different EIRP levels.

3.6 Conclusion

The all-RF architecture, both at the chip level and at the PCB level, is shown to result in excellent performance for mm-wave 256-element phased-arrays. State-of-art patterns, EIRP and EVM have been demonstrated using this architecture.

3.7 Acknowledgment

The authors thank Renesas Electronics, San Diego, for sponsoring the beamformer chips used in this work. The array was assembled by Kyocera International, San Diego, using their advanced phased-array assembly production line. This work is supported in part by gifts from Keysight and Qualcomm.

Chapter 3, in part, is a reprint of the material as it appears in: Y. Yin, Z. Zhang, T. Kanar, S. Zehir and G. M. Rebeiz, "A 24-29.5 GHz 256-element 5G phased-array with 65.5 dBm peak EIRP and 256-QAM modulation", in *IEEE International Microwave Symposium (IMS)*, Jun, 2020. The dissertation author was the first author of this paper.

Chapter 4

A 1 Gbps 3.5-4.75 km Communication

Link Based on a 5G 28 GHz 8×8

Phased-Array

4.1 Introduction

The demand for high data-rate communications for mobile users has promoted a large investigation effort on phased-array systems for the fifth-generation (5G) communication standard. The 5G millimeter-wave frequency band features large bandwidth and can easily support Gbps links at 100-300 meters. Also, the beam-forming capabilities of phased-array results in directive communications which overcome the increasing path loss found at high frequencies. Over the past two years, there have been several demonstrations of 300-800 meter communication links achieved using 5G phased-arrays [4–6, 9, 10], and an 8-12 Gbps communication link was demonstrated using a 28 GHz 8×8 phased-array at a distance of 300 meters in a single beam [6]. However, 5G phased-arrays have also a potential for long distance communication links, for example 3-5 kms or even a few tens of kilometers for backhaul or point-to-point applications.

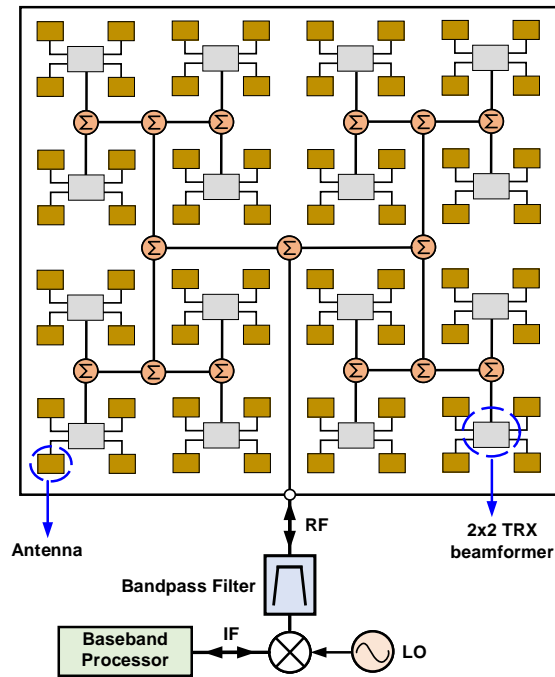


Figure 4.1: Block diagram of 28 GHz 8x8 phased-array.

In this work, a 200 Mbps to 1 Gbps communication link is demonstrated at a distance of 3.5-4.75 km with QPSK modulation. The communication link is based on two 8x8 transmit/receive high-performance phased-arrays with SiGe beamformer chips.

4.2 Wideband 8x8 Phased-Array

The 8x8 phased-array is built on a low-cost multiple-layer printed-circuit board (PCB). Sixteen 2x2 quad-TRX beamformer chips are flipped on the M1 layer along with a 1:16 Wilkinson power combining network as presented in Fig. 4.1. The 64 antenna elements are located on the other side of the PCB and are directly fed by the beamformer chips using short transmission line (between the chips and the antenna port). The antenna spacing is 0.5λ in the horizontal plane, allowing for $\pm 60^\circ$ scan angles.

The architecture of the SiGe BiCMOS 2x2 TRX beamformer is presented in Fig. 4.2 [11].

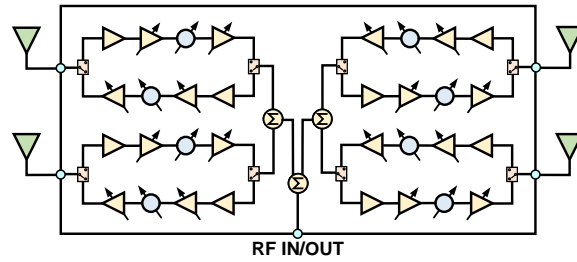


Figure 4.2: Block diagram of the 28 GHz 2x2 quad TRX beamformer.

Table 4.1: Summary of the 2x2 TRX beamformer chip

RX Mode		TX Mode	
Frequency (GHz)	27-28	Frequency (GHz)	27-28
Gain (dB)	19	Gain (dB)	24
Phase shifter bits	6	Phase shifter bits	6
Gain control	8 bits / 25 dB	Gain control	8 bits / 25 dB
NF (dB)	5.5	OP1dB (dBm)	15-16
IP1dB (dBm)	-19	IP1dB (dBm)	-7
Pdc (W)	0.64	Pdc @ P1dB (W)	1.4

Each channel contains a 6-bit phase shifter, 8-bit variable gain amplifier, a PA and LNA. In the RX mode, the chip has 19 dB electronic gain and 5.5 dB NF. In the TX mode, the chip has 24 dB electronic gain and each channel has 15-16 dBm of output power at P1dB. Note that the RX mode power consumption is relatively high since this chip has an IP1dB of -19 dBm per channel, which is quite high for a phased-array at 28 GHz.

Fig. 4.3a presents the measured H plane pattern (azimuth plane) in the TX mode at 29 GHz. A near-ideal pattern is obtained with sidelobe levels below -13 dB. The 3-dB beamwidth of main lobe is 12° and the array can scan up to $\pm 50^\circ$ without grating lobes. The measured RX patterns are nearly identical and are not shown. Note that these measurements are taken with minimal calibration as the array layout is perfectly symmetrical and the SiGe channels are all very similar in gain and phase even if from 16 different chips (to within ± 1.5 dB and $\pm 15^\circ$).

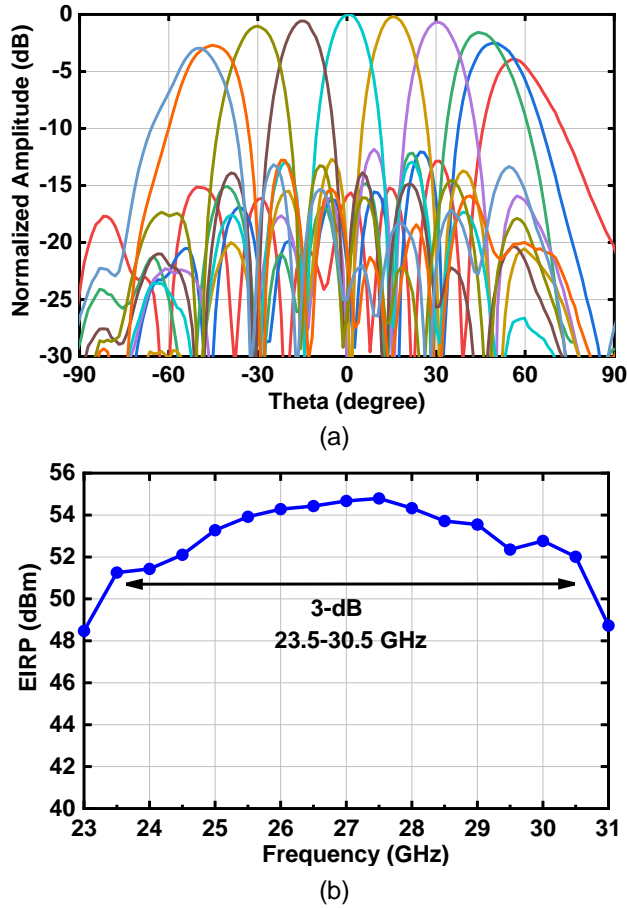


Figure 4.3: (a) Measured H-Plane patterns in the TX mode at 29 GHz and (b) measured EIRP vs frequency at P1dB.

The EIRP of 8x8 array at P1dB can be calculated as:

$$EIRP_{1dB} = 20\log N + G_{el} + P_{el} = 36 + 4 + 15 = 55 \text{ dBm}$$

where G_{el} is the antenna gain of a single antenna in the 2-D array and P_{el} is the input power at each antenna element. The Fig. 4.3b presents the measured EIRP of the 8x8 phased-array. A peak EIRP of 54 dBm at P1dB is achieved and agrees with simulations to within 1 dB. Also, the array has a 3-dB EIRP bandwidth from 23.5-30.5 GHz since it is designed for multi-standard 5G communications.

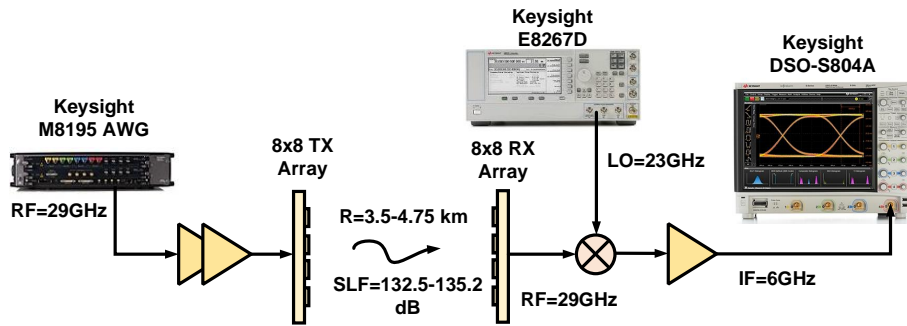


Figure 4.4: Block diagram of the 3.5-4.75 km link measurement setup.

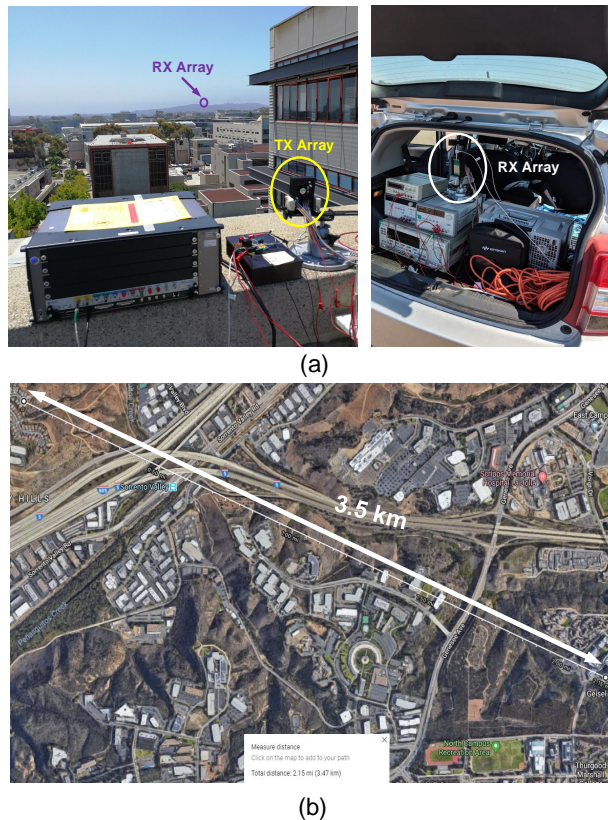


Figure 4.5: Setup photos of the 3.5 km communication link measurement: (a) views of transmit and receive setup, (b) distance on Google map.

4.3 3.5-4.75 Km Communication Link Measurements

Fig. 4.4 presents the block diagram of the communication link setup. A Keysight M8195 arbitrary waveform generator (AWG) was used to generate the modulated QPSK signal with a

Table 4.2: Link budget for 3.5-4.75 km communication

Distance (km)	3.5	4.75
Frequency (GHz)	29	29
TX EIRP (dBm)	51	51
Space loss factor (dB)	132.5	135.2
Atmospheric absorption (dB)	7	9.5
Antenna Gain (dB)	22	22
RX system electronic gain (dB)	31	31
RX system NF (dB)	7	7
Received signal power at antenna (dBm)	-66.5	-71.7
Receiver noise power (dBm)	-78.9	-78.9
Modulation Bandwidth (MHz)	650	650
Signal power received at DSO (dBm)	-35.5	-40.7
Noise power at the DSO (dBm)	-47.9	-47.9
Expected SNR (dB)	12.4	7.2

carrier of 29 GHz, and an external amplifier is employed to drive the array to P1dB. The signal was received by another 8x8 phased-array operating in the RX mode and down-converted to an IF of 6 GHz. A IF amplifier was used to maintain the received SNR before feeding into the DSO scope. The QPSK waveforms are demodulated by a Keysight S804 real-time digital sampling scope (DSO) and the Keysight Vector Signal Analysis software (VSA 89600).

A communication link was setup at distance of 3.5-4.75 km as shown in Fig. 4.5. The transmit array was placed on the sixth floor of the UCSD Jacobs Hall and the receive array was placed at Torrey Hills which was 3.5 km away from the transmit side. Mount Soledad was chosen for the 4.75 km link. The arrays were first aligned using line of sight adjustments, and then, the RX beam was moved electronically for best SNR (this is an advantage of phased-arrays as opposed to fixed reflectors).

The EIRP of the transmit array was set to 51 dBm which is 2 dB backoff at 29 GHz. Also, a QPSK modulation scheme was used since it allows operation very close to the transmitter P1dB and is immune to AM to AM and AM to PM distortions when compared to quadrature amplitude modulation (16 and 64-QAM). The simulated communication link budget at a distance of 3.5

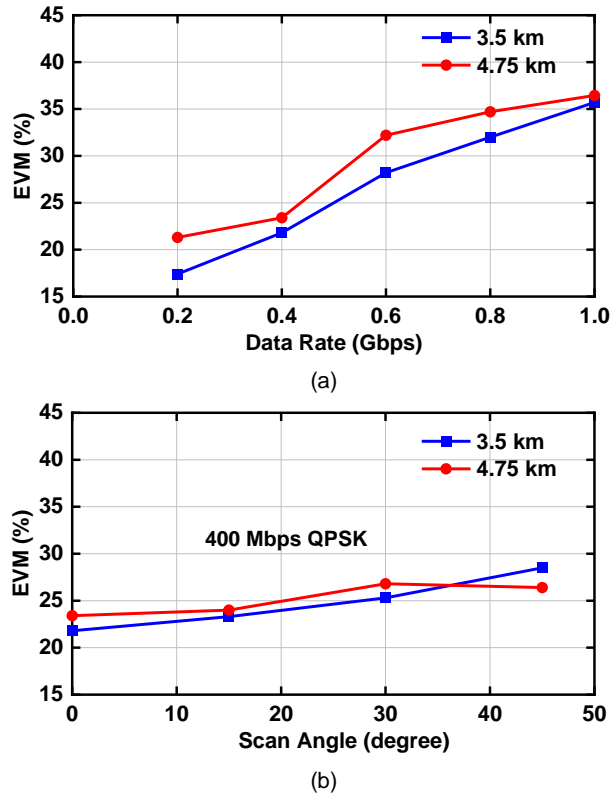


Figure 4.6: Measured: (a) EVM at different data rates with QPSK modulation and (b) EVM at different scan angles in the azimuth plane with 200 Mbaud QPSK modulation.

km and 4.75 km is presented in Table 4.2. The expected SNR are 12.4 dB and 7.2 dB for 3.5 km and 4.75 km, respectively, with 500 Mbaud QPSK modulation. Note that $\alpha=0.35$ was used, and the bandwidth for a 500 Mbaud signal is actually 650 MHz. Atmospheric attenuation of 0.1-0.2 dB/km is typically quoted at 30 GHz, but this is only for propagation at nadir (for SATCOM). A closer look at FCC document shows that the atmospheric attenuation at grazing angles to earth ($\Phi=80^\circ$) is actually 2 dB/km at 30 GHz [28].

The Fig. 4.6a presents the measured error vector magnitude (EVM) at different data rates with QPSK modulation. A maximum data rate of 1 Gbps can be achieved with EVM less than 36% (SNR=9 dB). Fig. 4.6b presents the measured EVM at different scan angles in azimuth plane with 200 Mbaud QPSK waveforms. The EVM remains below 28% (SNR=11 dB) when scanning up to 45° , and the EVM degradation versus scan is due to the reduced SNR when steering the

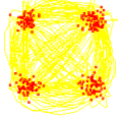
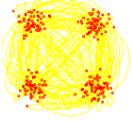
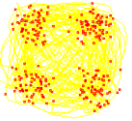
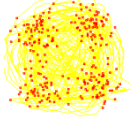
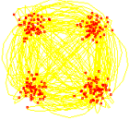
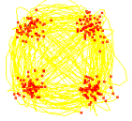
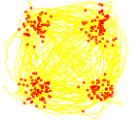
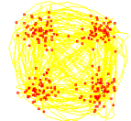
Different Data Rate QPSK (3.5 km)				
Data Rate	200 Mbps	400 Mbps	800 Mbps	1 Gbps
Constellation				
EVM	17.4%	21.8%	32%	35.7%
Scanning with 400 Mbps QPSK (3.5 km)				
Scan Angle	0 degree	15 degree	30 degree	45 degree
Constellation				
EVM	21.8%	23.3%	25.3%	28.5%

Figure 4.7: Measured constellations for the 3.5 km communication link.

beam. The measured constellations at different data rates and scan angles are presented in Fig. 4.7.

The TX array consumes 20 W at an EIRP of 51 dBm, and the receive array consumes 11 W. Knowing that an LO/mixer/down-converter can be obtained for < 2 W, the entire TX/RX phased-array system power consumption is < 23 W if fielded.

Conclusion

This work demonstrates a 1 Gbps communication link at a distance of 3.5-4.75 km using a low-cost 8x8 5G phased-array with SiGe chips. The 5G phased-array can not only support 300-800 meter links but also has potential for supporting extra long distance links for backhaul and point-to-point communications.

Acknowledgment

This work was supported in-part by Intel, and in-part, by the Laboratory for Telecommunication Sciences, Maryland, USA.

Chapter 4, in full, is a reprint of the material as it appears in: Y. Yin, T. Phelps, B. Ustundag, K. Kibaroglu, M. Sayginer and G. M. Rebeiz, "A 1 Gbps 3.5-4.75 km communication link based on a 5G 28 GHz 8x8 phased-array", in *IEEE International Symposium on Phased Array System & Technology (PAST)*, Oct, 2019, pp.1-4. The dissertation author was the primary investigator and author of this paper.

Chapter 5

A Bidirectional 36 Gbps Connectorless Connector at 2-4 cm Using a 28 GHz 2×2 Phased-Array with Position-Offset Compensation

5.1 Introduction

High-data-rate short-distance wireless communication systems are useful in a variety of environments. In a data center, they may be used to transfer data between servers at high speed. For personal use, they may be used to transfer gigabytes of data between devices, or be used as a connection between a device and a high-definition screen without the need for wires. Therefore, in situations where a high volume of data needs to be transferred between smart devices, it is advantageous to use a “connectorless connector” than a cable, as this eliminates any physical contact and improves the mechanical reliability of the connection.

One of the largest challenges for the connectorless connector is that the quality of data

Table 5.1: Summary of the 2x2 TRX array.

2x2 Array TX Performance		2x2 Array RX Performance	
Electronic Gain (dB)	21	Electronic Gain	17
EIRP bandwidth (GHz)	23.5-30.5	Electronic gain bandwidth (GHz)	23.5-30.5
TX NF (dB)	16	RX NF (dB)	5.5
Antenna gain (dB)	9	Antenna gain (dB)	9

transfer may be affected by physical misalignment between the devices. If a high antenna directivity is used, this can result in 5-10 dB less gain at wide angles on both TX and RX antennas, which can greatly reduce the data rate. This paper demonstrates high data-rate links with robust performance in extreme misalignment situations by using a 2x2 phased array on both the TX and RX units.

The goal of this work is to prove robust Gbps connections over short distance (2-4 cm) both for data transfer and in the future, as a potential to remove the coaxial connector between two industrial boxes (at the data center or any RF system). For RF systems, and as the data now is all digital and does not suffer from SNR degradation in links due to the regeneration of the digital data on the RX end, one can imagine a new set of connectorless connectors, placed in a row, and with digital transmit and receive chips transferring the RF signal at any bandwidth required (1 Gbps to 50 Gbps). Such a system requires wideband digital transceivers and phased-array transmitter and receivers, and this work presents the possibility of robust links using small phased-arrays. 5G frequencies are chosen for this work since phased-array chips and transceivers are really available and with wide bandwidth [4–6, 9, 10].

5.2 Connectorless Connector Based on a 2x2 Phased-Array

In this work, a 2x2 phased-array based on a single SiGe beamformer chip [11] is used to demonstrate a short-distance high-data-rate link. The chip is flipped on a multilayer printed circuit board (PCB) and feeds four stacked-patch antennas (Fig. 5.1). The chip is designed for

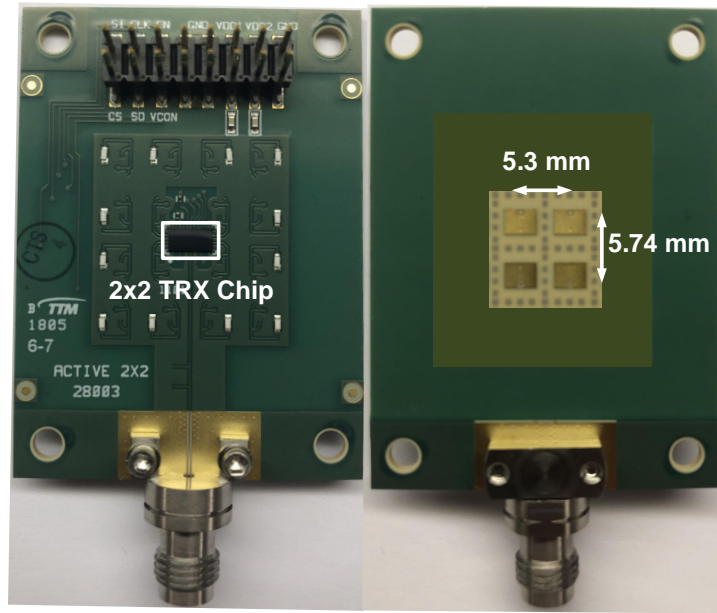


Figure 5.1: Front and back view of the 2x2 phased-array.

5G long-distance links, and each channel consists of a 6-bit phase shifter, variable gain amplifier, a PA and an LNA. Four RF channels are combined on chip with a 1:4 Wilkinson network. The antenna has a grid size of $5.3 \times 5.74 \text{ mm}^2$ ($\sim 0.53\lambda$ on a side at 30 GHz), which results in an active array size of $10.6 \times 11.5 \text{ mm}^2$ and a directivity of 11 dB at 27-28 GHz. A scanning angle of $\pm 60^\circ$ can be achieved without grating lobes. The 2x2 array has a 3-dB beamwidth of 54° allowing for a certain degree of misalignment without loss of signal (see Section 5.3). The 2x2 antenna gain is 9 dB at 27-28 GHz and includes the antenna loss and the transmission-line loss between the chip and the antennas (Table 5.1).

5.3 Link Measurements with Connectorless Connector

The measurement setup for the short distance link is shown in the Fig. 5.2. A Keysight M8195 arbitrary waveform generator (AWG) is used to generate the modulated signal with high symbol rate. The modulated signal is centered at 27 GHz and fed to a 2x2 array operating in the TX mode. Another 2x2 array is used as the receiver. A Keysight DSOZ632A 63 GHz real-time

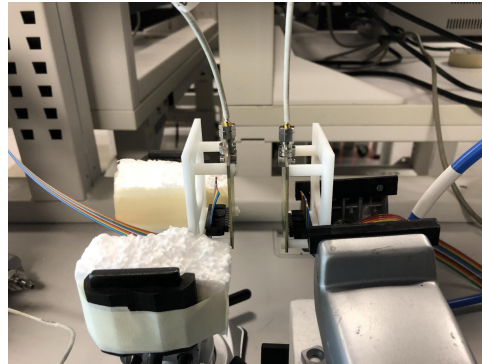
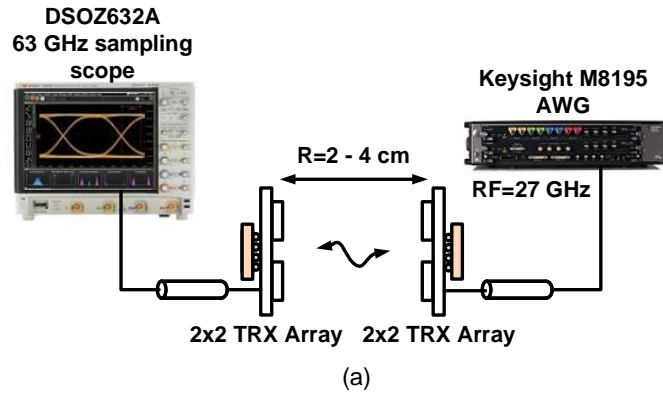


Figure 5.2: Measurement setup for 2-4 cm link: (a) block-diagram, (b) photograph.

scope is used to demodulate the signal using the Keysight VSA 89600 software suite. The two arrays are placed at a separation of 2-4 cm which is in the far field of each 2x2 array ($FF = 2D^2/\lambda = 2 \text{ cm}$ at 28 GHz).

5.3.1 No Misalignment Case

The link budget for a range of 4 cm is shown in the Table 5.2 for a center frequency of 27 GHz. The 2x2 array is designed to be very wideband (23-30.5 GHz) and this enables high baud-rate communication links with up to 7 GHz instantaneous bandwidth (Fig. 5.3). The transmit EIRP is -4 dBm which translates to -16 dBm of radiated power per antenna. The received SNR is simulated to be 40 dB for 6.5 GHz bandwidth due to the low NF of the SiGe beamformer, and the high SNR is ideal for high-order modulation waveforms. However, in this experiment,

Table 5.2: Link budget for R=4 cm

Misalignment angle (°)	0	50
2x2 Far-field distance (cm)	2	2
Modulation Bandwidth (GHz)	6.5	6.5
Space Loss Factor (dB)	34	34
EIRP (dBm)	-4	-7
2x2 Antenna RX Gain (dB)	9	6
RX Signal (dBm)	-29	-35
RX NF (dB)	6	6
Total Noise (dBm)	-70	-70
SNR (dB)	41	35

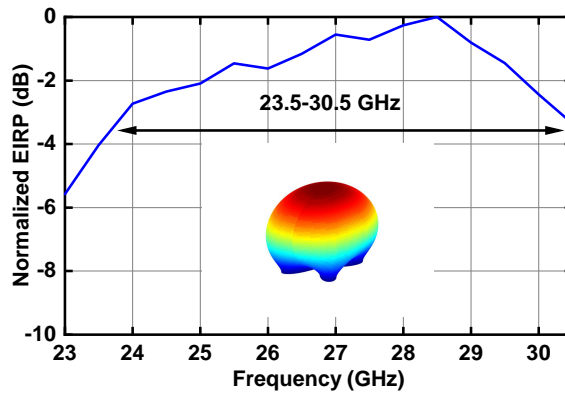


Figure 5.3: Measured normalized EIRP of the 2x2 antenna array. Inset shows 2x2 pattern at broadside.

the SNR is dominated by the AWG at 30-23 dB for 1-5 Gbaud symbol rate respectively, and the EIRP can be further reduced by ~ 5 dB without affecting the system performance.

Fig. 5.5a presents the measured error vector magnitude (EVM) relative to the constellation peak for no misalignment with 1-6 Gbaud symbol rate using 16-64 QAM waveforms. The EVM increases with the data rate due to the increased noise in the channel, but a 64-QAM / 6-Gbaud (36 Gbps) can be demodulated with $< 5\%$ EVM and low bit-error rate (Fig. 5.5b). Forward-error correction coding (FEC) can improve the bit-error rate to 10^{-10} at such an EVM.

Measurement at a distance of 2 cm yielded near identical results, but the EIRP was decreased to -10 dBm so as not to overload the RX channels. This is equivalent to -22 dBm of

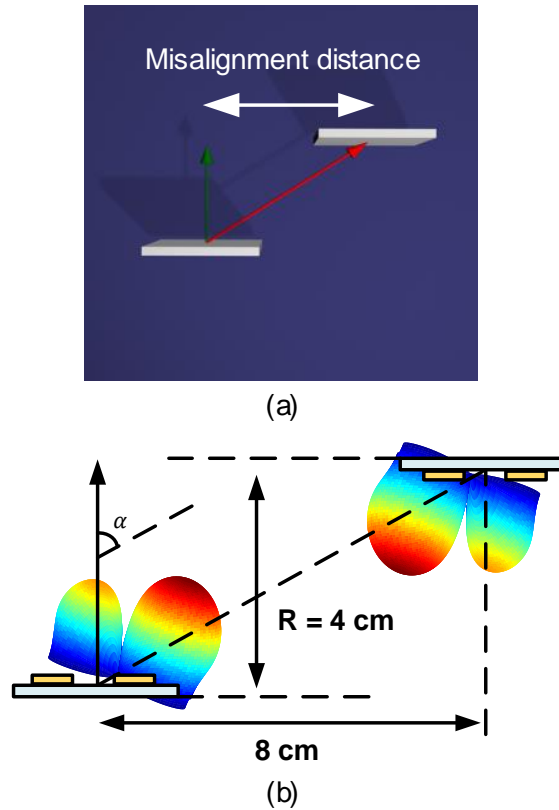
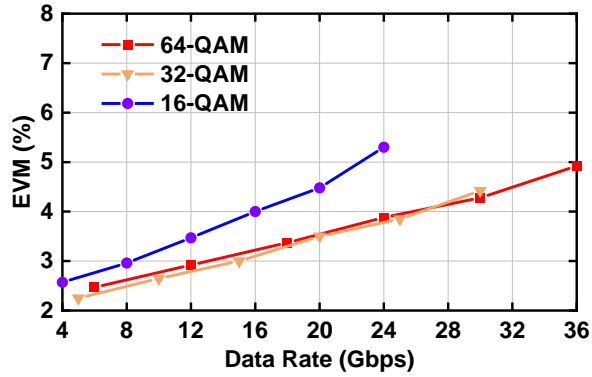


Figure 5.4: (a) Misalignment view of the two connectorless connectors, (b) two beams in alignment.

radiated power per antenna.

5.3.2 Misalignment of up to 63°

The measurement was also performed with two arrays having a misalignment distance as shown in the Fig. 5.4. A link budget for a 50° misalignment angle is presented in Table 5.2. In this set-up, the phase shifter in the 2x2 beamformer is adjusted to scan the beam of both the TX and RX arrays, so as to align to each other. The simulated patterns of the 2x2 array at broadside and scan at an angle of 50° are shown in Fig. 5.6. The gain drops by 3 dB at 50° as compared to the broadside pattern, and results in 6 dB lower system SNR (Table 5.2). Still, an SNR of 35 dB is available for a TX EIRP of -7 dBm and the system SNR remains limited by the AWG. Note that the scanned pattern results in 7.6-11.5 dB higher radiated power over the



(a)

Symbol Rate	2 GBaud	4 GBaud	6 GBaud
16-QAM Constellation			
EVM	2.96%	4%	5.32%
Symbol Rate	2 GBaud	4 GBaud	6 GBaud
32-QAM Constellation			
EVM	2.65%	3.5%	4.42%
Symbol Rate	2 GBaud	4 GBaud	6 GBaud
64-QAM Constellation			
EVM	2.92%	3.88%	4.92%

(b)

Figure 5.5: Measured: (a) EVM at different data rates, (b) constellations at different data rates with 16-QAM, 32-QAM, and 64-QAM modulation.

broadside pattern at 50° - 60° , which yields 15.2-23 dB SNR improvement in the communication link. Therefore, pattern scan is essential to maintain a high data rate connection over a large misalignment distance.

Fig. 5.7 presents the measured EVM with different misalignment distance using a 16-QAM 5-Gbaud waveform (20 Gbps). In the two-beam alignment case with pattern scanning, the

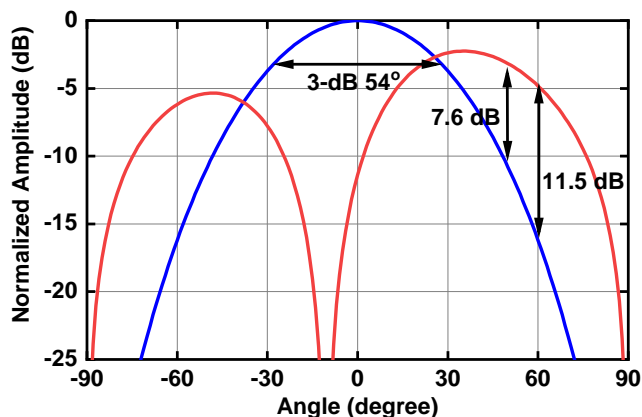


Figure 5.6: Simulated patterns of the 2x2 array at broadside and for a scan angle of 50°.

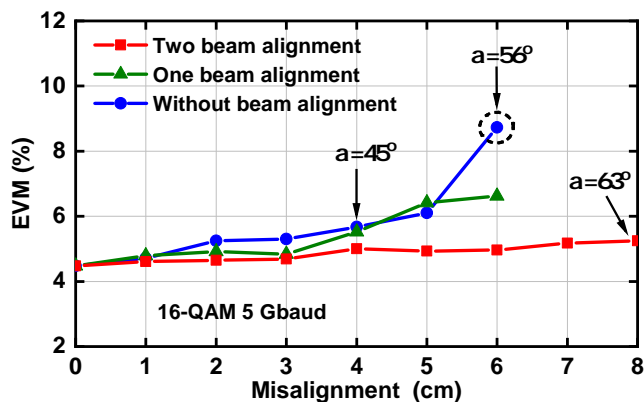


Figure 5.7: Measured 16-QAM EVM with different misalignment distance for 5 Gbaud symbol rate at $R=4$ cm.

EVM is almost constant as the misalignment distance increases. The misalignment can be as high as 8 cm ($\alpha=63^\circ$) and the EVM does not increase by more than 0.5%. This is achieved for an EIRP of -7 dBm and a 50° scan-angle setting (as in Table 5.2). The system is a very low power system, and the phased-array capabilities compensate for misalignment in any plane (elevation or azimuth).

5.4 Conclusion

This work presented the first short-range connectorless connector link using 5G frequencies and with scanning capabilities. It is seen that the use of phased-array scanning, even in a small array, greatly increases the link robustness versus misalignment and maintains a low EVM over large misalignment distances. The system requires a very low EIRP, and the maximum data rate is mostly determined by the instantaneous bandwidth of the phased-array link.

Acknowledgment

This work was supported by Intel. The authors thank Keysight for technical discussions.

Chapter 5, in full, is a reprint of the material as it appears in: Y. Yin, B. Ustundag, K. Kibaroglu, M. Sayginer and G. M. Rebeiz, "A bidirectional 36 Gbps connectorless connector at 2-4 cm using 28 GHz 2×2 phased-array with position-offset compensation", in *IEEE International Microwave Symposium (IMS)*, June, 2019, pp.1084-1087. The dissertation author was the primary investigator and author of this paper.

Chapter 6

Determining the OIP3 and Bias-Network Resonances of Phased-Array Amplifiers Using Far-Field Measurement Techniques

6.1 Introduction

The increasing demand for higher data rate of mobile users has motivated the development of complex 5G phased-arrays at millimeter-wave frequencies [1, 4–6, 8–10, 12, 26, 29]. These phased-arrays operated under high-order complex modulation waveforms such as 64-QAM and 256-QAM and the power amplifiers used at each element (in the beamformer chips) must have high linearity [30]. The measurement of the output 3rd-order intercept point (OIP3) using cables and connectors is a common way to determine the power amplifier linearity. But the amplifier OIP3 can also be measured in the far-field, since the output of each amplifier is combined in the air and this includes both the linear and the nonlinear components (intermodulation products, IM3).

The OIP3 of a single TX channel can be measured using a two-tone test (Fig. 6.1).

The input signals are continuous wave (CW) with a frequency spacing of Δf . The amplifier output spectrum includes the main output tones and the OIM3 (output intermodulation product) components. The amplifier OIP3 can be calculated as: $OIP3 = P_o + \Delta P/2$, where $\Delta P = P_o - OIM3$ [31]. Since the phased array combines the output of all transmit channels, the radiated spectrum of a phased array should be a scaled version of the single-channel amplifier for both linear and nonlinear components. A basic assumption in this work is that the IM3 products generated in the power amplifiers are coherent. The assumption is correct as the two tones input to the phased-array amplifiers are coherent and simple analysis indicates that the IM3 components are coherent too [30].

In this chapter, an experiment is performed using a 5G 28 GHz 2x2 TRX beamformer chip and a 32-element phased array built using these chips. The results show that the OIP3 determined from a single power amplifier measurement done in a coaxial 50 Ω setup, and from far-field measurements done in an antenna chamber, agree with each other provided that a couple of equations are used to translate the far-field measurements to the power amplifier port.

6.2 2x2 TRX Quad Beamformer Chip OIP3 Measurement

Fig. 6.2a presents the block diagram of the 2x2 TRX beamformer chip used [10]. The chip has four RF channels and a common RF port with an on-chip 1:4 Wilkinson network. Each channel contains a 6-bit phase shifter and a 25 dB variable gain amplifier (VGA). The chip is assembled on a printed-circuit board (PCB) with four RF connectors as shown in Fig. 6.2b. A single channel is measured and the other three are terminated with 50 Ω load. Planes A and B present the chip's common port and RF output port and are the reference planes.

Fig. 6.3 presents the measured AM-to-AM and AM-to-PM distortion of the TX channel at 28 GHz. The TX channel is operated in class A mode with an electronic gain of 33 dB and an OP1dB of 7.7 dBm. The phase distortion at P1dB is only 3.3°.

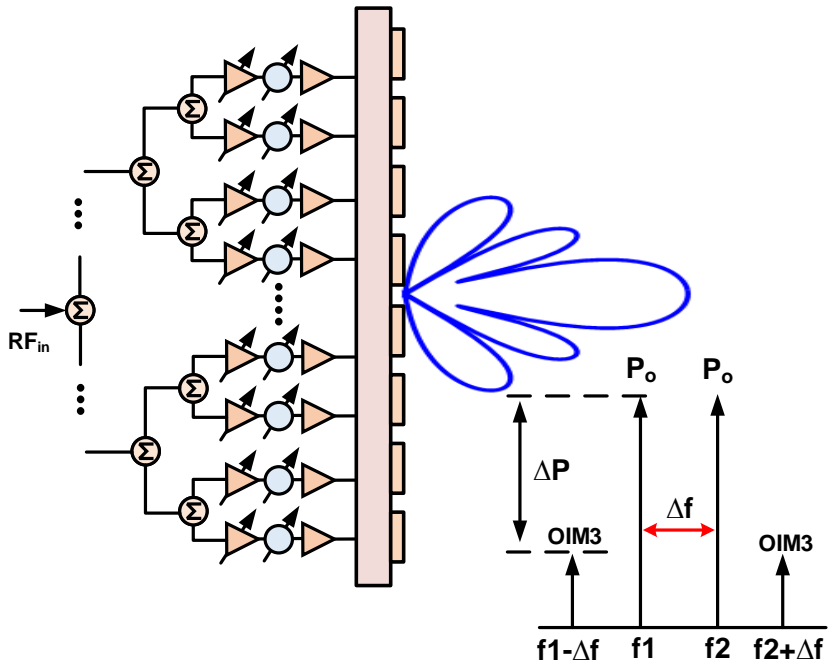


Figure 6.1: Architecture of a millimeter-wave phased array and its far-field radiated spectrum.

A two-tone test with a center frequency at 28 GHz and a frequency spacing of 10 MHz is then done (Fig. 6.4). An OIP3 of 17 dBm is found for low input powers and agrees well with the expected result for class-A operation ($OIP3 = OP1dB + 9.6 dB$). Note that at higher input powers, there is interaction between the IM3 and IM5 components resulting in a dip from the linear IM3 response. Therefore, it is essential that the IM3 measurement be done at low enough powers so as to form a weakly nonlinear system and higher-order nonlinear terms are negligible. Fig. 6.4b shows that the IM3 components grow 3x faster than the linear components, as expected [31].

6.3 28 GHz 4x8 Phased Array RF Performance Measurements

The far-field OIP3 measurement is performed on a 28 GHz 32-element phased array with an architecture shown in Fig. 6.5a ([6, 8, 10, 12]). The array is based on 2x2 quad TRX beamformer chips as described in the Section 6.2. The beamformer chips are flipped on one side

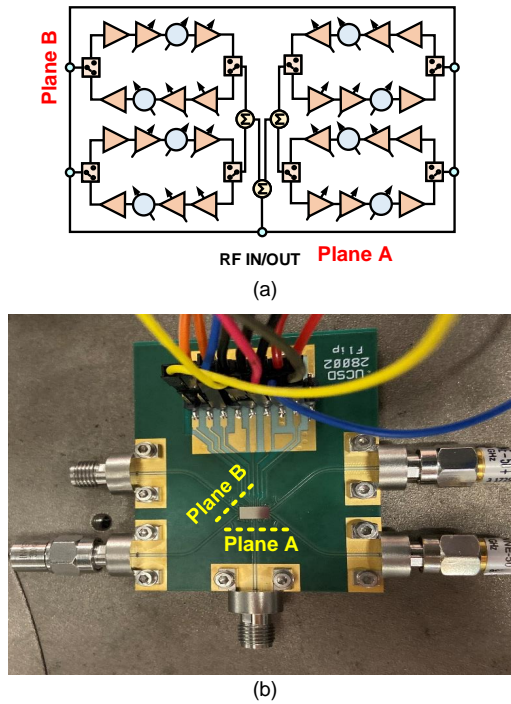


Figure 6.2: (a) Block diagram of the 2x2 TRX beamformer chip and (b) picture of the test PCB board for single-channel OIP3 measurements.

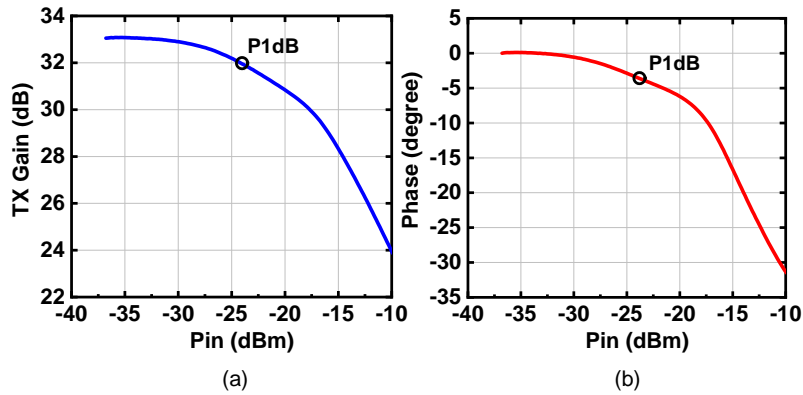


Figure 6.3: Measured (a) AM-AM and (b) AM-PM distortion for a single TX channel of the 2x2 TRX beamformer chip at 28 GHz.

of a low-cost printed-circuit-board (PCB) and the antenna elements with a stacked patch structure is designed on the other side of the board. The input power is distributed to eight beamformer chips using a Wilkinson network on the PCB.

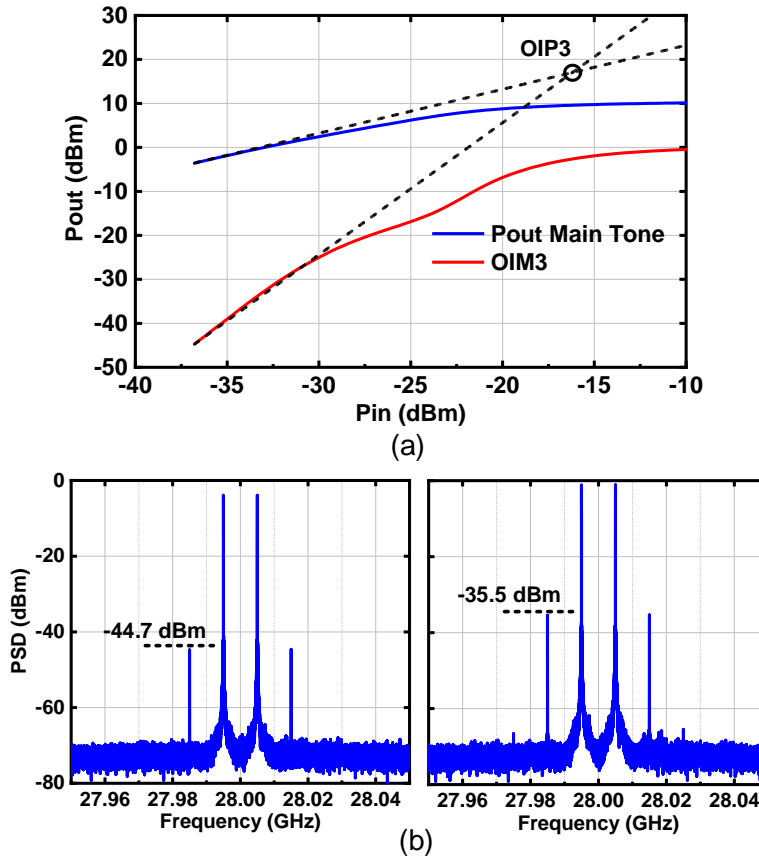


Figure 6.4: Measured (a) output power versus input power for the 2x2 beamformer chip at 28 GHz, and (b) output IM3 spectrum for a single channel with -36.7 and -33.7 dBm input power to the beamformer chip.

Fig. 6.5b presents the fabricated phased-array board with an antenna aperture of 4.2×2.4 cm². The 4x8 array employs an antenna grid size of 5.3 mm (0.53λ @30 GHz) on the horizontal (azimuth) axis and 6 mm (0.6λ @30 GHz) on the vertical (elevation) axis, and is capable of scanning $\pm 60^\circ$ in the azimuth plane and $\pm 35^\circ$ in the elevation plane at 27-28 GHz without grating lobes.

Fig. 6.6a presents the measured H-plane (azimuth) patterns at 27 GHz in the Tx mode with uniform illumination. Measurements are done to $\pm 55^\circ$ and with < -12 dB sidelobes. The array has a measured EIRP of 42 dBm at P1dB and 46 dBm at Psat for broadside illumination (Fig. 6.6b). Measurements agree well with calculations done using $EIRP_{sat} = 20\log N + G_{ant} +$

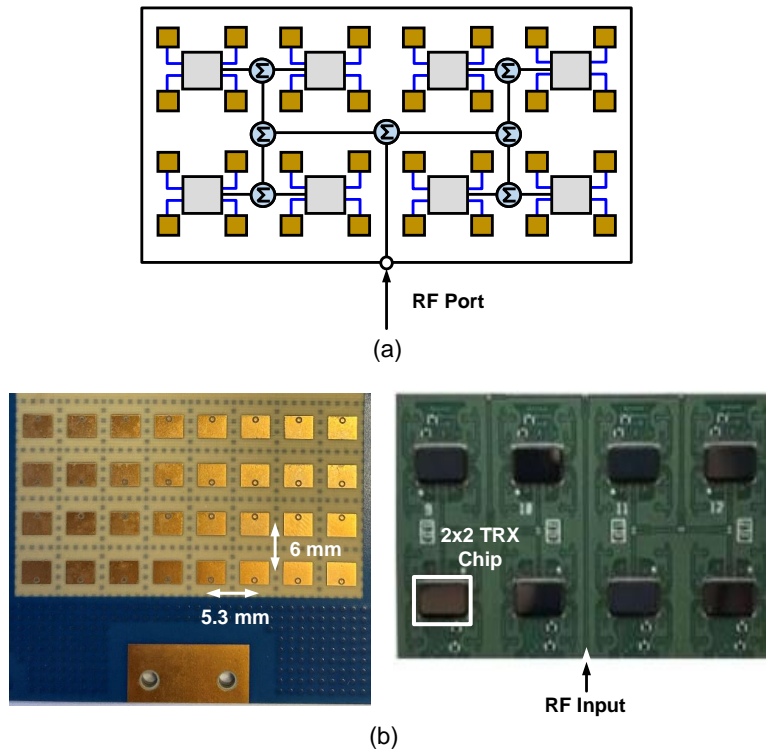


Figure 6.5: (a) Block diagram of the 28 GHz 4x8 phased-array, (b) front and back view of the phased-array board.

$P_{element} = 30 + 4 + 12 = 46$ dBm, where $G_{ant} = Directivity - Loss$, with $Directivity = 5$ dB and $Loss = 1$ dB and includes antenna loss (0.7 dB) and the transmission line loss between the chip and the antenna (0.3 dB).

6.4 Far-Field OIP3 Measurements Using the 4x8 Phased Array

The setup for far-field OIP3 measurements is shown in Fig. 6.7a. Two CW tones are generated by the Keysight N5247B PNA-X with a center frequency of 28 GHz and with 10 MHz spacing, and is the same as the single-channel measurements. The phased array is operated in the TX mode, and a horn antenna is placed at a distance of 0.4 m.

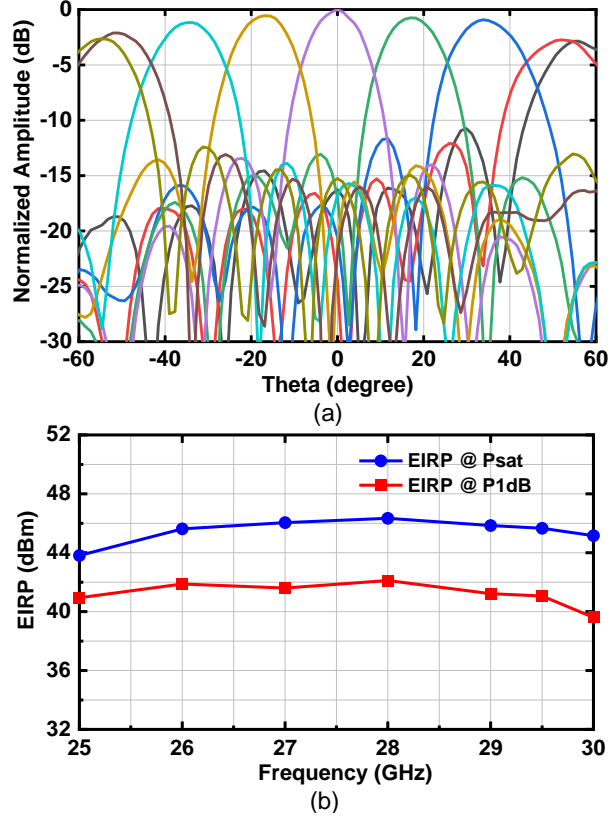


Figure 6.6: (a) Measured H-plane (azimuth) patterns at 27 GHz in the Tx mode. (b) Measured EIRP versus frequency.

The phased-array system can be modelled using the Friis blocks shown in Fig. 6.7b. The power amplifier IM3 components (i.e., OIP3) pass by a block which represents the transmit antenna gain with coherent power addition of N-amplifiers ($G_{Co-Tx}=34$ dB), then by a block which represents the space loss factor ($SLF=(\lambda/4\pi R)^2=-53.4$ dB), and then by a block which represents the receive horn antenna and cable loss ($G_{Rx}=18.5$ dB). Note that all of these blocks are highly linear and do not generate any IM3 components. The measured $OIM3_{Rx}$ are then calculated as:

$$OIM3_{Rx} = OIM3_{amp} + G_{Co-Tx} + SLF + G_{Rx} \quad (6.1)$$

where $G_{Co-Tx} = 20\log N + G_{ant}$. Note that G_{Co-Tx} is not the array antenna gain G_t , commonly given as $G_t = 10\log(N) + G_{ant}$. The $OIM3_{amp}$ (which is the average over all amplifiers used in

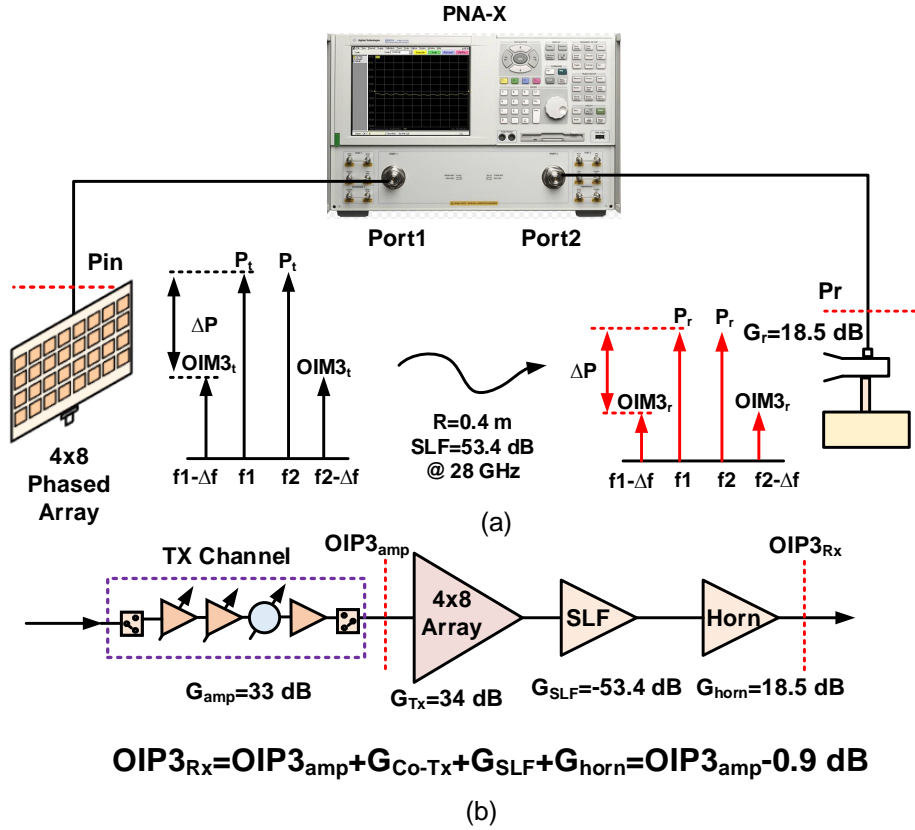


Figure 6.7: (a) Setup for far-field OIP3 measurement using a 4x8 phased array, (b) Friis block diagram for OIP3 in the far-field.

the phased-array) can be found using:

$$OIM3_{amp} = OIM3_{Rx} - G_{Co-Tx} - SLF - G_{Rx} \quad (6.2)$$

This is now done for two different transmit powers and the $OIP3$ is determined. The same Friis equation can be used to determine the amplifier $OIP3$ as:

$$OIP3_{amp} = OIP3_{Rx} - G_{Co-Tx} - SLF - G_{Rx} \quad (6.3)$$

with $G_{Co-Tx} = 34$ dB, $SLF = -53.4$ dB and $G_{Rx} = 18.5$ dB.

Fig 6.8 presents the measured linear and IM3 powers at the horn for various levels of input

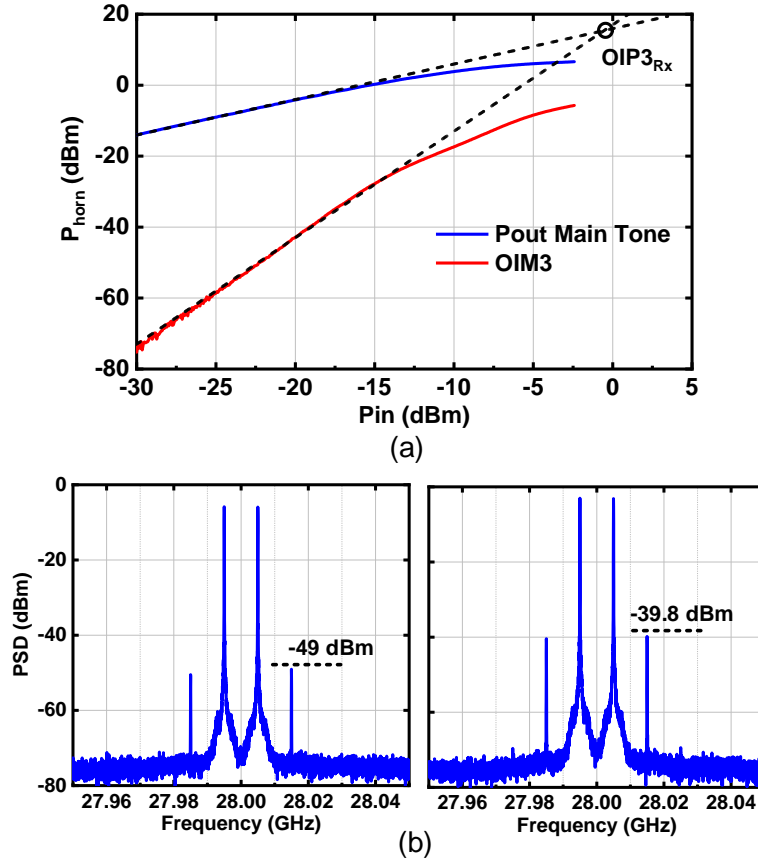


Figure 6.8: Measured (a) received power at the horn versus input power to the array ($\Delta f=10$ MHz), and (b) IM3 spectrum at the horn with -22.4 and -19.4 dBm input power to the 32-element phased-array.

power, and an $OIP3_{Rx}$ of 15.7 dBm is found. Using (6.3), this translates to an $OIP3_{amp}=16.6$ dBm and agrees well with the single-channel measurements of $OIP3=17$ dBm. There is a 0.4 dB discrepancy between the obtained average $OIP3$ using far-field measurements and using single-channel measurements. This is because of a slight 1dB degradation of the 32-element phased array due to increased temperature and due to the averaging effect of 32 power amplifiers.

Fig. 6.9 presents the power of main tone, $OIP3$ and $OIM3$ (all referenced back to the PA) from PA output versus different frequency spacings (Δf) between two tones. The main tone is easily referenced back using $P_{Rx} = P_t \cdot G_t \cdot SLF \cdot G_{Rx}$, and $P_t = 10 \log N + P_{element}$. As Δf changes from 1 kHz to 10 MHz, the output linear and nonlinear terms remain constant, as expected.

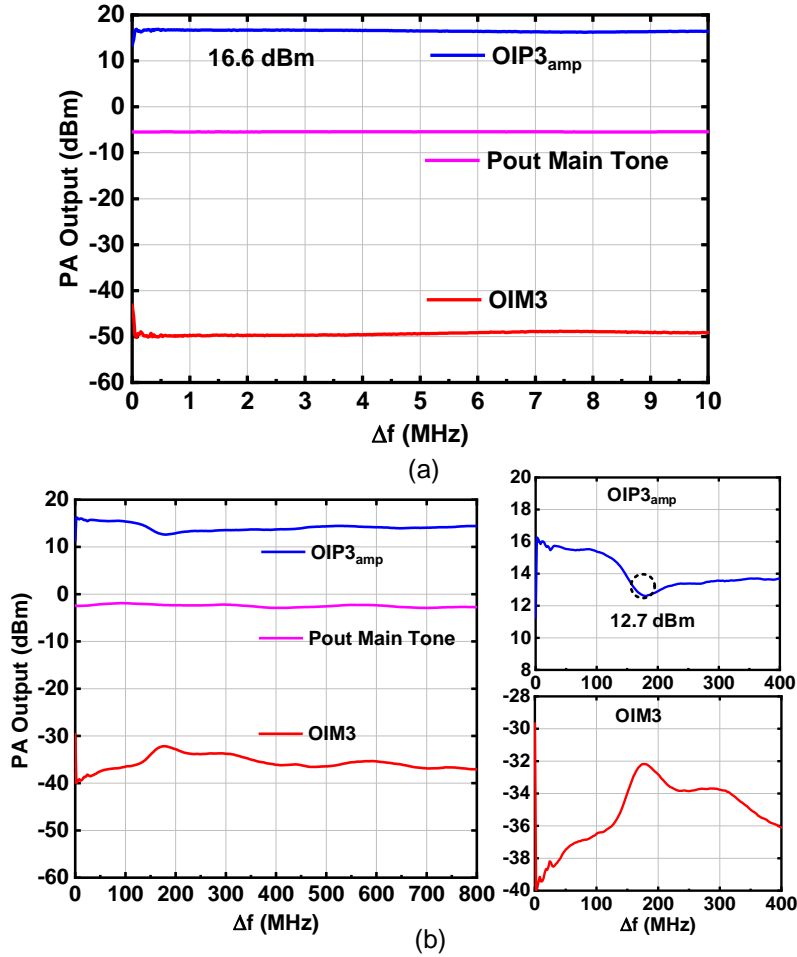


Figure 6.9: Measured output power versus frequency spacing for (a) 1 kHz to 10 MHz with $P_{in}=-22.4$ dBm (array input power) and (b) 1 kHz to 800 MHz with $P_{in}=-19.4$ dBm (array input power). All output powers are referenced to the PA output of a single channel using Equation (5.2), (5.3).

When Δf changes from 1 kHz to 800 MHz, an increase is observed for OIM3 components at $\Delta f=174$ MHz and is due to resonances in the PCB bias network. These resonances are due to the inductance between the chip and the decoupling capacitors, and are typically in the 40-1000 MHz range. This technique therefore allows the user to easily characterize resonances in the PCB bias network which can reduce the OIP3 and degrade the phased-array modulation performance. At $\Delta f=174$ MHz, the OIP3 drops from 16.6 dBm to 12.7 dBm, which is significant and can increase the error vector magnitude (EVM) for wideband waveforms.

6.5 Conclusion

This chapter presents a method of determining the OIP3 of amplifiers used in phased-arrays using far-field measurements. An equation translating the OIP3 measured in the far-field to a single amplifier output in the array is derived and proved to be valid by experiment. The technique can also detect resonances in the chip bias network.

6.6 Acknowledgment

The authors thank Kyocera International, San Diego, for assembling the array in their advanced assembly production line.

Chapter 6, in full, is a reprint of the material as it may appear in: Y. Yin and G. M. Rebeiz, "Determining the OIP3 and bias-network resonances of phased-array amplifiers using far-field measurement techniques", *IEEE Antennas and Wireless Propagation Letters.*, submitted. The dissertation author was the first author of this paper.

Chapter 7

A 37-42-GHz 8×8 Phased-Array With 48-51-dBm EIRP, 64-QAM 30-Gb/s Data Rates and EVM Analysis Versus Channel RMS Errors

7.1 Introduction

The millimeter-wave spectrum is currently used for the fifth-generation (5G) standard for high data-rate and low-latency links for both mobile users and fixed wireless access [1, 2, 32]. The 5G standard supports licensed bands at 23.5-30.5 GHz and 37-43 GHz, and an unlicensed band at 57-71 GHz. The beam steering capabilities of phased-arrays compensate for the high path loss at mm-waves and allows for long-distance communication links. Also, low-cost silicon chips allow the construction of affordable phased-arrays.

Over the past few years, there have been several demonstrations of phased-arrays at 28 GHz [4–7, 10, 11, 29, 33–36], 39 GHz [12, 26, 37] and 60 GHz [14–17, 38–40]. For example, a 28

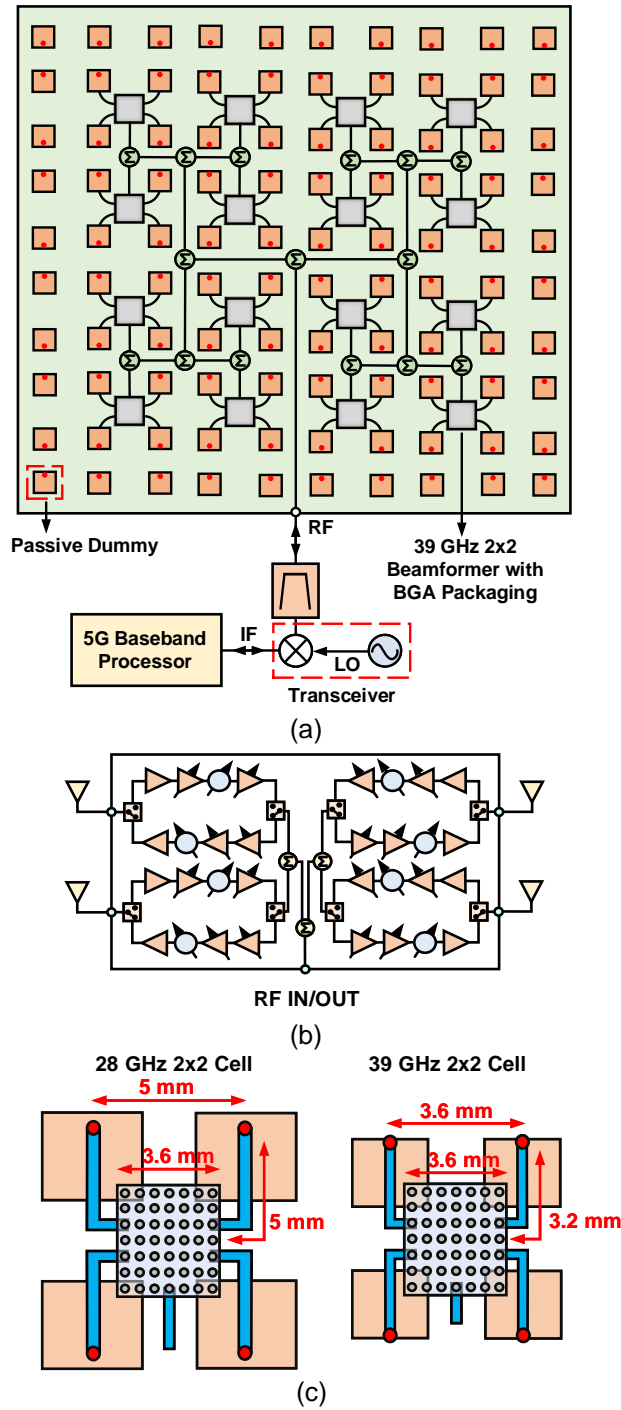


Figure 7.1: (a) Block diagram of the 39 GHz 8x8 phased-array, and (b) 2x2 39 GHz 5G TRX beamformer chip, and (c) dimensions of antennas and feed lines for the 2x2 cell at 30 GHz and 42 GHz. The 2x2 chip fits well within the 37-42 GHz antenna period.

GHz 8x8 phased-array is used in [6] to demonstrate a 12 Gbps link at 300 meters without any calibration. Also, there are demonstrations of 28 GHz dual-polarized silicon chips and phased-arrays with up to 32 elements on a single chip [4, 5] and [35, 36]. Phased-arrays and their related silicon chips have also been demonstrated at 44-46 GHz for Q-band satellite communication subarrays (up to 16 elements) [41, 42]. The 60 GHz frequency range has also been an active area of research with demonstrations of phased-array communication links at distances ranging from a few meters up to 800 meters [14–17, 38–40]. Finally, the 39 GHz region has gathered some attention in the past two years with some array demonstrations [12, 26, 37].

This chapter is an expanded version on [12], and presents the design and construction of a low-cost 8x8 39 GHz phased-array focusing on its system performance including local oscillator leakage and rejection. Also, a detailed analysis on the effect of amplitude and phase errors on the radiated EVM performance of a phased-array is presented. The paper concludes with detailed measurement showing patterns, EIRP, and EVM versus scan angle. Also, the EVM performance of the phased-arrays with and without calibration is presented and discussed.

7.2 Phased-Array Architecture and Beamformer

The 39 GHz phased-array employs the 2x2 beamformer architecture shown in Fig. 7.1a-b. The beamformer chips are flipped on one side of a low-cost multilayer printed-circuit board (PCB) and the antenna elements are placed on the other side of the board. The antennas are connected to the silicon beamformer chips using short transmission-lines, which ensures minimal loss and better system efficiency (Fig. 7.1c). The design is also symmetric and minimal calibration is needed for good operation. Also, a uniform heat distribution is obtained over the phased-array since the chips are distributed uniformly over the 2-D antenna grid. A transceiver chip is used at the sum port, and a high-pass filter after the transceiver chip greatly reduces the image response and any LO leakage. Note that a similar topology has been presented at 28 GHz in [11],

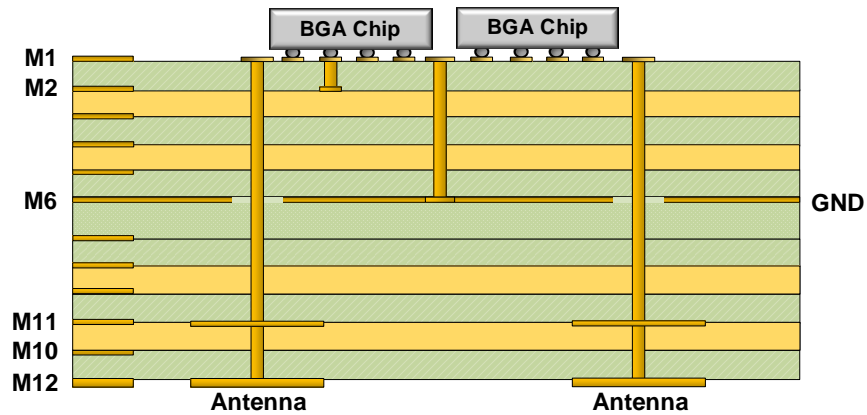


Figure 7.2: Stackup of the low-cost 12-layer PCB board.

Table 7.1: Summary of the 2x2 SiGe TRX beamformer chip

Receive mode		Transmit mode	
Gain (dB)	26	Gain (dB)	25
NF (dB)	5.5	Pout (dBm) @ P1dB / @ Psat	10-11 / 12
IP1dB (dBm)	-28	IP1dB (dBm)	-13
Gain Control	25	Gain Control (dB)	25
Phase Shifter	6-bit	Phase Shifter	6-bit
DC power / Ch (W)	0.15	DC power / Ch (W)	0.25
VDD (V)	2.5	VDD (V)	2.5

and this work expands on previous publications in terms of designing better cross-polarization performance, system measurements and EVM investigations versus RMS gain and phase errors.

The 2x2 TRX beamformer chip is fabricated in a SiGe BiCMOS technology with 0.5 mm ball-grid array (BGA) packaging (Fig. 7.1b). The chip has four RF channels and a common RF port with an on-chip 1:4 Wilkinson network. Each channel contains a 6-bit phase shifter with 5.6° phase resolution and a 25 dB variable gain amplifier (VGA) (Table 7.1). In the RX mode, the chip has 26 dB electronic gain and 5.5 dB noise figure (NF), and consumes 150 mW per channel. The electronic gain is defined as the measured $S_{21}+6$ dB with one channel being activated and the other three channels terminated. The 6 dB takes into account the added Wilkinson loss which is not present when all channels are energized. The relative high power consumption is due to

the IP1dB of -28 dBm (OIP1dB of -3 dBm at the common port when one channel is activated) resulting in a VGA OP1dB of +2 dBm when the SPDT switch (after the VGA) and the Wilkinson loss are taken into account. In the TX mode, the chip has 25 dB electronic gain and an OP1dB of 10-11 dBm, and consumes 250 mW per channel at P1dB. The chip performance listed in Table. 7.1 includes the BGA packaging. The digital control of the chip is implemented through a serial-peripheral interface (SPI).

The 8x8 phased-array is built on a low-cost 12-layer PCB as shown in Fig. 7.2. The substrate material is Panasonic Megtron-6 with $\epsilon_r=3.2\sim 3.5$ and $\tan\delta=0.006$ (at 40 GHz). Sixteen of the 2x2 TRX beamformer chips are placed on the M1 layer, and are connected to a 1:16 Wilkinson network on M1-M2 to the sum port. The Wilkinson network employs commercially available resistors for reduced cost. The SPI lines and VDD are routed on M3-M5. Also, passive antennas terminated with 50 Ω loads are placed around the 8x8 active elements to improve the performance of the edge elements. The antenna is placed on M10 and M12 layers with a stacked-patch structure [23] to enhance the bandwidth and M6 is used as the antenna ground. A symmetric PCB is used to reduce warpage.

7.3 Antenna Design

Fig. 7.3a presents a 2x2 sub-array with the antenna feeds located at one side of the microstrip antennas. The direction of the magnetic dipoles around the antenna is also shown for the TM_{01} mode excitation. \mathbf{M}_c is the magnetic dipole along the radiation edge and generates the co-pol pattern. $\mathbf{M}_1\text{-}\mathbf{M}_4$ are the magnetic dipoles along the non-radiation edges and result in the cross-polarization pattern. Fig. 7.3c presents the simulated electric-field distribution along the antenna's non-radiating edge, and an imbalance in both amplitude and phase is observed for \mathbf{M}_1 (\mathbf{M}_3) and \mathbf{M}_2 (\mathbf{M}_4), and is due to the finite coaxial feed at the edge of the antenna. Note that $\mathbf{M}_1\&\mathbf{M}_3$ and $\mathbf{M}_2\&\mathbf{M}_4$ have the same amplitude and are 180° phase difference due to the

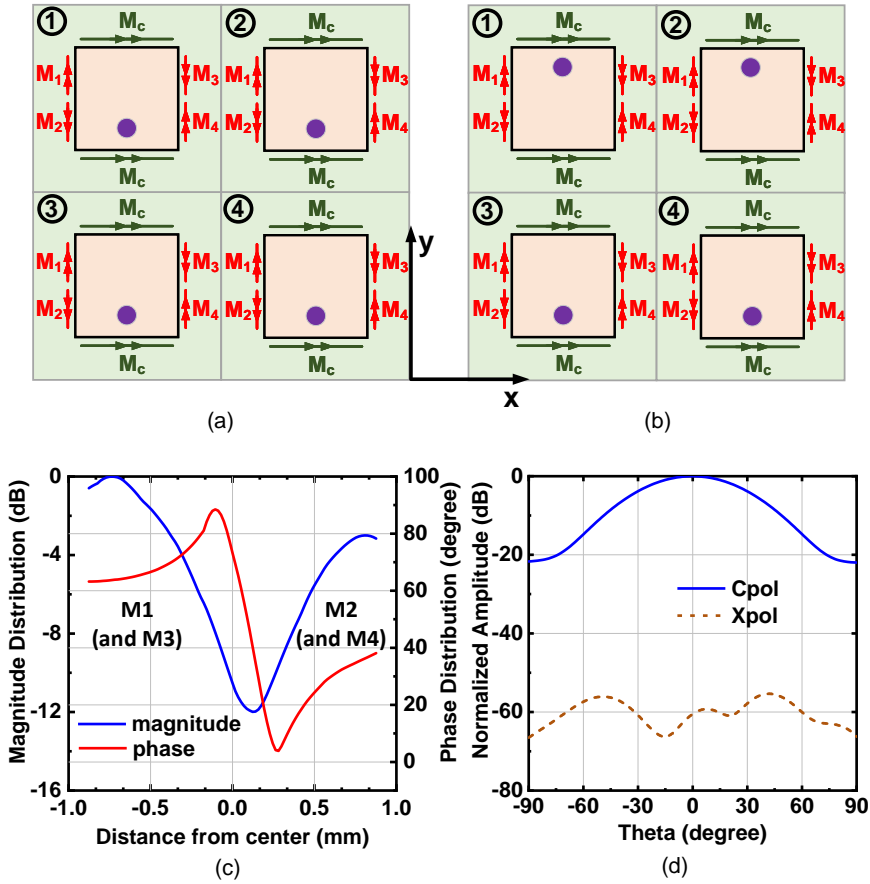


Figure 7.3: Single polarized 2x2 subarray with (a) standard feeds and (b) rotated feeds. (c) Simulated electric field distribution along the non-radiation edge of a single antenna. (d) Simulated 2x2 antenna array pattern with feed rotation. M_1 , M_3 and M_2 , M_4 are 180° out of phase.

symmetry of the antenna feed in the y-direction. This current distribution results in a radiated cross-polarization component which cancels at broadside and when scanning in the E-plane (y-direction). However, when the array scans in the x-direction (H-plane), the magnetic dipole pair M_1 & M_2 and M_3 & M_4 do not cancel and this results in a high cross-polarization level.

A common method to solve the cross-polarization problem in the H-plane is to use feed rotation [16], and this is achieved by flipping the antenna feeds between two adjacent rows as Fig. 7.3b. In this case, every 2x2 antenna cell maintains a symmetric field in the x and y directions. The magnetic dipoles M_2 and M_4 from element-1 cancel the M_1 and M_3 dipoles from element-3 and so forth. As a result, a phased-array based on a 2x2 cell with feed rotation radiates a very

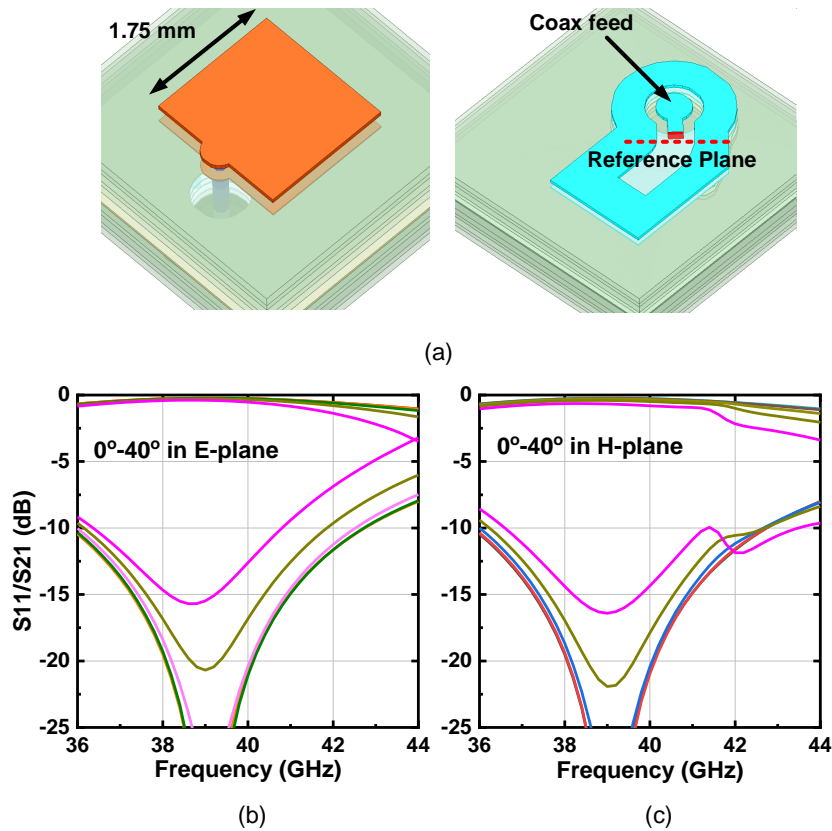


Figure 7.4: (a) 39 GHz antenna model and coaxial feed. Simulated S_{11} and S_{21} versus scan angle for (b) E-plane and (c) H-plane.

low cross-pol level when scanning in the E and H-planes. This is shown in Fig. 7.3d with < -55 dB cross-polarization level in the H-plane. Also, feed-rotation results in more space for the 2x2 beamformer chip as shown in Fig. 7.1c.

The wideband antenna model for the 39 GHz phased-array is presented in Fig. 7.4a. The antennas employ a grid size of 3.76 mm (0.52λ @ 41 GHz) in both the x and y-axes. A coaxial via from M1 to M12 layer is used to feed the antenna, with a characteristic impedance of 50 Ω . The distance from the beamformer chip's RF port to reference plane is 2.7 mm resulting in 0.35 dB loss (t-line loss is 1.3 dB/cm at 40 GHz). This improves the system EIRP and noise figure as compared to 16-channel RFICs with 1-1.5 dB distribution loss between the chip and the antennas [4, 5, 15, 29, 40].

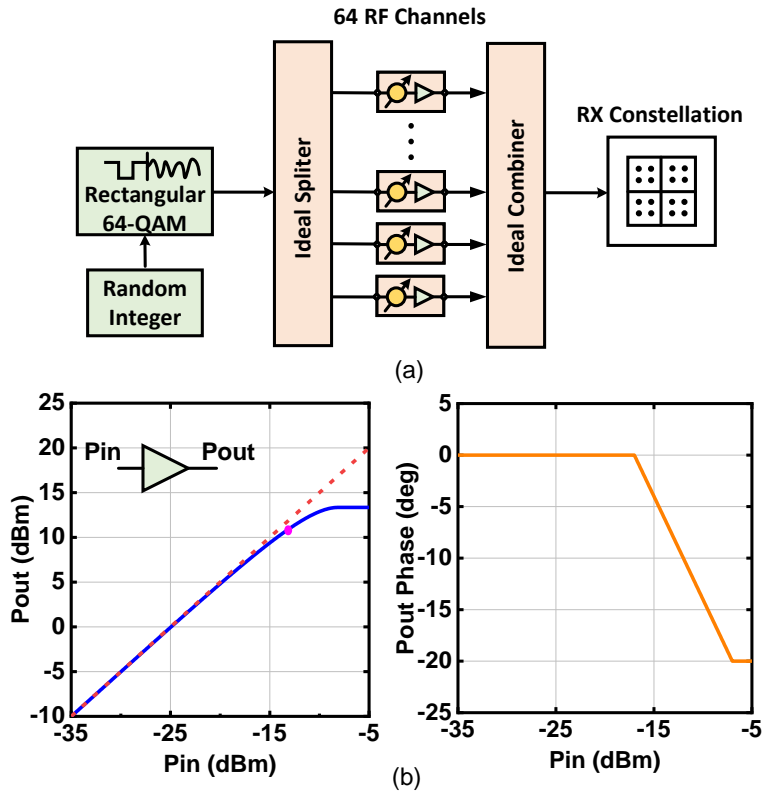


Figure 7.5: (a) Setup for EVM analysis in Matlab and (b) transmit RF channel model with 11 dBm OP1dB and its AM-AM and AM-PM response.

The antenna model is simulated in ANSYS HFSS using master and slave boundary conditions and Floquet port excitation. Fig. 7.4b, c presents the simulated S_{11} when scanning in both the E and H-planes. In the H-plane, the antenna can scan up to 60° with $S_{11} < -7$ dB at 37-42 GHz. In the E-plane, the antenna scans up to 40° with $S_{11} < -7$ dB at 37-41 GHz. The simulated S_{21} shows an antenna loss of < 0.8 dB at 39-40 GHz at 0 to 40° scan angles (see reference plane in Fig. 7.4a). The S_{21} response includes both the antenna ohmic loss and the reflection loss.

7.4 EVM Analysis versus Gain and Phase Error

Fig. 7.5a presents a system simulation setup in Matlab to investigate the effect of the phased-array channel variations on the radiated EVM of a complex waveform. A random integer

generator together with a rectangular QAM baseband modulator are used to generate the 64-QAM waveform with $\alpha=0.35$ and a peak-to-average-power ratio (PAPR) of 7.7 dB. This waveform is then distributed to 64 channels each with a different amplitude and phase response. The combining in the air is modelled using an ideal 64:1 summer and the signal is demodulated using a Matlab constellation diagram block. If the phased-array is scanning to θ_s and a progressive phase shifter, α_s , is used in the channels ($\alpha_s=kdsin(\theta_s)$), then a TTD phase shifter is used in each arm of 64:1 combining network to simulate the time-delay propagation in air for the 64 antennas.

The channels are modelled using a linear gain part with amplitude and phase control, and a non-linear power amplifier with $OP1dB = 11$ dBm and an AM-to-AM and AM-to-PM response as shown in Fig. 7.5b. The AM-AM and AM-PM responses were chosen since they result in a simulated EVM which is close to the measured values at different backoffs. The *MemorylessNonlinearity* function in Matlab communications toolbox was used to model the power amplifier using a cubic polynomial function.

Fig. 7.6 presents the simulated 64-element phased-array EVM at different backoffs and versus RMS gain and phase error levels. For 14 dB backoff (highly linear operation), the EVM remains at 0.8% and is independent of the RMS gain and phase errors. This is because the different gain and phase values across the elements average to zero and do not affect any constellation point. At 8 dB backoff, the EVM for an ideal array (RMS gain and phase error = 0) is 1.3%, and increases to 1.8% for an RMS gain error of 2 dB. The EVM increase with the RMS gain error is the result of +/-4 dB peak-to-peak gain variation across the array, leading to different compression characteristics for the power amplifiers. Note that the EVM increases from 1.3% to only 1.4% for an RMS gain error of 1 dB (+/-2 dB peak-to-peak gain variation). Finally, at a backoff of 5 dB, the EVM starts at 4.05% for no gain and phase error (given solely by the amplifier compression characteristics) and increases to 4.1%-4.2% for an RMS gain error of 1-2 dB (+/-2 dB and +/-4 dB variation).

Note that the EVM is independent of the RMS phase error on the array, and the increase

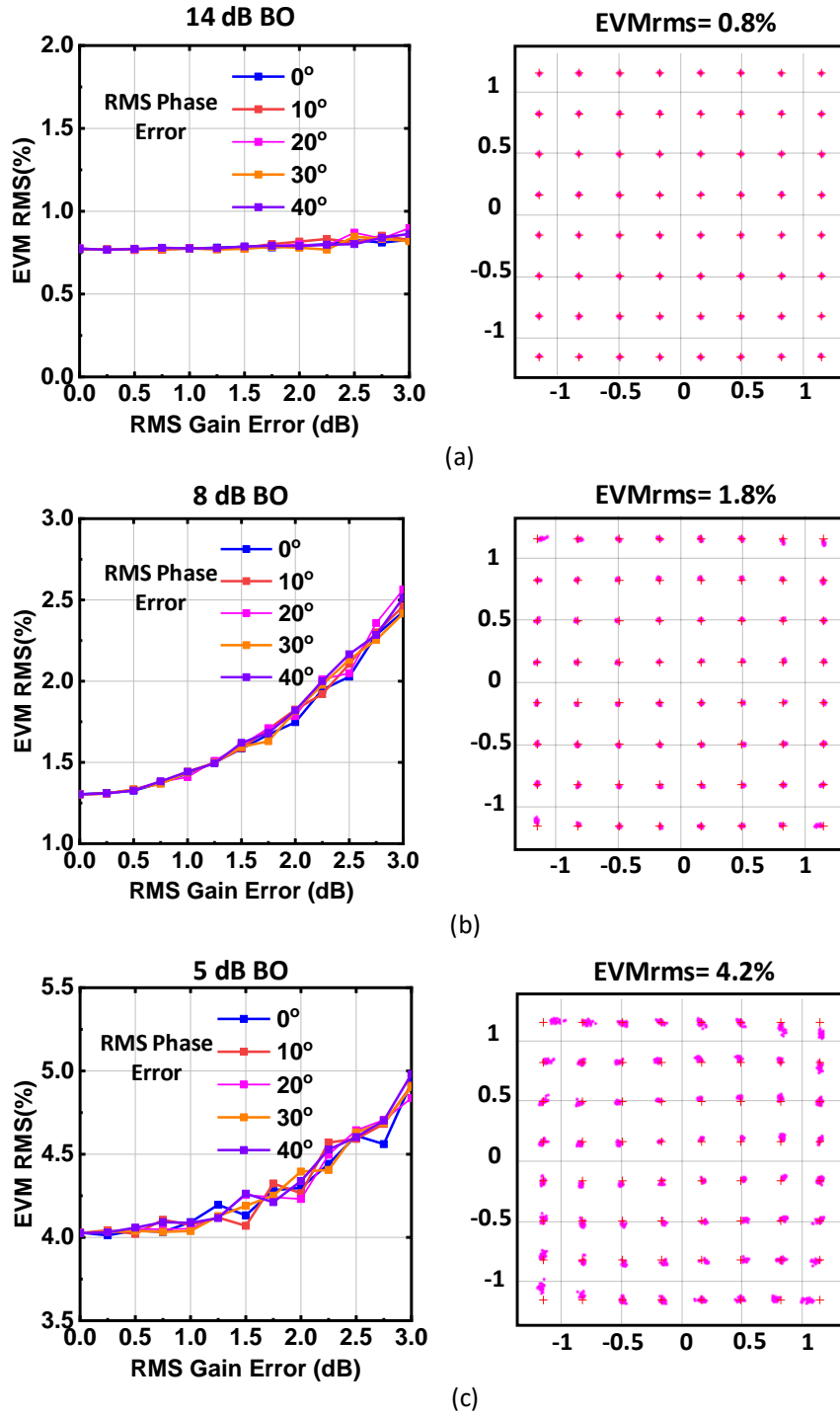


Figure 7.6: Simulated EVM versus rms gain and phase error across the array for a 64-QAM signal with $\alpha=0.35$ and a PAPR=7.7 dB, and at (a) 14 dB backoff, (b) 8 dB backoff and (c) 5 dB backoff. Constellations are plotted for 2 dB rms gain error and 20° rms phase error.

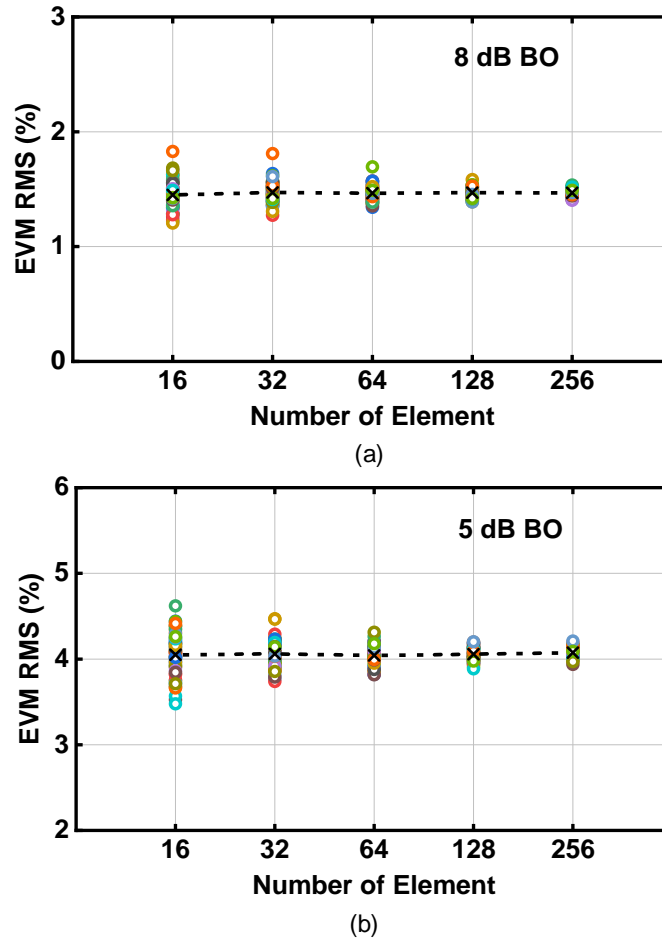


Figure 7.7: Simulated EVM versus number of element with 1 dB rms gain error and 10° rms phase error at (a) 8 dB and (b) 5 dB backoff for 60 iterations.

is solely due to the RMS gain error, which is basically the variations in the amplifier non-linear compression characteristics for different channels. The reason is that different RMS gain errors cause different amplitude and phase distortion from the power amplifiers for a modulated signal.

One surprising conclusion from this analysis is that the RMS phase error on the array does not affect the I / Q modulation properties (and EVM) even if it is very high (20° to 40° RMS error). This is because the 64-channel are added together in the far-field, and phase errors for all the channels average out to nearly zero. And even if there is a residual phase error after adding the 64 channels, it is a static (constant) phase error and is equally presented for every

constellation point. Therefore, it is ignored in the demodulator and does not affect the EVM. Note that a high RMS phase error does affect the array sidelobe levels and reduces the array directivity, thus reducing the SNR in the far-field. But as long as the system is not SNR limited, it does not affect the EVM.

Fig. 7.7 presents the simulated EVM versus number of antenna elements in a phased-array with 1 dB RMS gain error and 10° RMS phase error, at 8 dB and 5 dB backoff. 60 iterations are performed due to the statistical nature of the RMS error. It is seen that the mean EVM is nearly independent of the element count for $N \geq 16$. Also, for arrays having 64 elements and above, the EVM is tightly distributed around the mean value. Similar results are obtained for an RMS phase error of 20° . This simulation shows that the results in Fig. 7.6 apply for a wide size of phased-arrays.

The analysis shows that large phased-arrays (such as 32, 64, or 256 elements) can be operated up to an RMS gain error of 1 dB, with a minor penalty in pattern sidelobes and virtually no penalty in the radiated EVM. This finding will reduce the calibration overhead even for stringent EVM requirements and will reduce the cost of 5G phased-arrays.

7.5 Transceiver and High-Pass Filter

The up-conversion from IF (5 GHz) to RF (39 GHz) is achieved using the UCSD 22-44 GHz wideband up/down conversion transceiver chip, and is also fabricated using SiGe BiCMOS technology (Fig. 7.8a). The up-converter TX path contains a variable IF amplifier, a double-balanced mixer, and an RF power amplifier. A wideband T/R switch is also integrated on the chip for half-duplex operation. To suppress the lower-sideband (image) response from the mixer, on-chip low-Q elliptic filters are integrated between the mixer and the PA [43]. An integrated doubler is used in the LO path so as to reduce the external local oscillator frequencies (an LO of 17 GHz is required for 39 GHz operation).

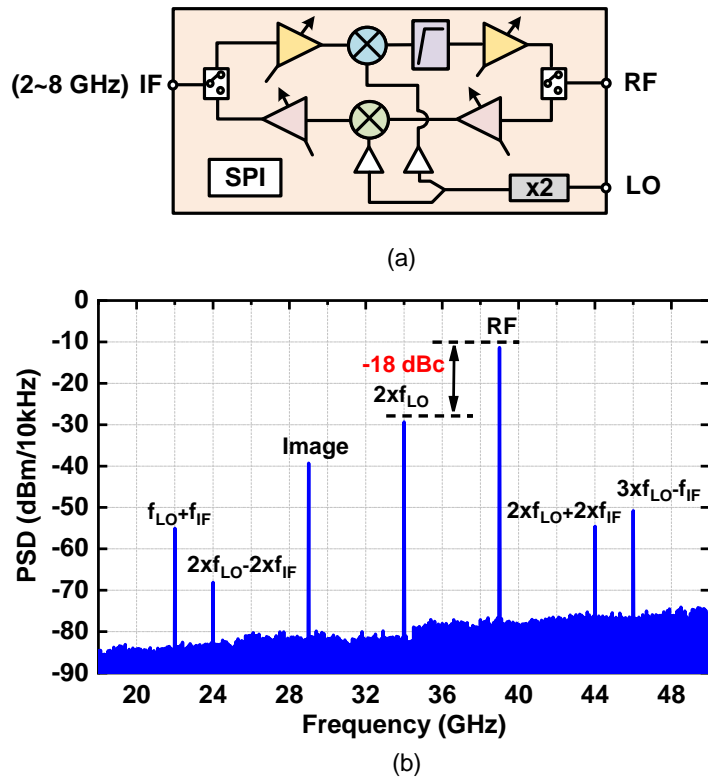


Figure 7.8: (a) Block diagram of UCSD wideband transceiver and (b) measured broadband spectrum at 10 dB backoff from P1dB in the TX mode.

The up-converter path results in a measured gain of 17 dB and an output P1dB of 12 dBm at 39 GHz. Fig. 7.8b presents the measured up/down-converter spectrum operating at 10 dB backoff in the transmit mode. The LO leakage is -18 dBc and the image is -28 dBc compared to the RF signal. Note that the LO leakage absolute level does not reduce versus backoff and therefore, it is important to measure it at the operating point and not at P1dB (LO leakage is -28 dBc at P1dB). The other mixing spurs are also shown and are <-40 dBc at 10 dB backoff operation.

Due to the limited suppression of LO leakage and image rejection from the transceiver, an additional high-pass filter is used after the transceiver (Fig. 7.9a). The filter is based on a multi-stub multi-mode resonator, which can be analyzed using even- and odd-mode techniques [44],

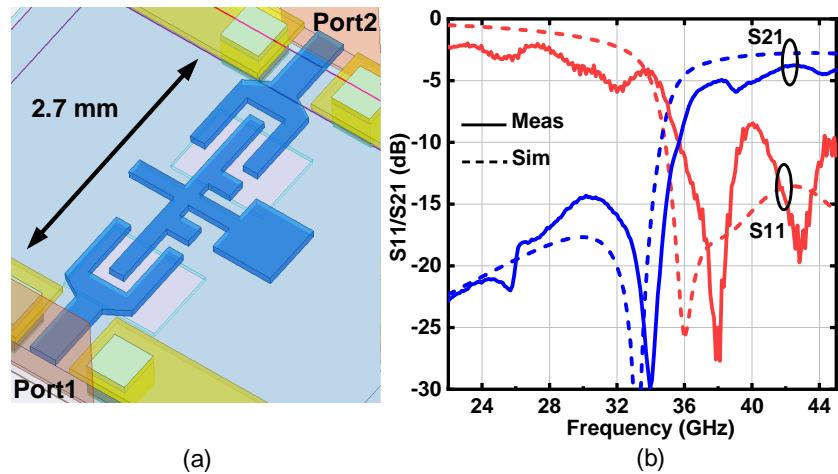


Figure 7.9: (a) Simulation model for the 39 GHz high-pass filter, (b) measured and simulated filter S-parameters.

and exhibits high rejection in the LO band (32-35 GHz) and low insertion loss in the RF band (37-42 GHz). Note that 42 GHz operation is obtained using a 35 GHz LO and 7 GHz IF. The filter operation is explained as follows: coupling between the input and output feedlines is controlled by the interdigital capacitor and the defected ground structure (DGS). The center step-impedance stub generates a transmission zero at the lower side of the passband, and is designed to be at the LO frequency. Fig. 7.9b presents the measured and simulated filter S-parameters. The transmission zero is located at 34 GHz, and $S_{21} < -20$ dB at 33-35 GHz for LO rejection. The image at 27-29 GHz is also reduced by 12-15 dB. In the passband, the filter insertion loss is 1-1.5 dB higher than simulations (and S_{11} has larger ripples) and this is due to difficulties in deembedding the coaxial connectors at 40 GHz.

7.6 39 GHz Phased-Array RF Performance Measurements

7.6.1 Construction, Array Electronic Gain and Calibration

The fabricated 8x8 39 GHz phased-array is shown in Fig. 7.10 with an active area of 3×3 cm². The array consumes 9.6 W in the Rx mode and 16-18 W in the Tx mode at P1dB and Psat.

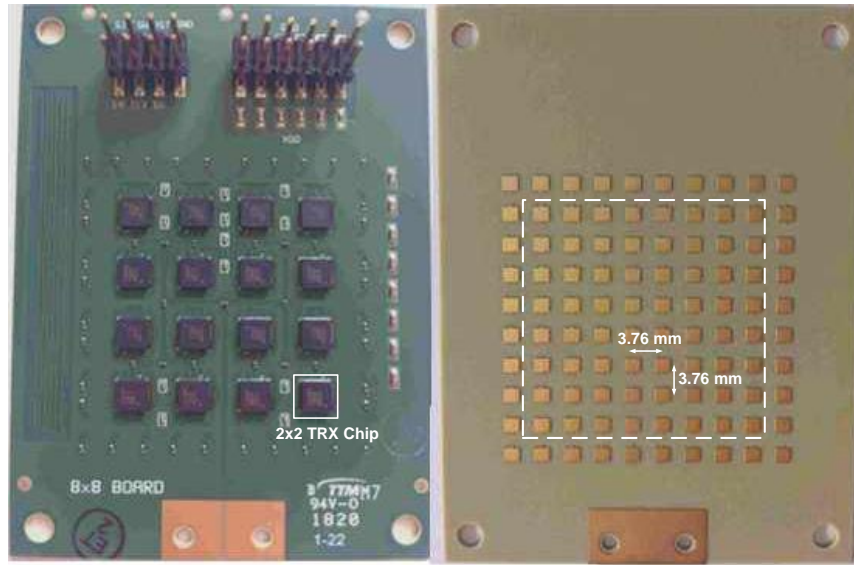


Figure 7.10: Front and back view of the 39 GHz 8x8 phased-array.

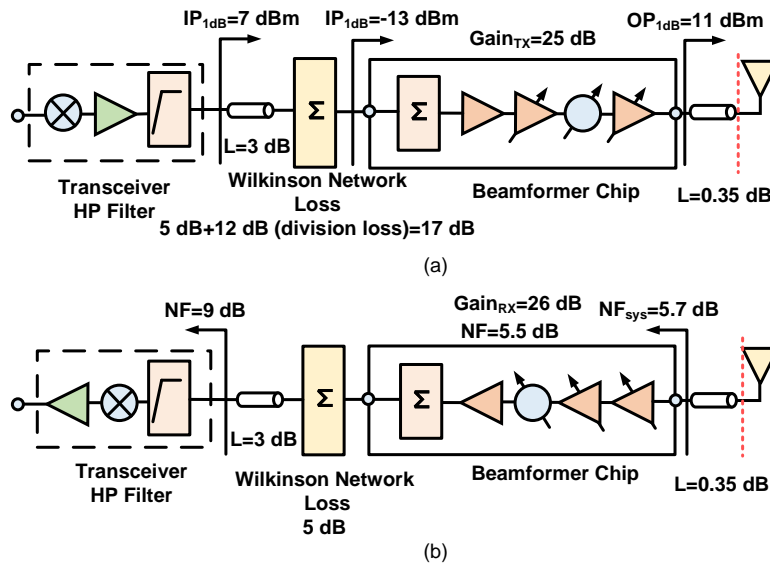


Figure 7.11: Block diagram for system analysis in (a) TX mode, and (b) RX mode.

A fan is used behind the array for cooling and keeps the PCB at a temperature $< 55^{\circ}\text{C}$.

In the Tx mode, the input $P_{1\text{dB}}$ at the common-port (coaxial connector) is calculated as (Fig. 7.11a):

$$P_{\text{common-port}_{1\text{dB}}} = -13 + 12 + 5 + 3 = 7 \text{ dBm} \quad (7.1)$$

where -13 dBm is the input IP1dB for the beamformer chip, 12 dB is the Wilkinson division loss, 5 dB is the Wilkinson ohmic loss, 3 dB is the extra transmission-line loss between the array and the connector (2.2 dB), and connector loss at 39 GHz (0.8 dB). The 7 dBm power at the common RF port is achieved using the UCSD transceiver.

The TX gain is defined as the power available at the antenna port for each element divided by the power input at the common port (Fig. 7.11a):

$$\begin{aligned} Gain_{TX_electronic} &= \frac{P_{element}}{P_{in}} = -3 - 12 - 5 \\ &+ 25 - 0.35 = 4.65 \text{ dB} \end{aligned} \quad (7.2)$$

where the beamformer electronic gain is 25 dB and the transmission-line loss between the chip and the antenna is 0.35 dB. The other factors are explained above.

The RX electronic gain is defined as the ratio of the output power at the RF connector (P_{out}) to the total power collected at the antenna aperture (referred to the microstrip antenna port), and is (Fig. 7.11b):

$$\begin{aligned} Gain_{RX_electronic} &= \frac{P_{out}}{S_{inc} * Area * \epsilon_{ant}} \\ &= -0.35 + 26 - 5 - 3 = 17.65 \text{ dB} \end{aligned} \quad (7.3)$$

where S_{inc} is the incident plane-wave power, $Area$ is the phased-array antenna area ($3 \times 3 \text{ cm}^2$) and ϵ_{ant} is the antenna efficiency. This gain includes the antenna-to-chip loss (0.35 dB), beamformer chip electronic gain (26 dB), Wilkinson network ohmic loss (5 dB) and the extra transmission-line loss (3 dB). Assuming a filter and transceiver NF of 9 dB at the common-port, the entire system NF, referred to the chip input port, is 5.7 dB and includes the beamformer chip and the Wilkinson network loss. This is only 0.2 dB higher than the beamformer NF due to the high electronic gain of the phased-array. Note that if we use the antenna port as the reference plane (since the available RX power may be defined at the antenna port), the system NF becomes 6.05 dB and

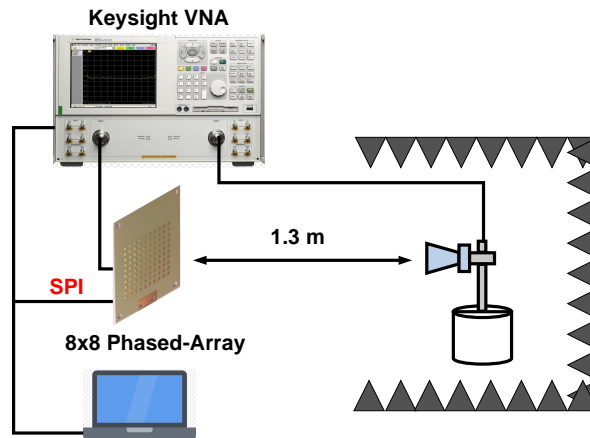


Figure 7.12: Measurement setup for pattern and calibration.

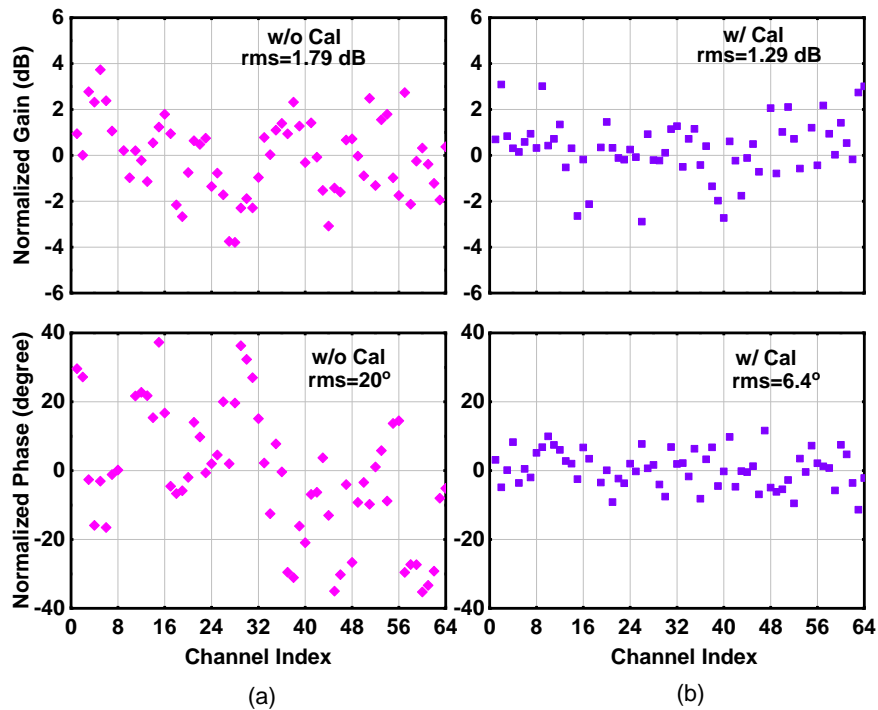


Figure 7.13: Measured normalized gain and phase variation (a) without calibration and (b) with calibration at 39 GHz in the TX mode for 64 channels.

includes the 0.35 dB transmission-line loss between the antenna and the beamformer chip.

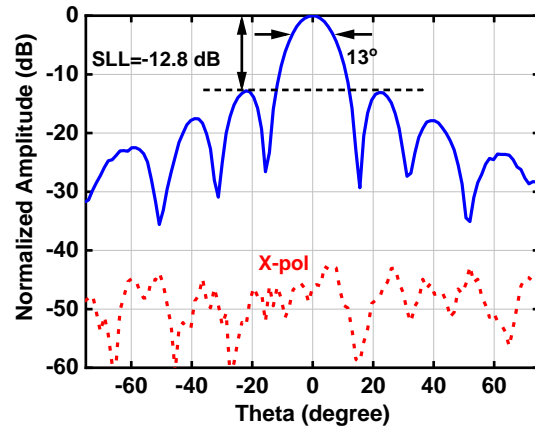
The 8x8 phased-array is measured in the far-field in an anechoic chamber with a standard gain horn antenna and a Keysight Vector Network Analyzer (Fig. 7.12). Each channel is turned

on individually at the nominal gain and phase state and S_{21} is measured. Due to the Tx/Rx switch loss (~ 1.7 dB) and transformer loss (~ 0.8 dB) after the PA, the neighboring antenna elements are still connected to loads having $S_{11} < -8$ dB when the power amplifiers are turned off. Fig. 7.13a and b present the gain and phase variation across the 64 channels at 39 GHz in the TX mode. Although the phased-array has a symmetric layout and equal feed-line lengths from the beamformer chips to the antennas, there is ± 4 dB amplitude variation and $\pm 40^\circ$ phase variation across all channels. This is due to the variations between the 16 different beamformer chips, assembly, and the non-ideal behavior of the 0201 lumped-element 100Ω resistors at 39 GHz in the PCB Wilkinson network. The array is then calibrated, and the offset between the reference channel and all other channels is compensated using the phase shifter and VGA on each channel. Note that with calibration, most of the channels have been placed within a $\pm 10^\circ$ and ± 2.5 dB range, resulting in an RMS gain and phase error across the array of 1.29 dB and 6.4° , respectively. This RMS error has minimal effect on the patterns as previously shown in [6].

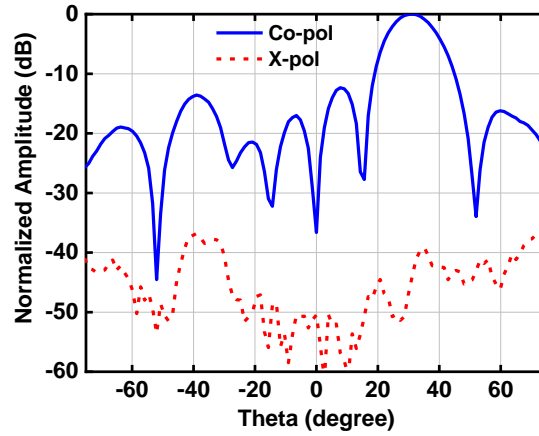
7.6.2 Patterns, EIRP and Frequency Response Measurements

Patterns: Fig. 7.14 presents the measured broadside pattern with -12.8 dB sidelobe level and a 3-dB beamwidth of 13° . The cross-polarization level is < -40 dB at broadside. A cross-polarization level of < -30 dB is achieved over all scan angles in the H-Plane and agrees well with the analysis in Section 7.3 (Fig. 7.14b, c). The cross-polarization level is also < -30 dB in the E-plane and is not shown.

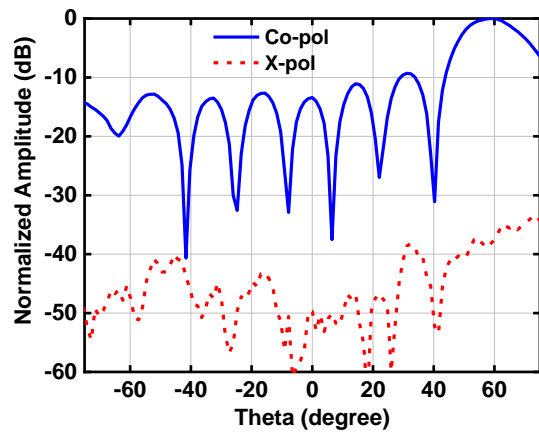
Fig. 7.15 presents a comparison of the Tx-mode H-plane patterns (azimuth scan) measured with and without calibration (RX-mode has similar patterns and is not shown). The phased-array can scan to $\pm 60^\circ$ with < -12 dB sidelobes for uniform illumination, and the patterns with calibration result in 1-2 dB lower sidelobe levels than these without calibration, as expected from previous work [6]. A 6-dB raised-cosine taper results in -15 dB to -16 dB sidelobe levels. The patterns follow a $\cos^{1.2}\theta$ response, and drop by 3.6 dB at 60° as compared to broadside. This



(a)



(b)



(c)

Figure 7.14: Measured broadside co-pol and cross-polarization components at (a) broadside, (b) 30° scan angle in the H-plane and (c) 60° scan angle in the H-plane. All patterns are measured at 39 GHz without calibration.

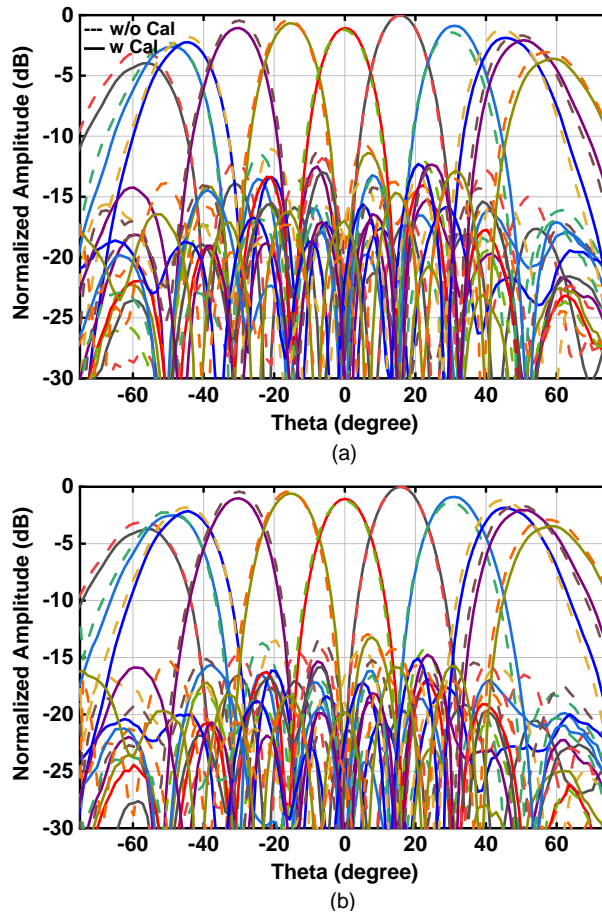


Figure 7.15: Measured H-plane patterns in the TX mode with and without calibration for (a) uniform illumination, and (b) 6-dB raised cosine taper.

shows that the antenna is well matched up to wide scan angles. For lower sidelobes with more aggressive aperture distributions such as -30 dB Taylor, one should definitely calibrate the array to an RMS gain error of $<0.5-0.7$ dB.

Fig. 7.16 presents the measured E-plane patterns. The array scans to $\pm 50^\circ$ at 39 GHz with sidelobe levels of -13 dB to -14 dB.

Fig. 7.17 presents the measured H-plane patterns at 38-40 GHz when the phase shifters across the array are set to scan the beam to 50° at 39 GHz. The measured beam-squint is 2.2° at 38-40 GHz which is close to the simulated value of 1.8° . Since the beamwidth is 18° at this scan angle, the beam-squint has negligible effect on the phased-array performance.

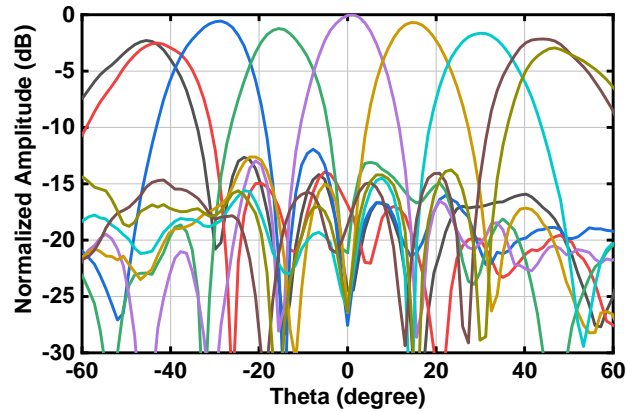


Figure 7.16: Measured E-plane patterns without calibration at 39 GHz.

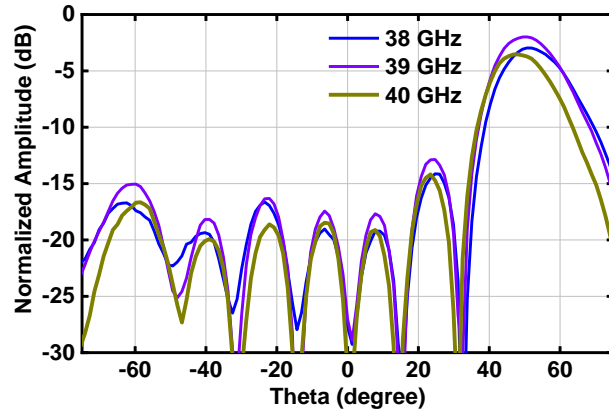


Figure 7.17: Measured beam-squint from 38 to 40 GHz at 50° scan angle in the H-plane and normalized to the broadside pattern at 39 GHz. Patterns are measured without calibration.

EIRP: The measured EIRP at broadside of the 8x8 array with and without calibration is shown in Fig. 7.18a. An $EIRP_{sat}$ of 51 dBm is achieved with a 3-dB bandwidth of 36-41.5 GHz. The EIRP can be calculated as:

$$EIRP_{sat} = 20\log N + 4 + 12 = 36 + 4 + 12 = 52 \text{ dBm} \quad (7.4)$$

where $P_{el_sat} = 12$ dBm, and agrees well with measurements of 50-51 dBm at 39-40 GHz. A microstrip antenna gain of 4 dB is used and includes both the antenna loss and the transmission-line loss from the beamformer chip (0.3 dB + 0.35 dB = 0.65 dB). The measured $EIRP_{1dB}$ is

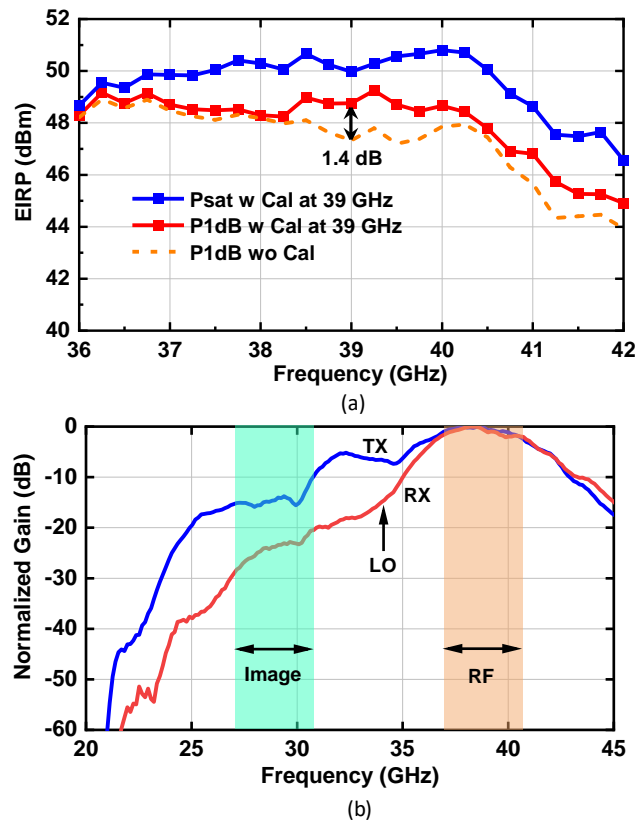


Figure 7.18: (a) Measured EIRP at P1dB and Psat versus frequency with and without calibration and (b) wideband frequency response in TX and RX modes of the 39 GHz 8x8 array.

49 dBm with calibration, which is 1.4 dB higher than the non-calibrated array. This is due to all elements being driven together to P1dB after calibration. Also, the calibration improves the antenna directivity by ~ 0.5 dB due to reduced RMS errors and results in more uniform amplitude and phase distribution on the array.

Frequency Response: The measured array wideband frequency response is shown in Fig. 7.18b. The RF band is 37-42 GHz, and for 39 GHz operation, the LO is chosen at 34 GHz which results in an IF of 5 GHz and a 29 GHz image band. There is only 5 dB LO suppression and 15 dB image rejection in the TX mode which is not enough to satisfy the FCC emission requirements. This is due to the wideband performance of both the beamformer chip and the antenna. Therefore, the up-converter and filter response is essential for low spurious radiation.

7.7 System Level Measurements

Complex modulation measurements are performed on the 39 GHz phased-array system with the setup shown in Fig. 7.19a. A Kesight M8195 arbitrary waveform generator (AWG) is used to generate 16-QAM and 64-QAM waveforms with an IF centered at 5 GHz. The modulated IF signal is upconverted to 39 GHz using the transceiver chip and the high-pass filter (LO is set at 17 GHz) described in Section 4.5. On the receive side, a Ka-band horn antenna is used at a range of 1 m, and results in a space-loss-factor ($SLF=(\lambda/4\pi R)^2$) of 64.3 dB at 39 GHz. A Keysight DSOZ632A 63 GHz real-time scope is then employed to demodulate the signal using the Keysight Vector Signal Analysis software (VSA-89600). The scope has excellent sensitivity even at -40 dBm and a pre-amplifier is not required. Also, a spectrum analyzer is used on the RX port to measure the LO and image leakage.

7.7.1 Radiated LO and Image Power

A single-tone test is first performed to measure the LO and image rejection with $f_{RF}=39$ GHz, $f_{LO}=34$ GHz, and $f_{Image}=29$ GHz (Fig. 7.19b). An LO rejection of 50 dBc and an image rejection of 49.5 dBc are achieved at the array $EIRP_{1dB}$ level.

To calculate the total LO radiated power, one starts with understanding the measured RF signal power levels. The received power at the horn is found using the Friis equation as:

$$P_r = P_t G_t G_r \left(\frac{\lambda}{4\pi R}\right)^2 \quad (7.5)$$

where $EIRP=P_t G_t$, with P_t being the total power radiated by the antenna and G_t is the antenna gain, both defined at the antenna input port. G_r is the receive horn gain, and R is the distance between the phased-array and the horn antenna. This equation can also be written as:

$$P_r = P_{rad} D_t G_r \left(\frac{\lambda}{4\pi R}\right)^2 \quad (7.6)$$

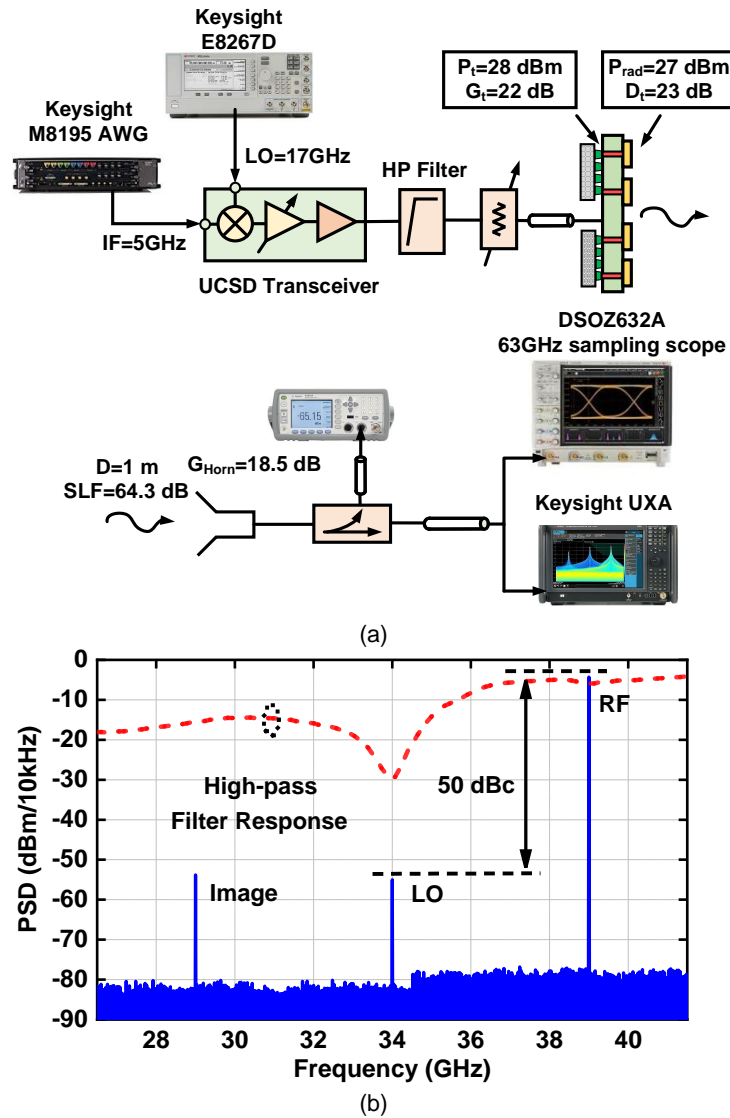


Figure 7.19: (a) Setup for 39 GHz 8x8 array 1 m link and EVM measurements. (b) Measured spectrum for the 39 GHz array system at P1dB.

where P_{rad} is the total radiated power from the array and D_t is the transmit array directivity. Both P_{rad} and D_t are defined in the air, just in front of the antenna (Fig. 7.19a). At 39 GHz, the antenna radiates a total power of $P_{rad} = 10$ dBm (P_{el}) - 1 dB (antenna and t-line loss) + 18 dB (64 elements) = 27 dBm.

The measured receive LO signal is 50 dB lower than the RF signal at P1dB (Fig. 7.19b), and if the LO and RF signals are at the same frequency, then the total radiated LO power is found

using a simple ratio and is $P_{rad}-P_{LO} = 27 \text{ dBm} - 50 \text{ dB} = -23 \text{ dBm}$. However, the LO frequency is at 34 GHz and there is a -1.7 dB difference in the SLF between 34 GHz and 39 GHz ($-1.7 \text{ dB} = (34/39)^2$). Taking this correction factor into account, the total radiated LO power is $-23 \text{ dBm} + 1.7 \text{ dB} = -21.3 \text{ dBm}$, and is 8.3 dB lower than the FCC allowed value of -13 dBm/MHz .

The LO radiation pattern is nearly the same pattern as the RF signal pattern due to the wideband phase shifters used. When the phased-array is set to scan to θ_s at 39 GHz, the LO radiation at 34 GHz peaks at a slightly different angle. This is calculated using the progressive phase, α_s , between the antenna elements, and is given by:

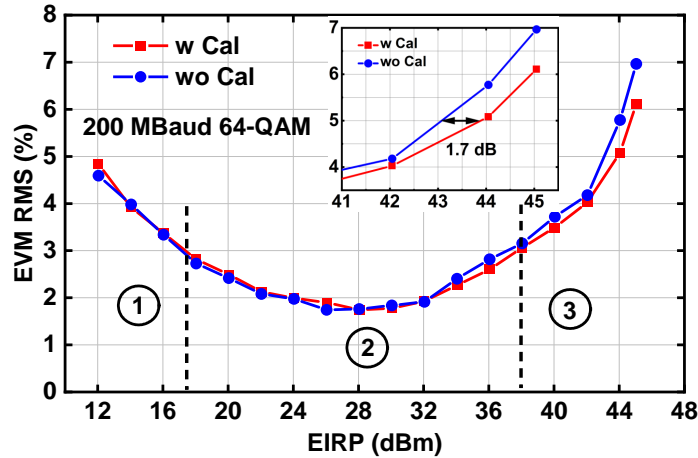
$$\alpha_s = k_{RF}d\sin(\theta_s) = k_{LO}d\sin(\theta_{LO}) \quad (7.7)$$

$$\sin(\theta_{LO}) = (k_{RF}/k_{LO})\sin(\theta_s) \quad (7.8)$$

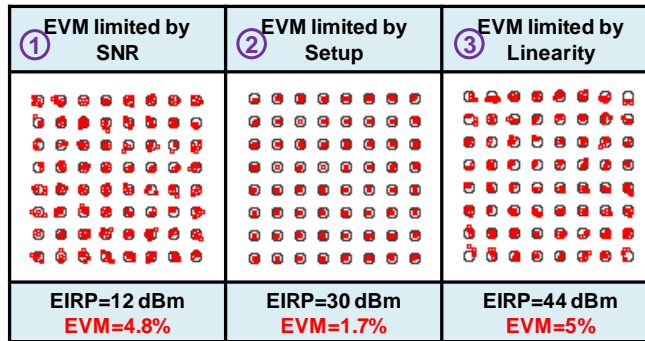
where $k_{RF} = 2\pi/\lambda_{RF}$ and $k_{LO} = 2\pi/\lambda_{LO}$, and d is the antenna spacing. For example, a scan angle of 50° at 39 GHz results in a 34 GHz LO peak radiation angle of 61.5° . Therefore, for OOB (out-of-band) emission specifications, it is important to measure the LO power at a different angle than the RF scan angle.

7.7.2 EVM

A 64-QAM 200 MBaud waveform with a 5 GHz carrier is generated by the AWG with a pulse shaping factor $\alpha=0.35$ and a peak-to-average-ratio (PAPR) of 7.7 dB. Fig. 7.20a presents the EVM_{rms} versus the array EIRP. In region 1, the EVM is limited by the SNR due to the low EIRP and the SLF of 64.3 dB. In region 2, the EVM is limited by the AWG SNR together with the phase noise contribution of the LO signal generator and the real-time scope ($EVM=1.7\%$). And in region 3, the EVM is limited by the power amplifier non-linearity in the phased-array. The measured constellation diagrams for the different EIRP regions are shown in Fig. 7.20b. The 39 GHz phased-array is capable of radiating an average EIRP of 44 dBm for a 64-QAM signal with



(a)



(b)

Figure 7.20: Measured (a) EVM versus EIRP at 39 GHz with a 200 MBaud 64-QAM waveform with and without calibration, and (b) constellations at different EIRP levels.

7.7 dB PAPR and $<5\%$ EVM_{rms} , which is 5 dB backoff from the array P1dB.

A closer look at the EVM with and without calibration (Fig. 7.20a) shows that the EVM with calibration results in 1.7 dB higher EIRP. This is because the calibrated array results in 1.4 dB higher EIRP than a non-calibrated array and the EVM is dependent on backoff from P1dB. Also there is an RMS gain reduction from 1.76 dB to 1.26 dB between the calibrated and non-calibrated array, which improves the EVM as shown in Fig. 7.6.

The EVM is also measured for different scan angles for the 64-QAM 200 Mbaud waveform (Fig. 7.21). An almost-constant EVM is achieved within a $\pm 60^\circ$ scan range at 5 dB (44-45 dBm) and 10 dB (39-40 dBm) backoff from P1dB. All EVM values include the transceiver and LO

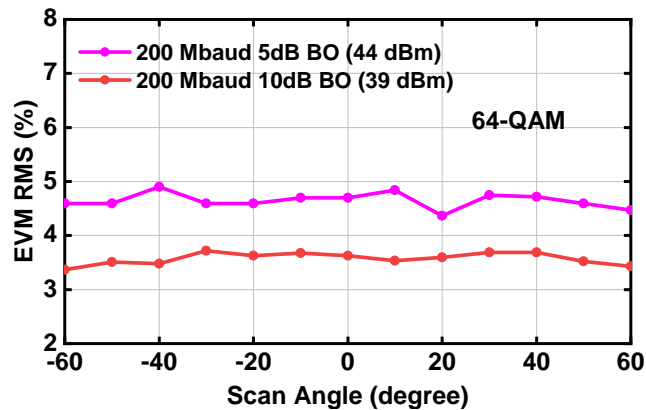
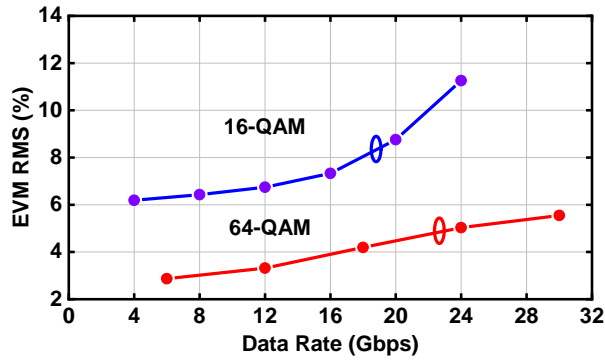


Figure 7.21: Measured EVM versus scan angles in the H-plane for a 64-QAM waveform. Measurements done without calibration.

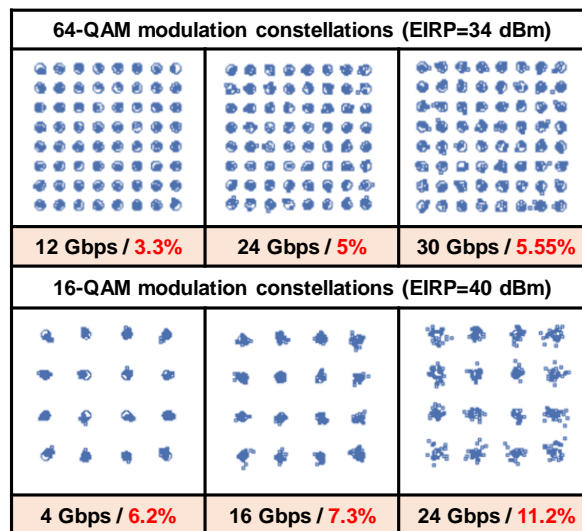
distributions.

7.7.3 Wideband Performance

Fig. 7.22a presents the measured EVM versus data rate with 16 and 64-QAM waveforms at a carrier frequency of 39 GHz. A maximum data rate of 24 Gbps and 30 Gbps with 16-QAM and 64-QAM waveforms is achieved with low EVM. Note that for 30 Gbps 64-QAM waveform, the instantaneous bandwidth required is 5 GHz, and this is within the 3-dB bandwidth of the array (37-42 GHz). The reason why the 16-QAM measurements have a worse EVM than the 64-QAM measurements is that the 16-QAM results were done at an EIRP of 40 dBm, which is 6 dB higher EIRP than the 64-QAM results (see Fig. 7.22b). Example constellations for different data rates are shown in Fig. 7.22b. Table 7.2 presents a comparison with state of the art phased-arrays in the 39 GHz band. It is seen that this work has the highest beamformer linearity, wide scanning range and highest data rate to-date.



(a)



(b)

Figure 7.22: Measured (a) EVM versus data rate with 16 and 64-QAM waveforms, (b) constellations at different data rates. Measurements done without calibration.

7.8 Conclusion

A 39 GHz 8x8 phased-array for 5G applications was presented. The array achieves an EIRP of 49-51 dBm with 3-dB bandwidth of 36-41.5 GHz. The array can scan up to +/-60° in the azimuth plane and +/-50° in the elevation plane. A complete 39 GHz system is demonstrated using an 8x8 array with a high-pass filter and a compact transceiver. The system has excellent LO and image rejection and < 5% EVM is achieved using a 64-QAM 200 MHz waveform with an average

Table 7.2: Comparisons with State-of-the-Art 39-GHz Phased-Arrays

Chip Parameter	This work	Tokyo Tech '19 [37]	Intel '19 [26]
Technology	0.18 μm SiGe BiCMOS	65 nm CMOS	28 nm CMOS
Elements per chip	4	4	8 (dual-polarized)
Phase control (bit)	6	>6	4
Gain control (dB)	25	N/A	27
RX NF / chip (dB)	5.5	>7	5.8 (chip only)
RX IP _{1dB} (dBm)	-28	N/A (estimated <-39 dBm)	-43
TX OP _{1dB} / ch. (dBm)	11	15	11.5
TX P _{DC} / ch. (mW)	250 @ P_{1dB}	375 @ P _{1dB}	339 @ P _{1dB}
RX P _{DC} / ch. (mW)	150	N/A	N/A
Phased-Array Measurements			
Elements in array	8x8	4x16	4x4
Polarization	Single	Single	Single
EIRP (dBm)	51 @ P_{sat}	53 @ P _{sat}	No EIRP
TX P _{DC} / array (W)	16 @ P_{1dB} 18 @ P_{sat}	24 @ P _{sat}	5.4 @ P _{1dB} / Pol (N/A @ P _{sat})
Scan range (°)	+/- 60°	+/- 20°	+/- 45°
EVM	-26 dB @ 200 MHz 5 dB BO from P1dB (EIRP=44 dBm)	-30 dB @ 400 MHz (no EIRP value mentioned)	No Modulation Measurements
Over-the-air maximum data rate	30 Gbps / 64-QAM 24 Gbps / 16-QAM	N/A	N/A

EIRP up to 44 dBm with calibration. Performance comparison with and without calibration is presented and negligible difference is observed in patterns and shows that phased-arrays based on 2x2 beamformer chips and a symmetrical layout can operate well. The EIRP and EVM of calibrated arrays are better than non-calibrated arrays and improvement of 1.4-1.7 dB is observed. The 39 GHz array achieves up to 30 Gbps data-rate with 64-QAM waveforms and is an excellent candidate for 5G 39 GHz mm-wave systems.

7.9 Acknowledgment

The authors thank Renesas Electronics, for sponsoring the beamformer chips used in this work. The array was assembled by Kyocera International, San Diego, using their advanced

assembly production line.

Chapter 7, in full, is a reprint of the material as it appears in: Y. Yin, S. Zehir, T. Kanar, Q. Ma, H. Chung, L. Gao and G. M. Rebeiz, "A 37-42-GHz 8×8 phased-array with 48-51-dBm EIRP, 64-QAM 30-Gb/s data rates, and EVM analysis versus channel RMS errors", *IEEE Trans. Microw. Theory Techn.*, accepted. The dissertation author was the primary investigator and author of this paper.

Chapter 8

Conclusion and Future Work

8.1 Conclusion

This dissertation presented several demonstrations of phased-array systems at 28 and 39 GHz. The arrays are based on 2x2 TRX beamformer chips with all-RF architecture and excellent performance is achieved. Also, some advanced techniques and applications such as carrier aggregation or wideband data transfer between connectorless connectors were presented.

In chapter 2, a 23.5-29.5 GHz wideband 8x8 phased-array for multi-standard operation and 5G carrier aggregation was presented. The array achieves a peak EIRP of 54.8 dBm. The array results in excellent patterns in the E- and H-planes over the frequency range using a single-point calibration at 27 GHz. EVM measurements (-26 dB) at 24.5-29.5 GHz with 200-800 Mbaud 64-QAM waveforms resulted in 46-47 dBm EIRP which is 6-8 dB backoff from $EIRP_{1dB}$. Inter-band 5G carrier aggregation measurements were also demonstrated with 25- and 29-GHz carriers with 12 dB backoff and a total radiated EIRP of 41 dBm. The IM3 components are out of band and partly filtered out by the antenna response. The work shows that carrier aggregation is possible in 5G millimeter-wave system provided that the beamformer phase setting is done so as to minimize the beam squint and pattern gain loss for two carriers.

In chapter 3, the all-RF architecture, both at the chip level and at the PCB level, was shown to result in excellent performance for mm-wave 256-element phased-arrays. State-of-the-art patterns, EIRP and EVM have been demonstrated using this architecture.

In chapter 4, a 1 Gbps communication link at a distance of 3.5-4.75 km using a low-cost 8x8 5G phased-array with SiGe chips was demonstrated. The 5G phased-array can not only support 300-800 meter links but also has potential for supporting extra long distance links for backhaul and point-to-point communications.

In chapter 5, the first short-range connectorless connector link using 5G frequencies and with scanning capabilities was presented. It is seen that the use of phased-array scanning, even in a small array, greatly increases the link robustness versus misalignment and maintains a low EVM over large misalignment distances. The system requires a very low EIRP, and the maximum data rate is mostly determined by the instantaneous bandwidth of the phased-array link.

In chapter 6, a method of determining the OIP3 of amplifiers used in phased-arrays using far-field measurements was presented. An equation translating the OIP3 measured in the far-field to a single amplifier output in the array is derived and proved to be valid by experiment. The technique can also detect resonances in the chip bias network.

In chapter 7, a 39 GHz 8x8 phased-array for 5G applications was presented. The array achieves an EIRP of 49-51 dBm with 3-dB bandwidth of 36-41.5 GHz. The array can scan up to $\pm 60^\circ$ in the azimuth plane and $\pm 50^\circ$ in the elevation plane. A complete 39 GHz system is demonstrated using an 8x8 array with a high-pass filter and a compact transceiver. The system has excellent LO and image rejection and $< 5\%$ EVM is achieved using a 64-QAM 200 MHz waveform with an average EIRP up to 44 dBm with calibration. Performance comparison with and without calibration is presented and negligible difference is observed in patterns and shows that phased-arrays based on 2x2 beamformer chips and a symmetrical layout can operate well. The EIRP and EVM of calibrated arrays are better than non-calibrated arrays and improvement of 1.4-1.7 dB is observed. The 39 GHz array achieves up to 30 Gbps data-rate with 64-QAM

waveforms and is an excellent candidate for 5G 39 GHz mm-wave systems.

8.2 Future Work

The phased-array systems presented in this dissertation may be expanded and improved in a few aspects:

1) For the wideband 28 GHz phased-array, future work is needed to optimize the carrier aggregation systems including the design of wideband power amplifiers with low IM3 products, the possible use of filters between the beamformer chip and antennas, and the design of radomes with bandpass properties.

2) It is advantageous to design a dual-band phased array which can be operated at 28- and 39-GHz bands and one RF system is needed for two licensed bands. This will greatly lower the cost of deployment. The design and optimization of dual-band antennas and beamformer chips is the main challenge for this system.

3) Electromagnetic band-gap (EBG) structures generate a stopband to block the propagation of electromagnetic waves at a certain frequency. Therefore, EBG structures can be used in phased arrays to suppress the triggering of surface-wave modes and improve the array scanning performance.

4) Wideband digital pre-distortion can be used at the array level to improve the system performance (EVM) vs. backoff. This can be done using low-power side-coupling antennas as feedback paths to the digital pre-distorter. The challenge is to find the correct algorithm which can be used over a large array, and to reduce the number of feedback paths.

Bibliography

- [1] W. Roh, J. Seol, J. Park, B. Lee, J. Lee, Y. Kim, J. Cho, K. Cheun, and F. Aryanfar, “Millimeter-wave beamforming as an enabling technology for 5G cellular communications: theoretical feasibility and prototype results,” *IEEE Communications Magazine*, vol. 52, no. 2, pp. 106–113, Feb 2014.
- [2] S. Onoe, “Evolution of 5G mobile technology toward 2020 and beyond,” in *2016 IEEE International Solid-State Circuits Conference (ISSCC)*, Feb 2016, pp. 23–28.
- [3] J. Pang, Z. Li, R. Kubozoe, X. Luo, R. Wu, Y. Wang, D. You, A. A. Fadila, R. Saengchan, T. Nakamura, J. Alvin, D. Matsumoto, A. T. Narayanan, B. Liu, J. Qiu, H. Liu, Z. Sun, H. Huang, K. K. Tokgoz, K. Motoi, N. Oshima, S. Hori, K. Kunihiro, T. Kaneko, A. Shirane, and K. Okada, “A 28GHz CMOS phased-array beamformer utilizing neutralized bi-directional technique supporting dual-polarized MIMO for 5G NR,” in *2019 IEEE International Solid-State Circuits Conference - (ISSCC)*, 2019, pp. 344–346.
- [4] B. Sadhu, Y. Tousi, J. Hallin, S. Sahl, S. K. Reynolds, . Renström, K. Sjögren, O. Haapalahti, N. Mazor, B. Bokinge, G. Weibull, H. Bengtsson, A. Carlinger, E. Westesson, J. Thillberg, L. Rexberg, M. Yeck, X. Gu, M. Ferriss, D. Liu, D. Friedman, and A. Valdes-Garcia, “A 28-GHz 32-element TRX phased-array IC with concurrent dual-polarized operation and orthogonal phase and gain control for 5G communications,” *IEEE Journal of Solid-State Circuits*, vol. 52, no. 12, pp. 3373–3391, Dec 2017.
- [5] J. D. Dunworth, A. Homayoun, B. Ku, Y. Ou, K. Chakraborty, G. Liu, T. Segoria, J. Lerdworatawee, J. W. Park, H. Park, H. Hedayati, D. Lu, P. Monat, K. Douglas, and V. Aparin, “A 28GHz Bulk-CMOS dual-polarization phased-array transceiver with 24 channels for 5G user and basestation equipment,” in *2018 IEEE International Solid - State Circuits Conference - (ISSCC)*, Feb 2018, pp. 70–72.
- [6] K. Kibaroglu, M. Sayginer, T. Phelps, and G. M. Rebeiz, “A 64-element 28-GHz phased-array transceiver with 52-dBm EIRP and 8–12-Gb/s 5G link at 300 meters without any calibration,” *IEEE Transactions on Microwave Theory and Techniques*, vol. 66, no. 12, pp. 5796–5811, Dec 2018.
- [7] J. Pang, R. Wu, Y. Wang, M. Dome, H. Kato, H. Huang, A. T. Narayanan, H. Liu, B. Liu, T. Nakamura, T. Fujimura, M. Kawabuchi, R. Kubozoe, T. Miura, D. Matsumoto, Z. Li,

- N. Oshima, K. Motoi, S. Hori, K. Kunihiro, T. Kaneko, A. Shirane, and K. Okada, "A 28-GHz CMOS phased-array transceiver based on LO phase-shifting architecture with gain invariant phase tuning for 5G new radio," *IEEE Journal of Solid-State Circuits*, vol. 54, no. 5, pp. 1228–1242, May 2019.
- [8] A. Nafe, M. Sayginer, K. Kibaroglu, and G. M. Rebeiz, "2x 64-element dual-polarized dual-beam single-aperture 28-GHz phased array with 2x 30 Gb/s links for 5G polarization MIMO," *IEEE Transactions on Microwave Theory and Techniques*, pp. 1–1, 2020.
- [9] H. Kim, B. Park, S. Oh, S. Song, J. Kim, S. Kim, T. Moon, S. Kim, J. Chang, S. Kim, W. Kang, S. Jung, G. Tak, J. Du, Y. Suh, and Y. Ho, "A 28GHz CMOS direct conversion transceiver with packaged antenna arrays for 5G cellular system," in *2017 IEEE Radio Frequency Integrated Circuits Symposium (RFIC)*, Jun 2017, pp. 69–72.
- [10] K. Kibaroglu, M. Sayginer, and G. M. Rebeiz, "A low-cost scalable 32-element 28-GHz phased array transceiver for 5G communication links based on a 2×2 beamformer flip-chip unit cell," *IEEE Journal of Solid-State Circuits*, vol. 53, no. 5, pp. 1260–1274, May 2018.
- [11] B. Ustundag, K. Kibaroglu, M. Sayginer, and G. M. Rebeiz, "A wideband high-power multi-standard 23–31 GHz 2×2 quad beamformer chip in SiGe with >15 dBm OP1dB per channel," in *2018 IEEE Radio Frequency Integrated Circuits Symposium (RFIC)*, Jun 2018, pp. 60–63.
- [12] Y. Yin, S. Zehir, T. Kanar, and G. M. Rebeiz, "A 37–42 GHz 8x8 phased-array for 5G communication systems with 48–50 dBm EIRP," in *2019 IEEE MTT-S International Microwave Symposium (IMS)*, Jun 2019, pp. 480–483.
- [13] Y. Wang, R. Wu, J. Pang, D. You, A. A. Fadila, R. Saengchan, X. Fu, D. Matsumoto, T. Nakamura, R. Kubozoe, M. Kawabuchi, B. Liu, H. Zhang, J. Qiu, H. Liu, N. Oshima, K. Motoi, S. Hori, K. Kunihiro, T. Kaneko, A. Shirane, and K. Okada, "A 39-GHz 64-element phased-array transceiver with built-in phase and amplitude calibrations for large-array 5G NR in 65-nm CMOS," *IEEE Journal of Solid-State Circuits*, vol. 55, no. 5, pp. 1249–1269, May 2020.
- [14] B. Rupakula, A. Nafe, S. Zehir, Y. Wang, T. Lin, and G. Rebeiz, "63.5–65.5-GHz Transmit/Receive Phased-Array Communication Link With 0.5–2 Gb/s at 100–800 m and $\pm 50^\circ$ Scan Angles," *IEEE Transactions on Microwave Theory and Techniques*, vol. 66, no. 9, pp. 4108–4120, Sep 2018.
- [15] M. Boers, B. Afshar, I. Vassiliou, S. Sarkar, S. T. Nicolson, E. Adabi, B. G. Perumana, T. Chalvatzis, S. Kavvadias, P. Sen, W. L. Chan, A. H. Yu, A. Parsa, M. Nariman, S. Yoon, A. G. Besoli, C. A. Kyriazidou, G. Zochios, J. A. Castaneda, T. Sowlati, M. Rofougaran, and A. Rofougaran, "A 16TX/16RX 60 GHz 802.11ad chipset with single coaxial interface and polarization diversity," *IEEE Journal of Solid-State Circuits*, vol. 49, no. 12, pp. 3031–3045, Dec 2014.

- [16] B. Rupakula, S. Zahir, and G. M. Rebeiz, "Low complexity 54–63-GHz transmit/receive 64- and 128-element 2-D-scanning phased-arrays on multilayer organic substrates with 64-QAM 30-Gbps data rates," *IEEE Transactions on Microwave Theory and Techniques*, vol. 67, no. 12, pp. 5268–5281, Dec 2019.
- [17] E. Cohen, M. Ruberto, M. Cohen, O. Degani, S. Ravid, and D. Ritter, "A CMOS bidirectional 32-element phased-array transceiver at 60 GHz with LTCC antenna," *IEEE Transactions on Microwave Theory and Techniques*, vol. 61, no. 3, pp. 1359–1375, Mar 2013.
- [18] T. Cappello, A. Duh, T. W. Barton, and Z. Popovic, "A dual-band dual-output power amplifier for carrier aggregation," *IEEE Transactions on Microwave Theory and Techniques*, vol. 67, no. 7, pp. 3134–3146, Jul 2019.
- [19] S. Mondal and J. Paramesh, "A reconfigurable 28-/37-GHz MMSE-adaptive hybrid-beamforming receiver for carrier aggregation and multi-standard MIMO communication," *IEEE Journal of Solid-State Circuits*, vol. 54, no. 5, pp. 1391–1406, May 2019.
- [20] S. Mondal, R. Singh, and J. Paramesh, "A reconfigurable bidirectional 28/37/39GHz front-end supporting MIMO-TDD, carrier aggregation TDD and FDD/full-duplex with self-interference cancellation in digital and fully connected hybrid beamformers," in *2019 IEEE International Solid-State Circuits Conference - (ISSCC)*, Feb 2019, pp. 348–350.
- [21] S. Shakib, M. Elkholy, J. Dunworth, V. Aparin, and K. Entesari, "2.7 A wideband 28GHz power amplifier supporting 8×100MHz carrier aggregation for 5G in 40nm CMOS," in *2017 IEEE International Solid-State Circuits Conference (ISSCC)*, Feb 2017, pp. 44–45.
- [22] S. S. et al, "A wideband 28-GHz transmit–receive front-end for 5G handset phased arrays in 40-nm CMOS," *IEEE Transactions on Microwave Theory and Techniques*, vol. 67, no. 7, pp. 2946–2963, Jul 2019.
- [23] R. B. Waterhouse, "Design of probe-fed stacked patches," *IEEE Transactions on Antennas and Propagation*, vol. 47, no. 12, pp. 1780–1784, Dec 1999.
- [24] J. T. Aberle, D. M. Pozar, and J. Manges, "Phased arrays of probe-fed stacked microstrip patches," *IEEE Transactions on Antennas and Propagation*, vol. 42, no. 7, pp. 920–927, Jul 1994.
- [25] B. Rupakula and G. M. Rebeiz, "Third-order intermodulation effects and system sensitivity degradation in receive-mode 5G phased arrays in the presence of multiple interferers," *IEEE Transactions on Microwave Theory and Techniques*, vol. 66, no. 12, pp. 5780–5795, Dec 2018.
- [26] A. G. Roy, O. Inac, A. Singh, T. Mukatel, O. Brandelstein, T. W. Brown, S. Abughazaleh, J. S. Hayden, B. Park, G. Bachmanek, T. J. Kao, J. Hagn, S. Dalmia, D. Shoham, B. Davis, I. Fisher, R. Sover, A. Freiman, B. Xiao, B. Singh, and J. Jensen, "A 37-40 GHz phased array front-end with dual polarization for 5G MIMO beamforming applications," in *2019 IEEE Radio Frequency Integrated Circuits Symposium (RFIC)*, Jun 2019, pp. 251–254.

- [27] Y. Yoon, K. H. An, D. Kang, K. Kim, S. Lee, J. S. Jang, D. Minn, B. Suh, J. Lee, J. Kim, M. Kim, J. H. Lee, S. T. Choi, J. Son, and S. Yang, "A highly linear 28GHz 16-element phased-array receiver with wide gain control for 5G NR application," in *2019 IEEE Radio Frequency Integrated Circuits Symposium (RFIC)*, Jun 2019, pp. 287–290.
- [28] *Millimeter Wave Propagation: Spectrum Management Implications*. Federal Communications Commission Office of Engineering and Technology, Jul 1997.
- [29] Y. Cho, W. Lee, H. Park, B. Park, J. H. Lee, J. Kim, J. Lee, S. Kim, J. Park, S. Park, K. H. An, J. Son, and S. Yang, "A 16-element phased-array CMOS transmitter with variable gain controlled linear power amplifier for 5G new radio," in *2019 IEEE Radio Frequency Integrated Circuits Symposium (RFIC)*, Jun 2019, pp. 247–250.
- [30] B. Rupakula, A. H. Aljuhani, and G. M. Rebeiz, "ACPR improvement in large phased arrays with complex modulated waveforms," *IEEE Transactions on Microwave Theory and Techniques*, vol. 68, no. 3, pp. 1045–1053, Mar 2020.
- [31] D. M. Pozar, *Microwave Engineering 4th ed.* NJ: Wiley, 2012.
- [32] G. M. Rebeiz, S. Kim, O. Inac, W. Shin, O. Gurbuz, Y. Ou, F. Golcuk, T. Kanar, and B. Ku, "Millimeter-wave large-scale phased-arrays for 5G systems," in *2015 IEEE MTT-S International Microwave Symposium*, May 2015, pp. 1–3.
- [33] H. Kim, B. Park, S. Song, T. Moon, S. Kim, J. Kim, J. Chang, and Y. Ho, "A 28-GHz CMOS direct conversion transceiver with packaged 2×4 antenna array for 5G cellular system," *IEEE Journal of Solid-State Circuits*, vol. 53, no. 5, pp. 1245–1259, May 2018.
- [34] F. Aryanfar, J. Pi, H. Zhou, T. Henige, G. Xu, S. Abu-Surra, D. Psychoudakis, and F. Khan, "Millimeter-wave base station for mobile broadband communication," in *2015 IEEE MTT-S International Microwave Symposium*, May 2015, pp. 1–3.
- [35] A. Nafe, M. Sayginer, K. Kibaroglu, and G. M. Rebeiz, "2x64 Dual-Polarized Dual-Beam Single-Aperture 28 GHz Phased Array with High Cross-Polarization Rejection for 5G Polarization MIMO," in *2019 IEEE MTT-S International Microwave Symposium (IMS)*, Jun 2019, pp. 484–487.
- [36] K. Kibaroglu, M. Sayginer, A. Nafe, and G. M. Rebeiz, "A dual-polarized dual-beam 28 GHz beamformer chip demonstrating a 24 Gbps 64-QAM 2x2 MIMO link," in *2018 IEEE Radio Frequency Integrated Circuits Symposium (RFIC)*, Jun 2018, pp. 64–67.
- [37] Y. Wang, R. Wu, J. Pang, D. You, A. A. Fadila, R. Saengchan, X. Fu, D. Matsumoto, T. Nakamura, R. Kubozoe, M. Kawabuchi, B. Liu, H. Zhang, J. Qiu, H. Liu, W. Deng, N. Oshima, K. Motoi, S. Hori, K. Kunihiro, T. Kaneko, A. Shirane, and K. Okada, "A 39GHz 64-element phased-array CMOS transceiver with built-in calibration for large-array 5G NR," in *2019 IEEE Radio Frequency Integrated Circuits Symposium (RFIC)*, Jun 2019, pp. 279–282.

- [38] B. Rupakula, S. Zahir, and G. M. Rebeiz, "A 128-element 54-63 GHz 2-dimensional Tx/Rx phased-array with 64-QAM/30 Gbps communication links," in *2019 IEEE MTT-S International Microwave Symposium (IMS)*, Jun 2019, pp. 1072–1075.
- [39] S. Zahir, O. D. Gurbuz, A. Kar-Roy, S. Raman, and G. M. Rebeiz, "60-GHz 64- and 256-elements wafer-scale phased-array transmitters using full-reticle and subreticle stitching techniques," *IEEE Transactions on Microwave Theory and Techniques*, vol. 64, no. 12, pp. 4701–4719, Dec 2016.
- [40] A. Valdes-Garcia, S. T. Nicolson, J. Lai, A. Natarajan, P. Chen, S. K. Reynolds, J. C. Zhan, D. G. Kam, D. Liu, and B. Floyd, "A fully integrated 16-element phased-array transmitter in SiGe BiCMOS for 60-GHz communications," *IEEE Journal of Solid-State Circuits*, vol. 45, no. 12, pp. 2757–2773, Dec 2010.
- [41] C. Kim, D. Kang, and G. M. Rebeiz, "A 44–46-GHz 16-element SiGe BiCMOS high-linearity transmit/receive phased array," *IEEE Transactions on Microwave Theory and Techniques*, vol. 60, no. 3, pp. 730–742, Mar 2012.
- [42] J. Hacker, C. Hillman, A. Papavasiliou, C. G. Kim, A. Abbaspour-Tamijani, C. Y. Kim, D. W. Kang, and G. Rebeiz, "A 16-element transmit/receive Q-band electronically steerable subarray tile," in *2012 IEEE/MTT-S International Microwave Symposium Digest*, Jun 2012, pp. 1–3.
- [43] K. Kibaroglu, M. Sayginer, and G. M. Rebeiz, "A 28 GHz transceiver chip for 5G beamforming data links in SiGe BiCMOS," in *2017 IEEE Bipolar/BiCMOS Circuits and Technology Meeting (BCTM)*, Oct 2017, pp. 74–77.
- [44] Q. Chu, X. Wu, and X. Tian, "Novel UWB bandpass filter using stub-loaded multiple-mode resonator," *IEEE Microwave and Wireless Components Letters*, vol. 21, no. 8, pp. 403–405, Aug 2011.